



**FAKULTA STROJNÍ
ZÁPADOČESKÉ
UNIVERZITY
V PLZNI**

**Z Á P A D O Č E S K Á U N I V E R Z I T A V
P L Z N I F A K U L T A S T R O J N Í K A T E D R A
M A T E R I Á L U A S T R O J Í R E N S K É
M E T A L U R G I E**

TEZE DISERTAČNÍ PRÁCE

Doktorský studijní program: P2301 Strojní inženýrství Studijní obor: Materiálové inženýrství a strojírenská metalurgie

First principle studies of optical, thermoelectric and electronic characteristics of complex materials

Studium optických, termoelektrických a elektronických charakteristik složitých materiálů z prvních principů

Autor: Sikander Azam

Školitel: Priv. Doz. Dr. J. Minár

Prohlášení o autorství

Předkládám tímto k posouzení a obhajobě disertační práci, zpracovanou na závěr studia doktorského studijního programu na Fakultě strojní Západočeské univerzity v Plzni. Prohlašuji, že jsem tuto disertační práci vypracovala samostatně, s použitím odborné literatury a pramenů, uvedených v seznamu, který je součástí této disertační práce.

V Plzni dne:

.....

Podpis autora

Prohlašuji, že jsem předloženou disertační práci vypracoval samostatně s použitím uvedené literatury a zdrojů informací. Prohlašuji, že obsah tištěné verze disertační práce a obsah elektronické verze disertační práce ve formátu PDF umístěné na CD-ROM v příloze tištěné disertační práce jsou shodné.

V Plzni dne:

Abstract

Advancement in optical telecommunications and optical computing devices has increased the demand for materials with greater optical coefficients. For that reason, several materials with suitable optical properties have been designed, some of which are based on the family of quaternary chalcogenide compounds. Their flexibility in varying composition as well as structure allows tuning their optical properties.

Quaternary chalcogenide compounds have gained popularity due to suitability for a wide range of technological applications, such as photovoltaic, optoelectronic, thermoelectric, medical, etc. Recently, these materials have been utilized more extensively owing to their improved thermoelectric and optoelectronic properties. Most of the extant work has been performed in synthesizing the compounds and studying their thermoelectric properties.

Theoretical studies are considered fundamental in the evolution of novel materials and devices for various industrial applications. Applying the first principles method, it is now possible to access a database of crystal structures and use computer software to predict and understand material properties when experimental measurements are absent. The same approach was adopted in this work to study the structural, electronic, optical and thermoelectric properties of materials based on sulfur (S), selenium (Se), and tellurium (Te), i.e., the quaternary chalcogenide compounds. Theoretical calculations allow gaining better insight into molecular properties of these materials. The main aim of the present work is better understanding of the electronic structure, as well as optical and thermoelectric properties, of the aforementioned class of quaternary chalcogenide compounds.

In this thesis, the electronic structure and optical properties calculations are extensively studied by applying Density functional theory (DFT), which can successfully reveal different properties of many condensed matter systems. In addition, the full potential linear augmented plane wave (FP-LAPW) method, as incorporated in the WIEN2K code, is applied, to study the electronic structure, thermal properties and linear optical properties of some quaternary chalcogenide compounds.

Using the investigated structure, the thermoelectric properties (electrical and thermal conductivity, Seebeck coefficient, Figure of merit and power factor) are described, along with the development of Boltzmann transport equation with constant relaxation time approximation.

Abstract

Pokrok v optické telekomunikaci a v optických výpočetných zařízeních zvýšil poptávku po materiálech s vyššími optickými koeficienty. Za tímto účelem bylo navrženo několik materiálů s vhodnými optickými vlastnostmi. Na základě nedávných studií byla pro vývoj těchto materiálů navržena skupina kvaternárních chalkogenidů. Široká variabilita ve složení i ve struktuře umožňuje ladit optické vlastnosti těchto chalkogenních sloučenin.

Skupina kvaternárních chalkogenidů byla sledována pro jejich rozsáhlé možnosti v technologických aplikacích, jako například ve fotovoltaice, optoelektronických aplikacích, termoelektrických aplikacích, v lékařství atd. Velké pozornosti se těmto materiálům dostalo během několika posledních let, zejména kvůli jejich vylepšeným termoelektrickým a optoelektronickým vlastnostem. Většina výzkumu se týkala syntetizování sloučenin a studia jejich termoelektrických vlastností.

Teoretické studie jsou pro vývoj nových materiálů a zařízení pro různé průmyslové aplikace považovány za zásadní. Metody vycházející z prvních principů umožňují vyjít z databáze krystalových struktur a pomocí počítačových programů předpovědět vlastnosti a porozumět jim i v případě, že experimentální data nejsou k dispozici. Z toho důvodu jsme se zaměřili na studium kvaternárních chalkogenidů obsahujících síru (S), selen (Se), telur (Te) pomocí metod vycházejících z prvních principů. Teoretické výpočty mohou být nejlepším způsobem jak získat vhled do molekulárních vlastností. Hlavním cílem předkládané práce je studium elektronové struktury a optických a termoelektrických vlastností třídy kvaternárních chalkogenních sloučenin.

V této práci jsou prezentovány rozsáhlé výpočty elektronové struktury a optických vlastností uskutečněné v rámci teorie funkcionálu hustoty (DFT), která byla již mnohokrát úspěšně použita pro pevné látky. Pro výpočty elektronových struktur, teplotních vlastností a lineárních optických vlastností různých kvaternárních chalkogenních sloučenin jsme využili linearizovanou metodu přidružených vln pro úplný potenciál (full-potential linear augmented plane wave, FP-LAPW) implementovanou programem WIEN2k.

Získané výsledky ohledně struktury a elektronové struktury pak byly použity pro studium termoelektrických vlastností (elektrické a teplotní vodivosti, Seebeckova koeficientu, koeficientu termoelektrické činnosti, výkonnostního faktoru) pomocí Boltzmanovy transportní rovnice v aproximaci konstantní relaxační doby.

Acknowledgments

Thanking people after a goal has been achieved is a hard task because a relevant order cannot be assigned. Any little action can influence the final result of a research project. One word, one smile, even a short fresh breeze in the right moment and place can unchain a terrible or favorable workday in a fundamental stage. I would like to honor here by including as much as possible the names of this people whose help, support, encouragement and best wishes allowed me to arrive safe at the end of this remarkable journey. Thanks to them this PhD was a memorable and unforgettable experience. After having pointed out the above, here I go (without any particular order of relevance):

All praises be to Almighty Allah who created the human being with intelligence, knowledge, sight to observe and mind to think. The fact that a single name appears on the title page of this thesis can be quite misleading. This journey would not have been thinkable without the support of great number of people.

I wish to express my devoted thanks to my parents and late Grand Mother for raising me up and supporting me, my uncle, aunt, brothers and sisters for being there since my childhood, whose prayers and affection eventually enabled me to complete this task and materialize my dreams.

I am grateful to my supervisor Prof. Dr. Jan Minár for his encouragement and supervision throughout my Ph.D. study. His valuable scientific advices, suggestions, and discussions make my graduation project successful. I have learned a lot from him including scientific knowledge, good article writing skills, and very especially for reading and correcting my research achievements. I am extremely thankful to him for giving total freedom in selecting research problems and providing me thoughtful suggestions. The strong scientific foundation that he has given me will continue to guide and inspire me in my future carrier

I offer my cordial and profound thanks to my elder brother Anwar Shah, his helping hands were always there for me whenever I need him. His physical and moral support has always kept my courage high. It would take forever to list all the help I got from him.

I extend my deepest gratitude to Prof. Ondřej Šipr, I got a lot of help from him.

I would also like to thank my fellow Ph.D. students, Saleem Ayaz Khan and Wilayat Khan, for their help and words of advice throughout this project.

I would also like to give full credit to all my school, college and university teachers who shaped me into who I am.

I am grateful to Prof. Professor Xavier GONZE for offering the opportunity to visit his group at the Institute of Condensed Matter and Nanosciences - Nanoscopic physics research division Chemin des toiles, 8 bte L7.03.01, B-1348 Louvain-la-neuve,

Belgium. It was a great experience working with him and his helpful discussions on scientific problems greatly influenced my way of research direction. Thanks to all of his group, staff and the institute of Condensed Matter and Nanosciences.

I would like to mention my appreciation to all of my previous teachers, who educated me with great effort and patience to prepare me for the future. My colleagues are definitely not limited to the group who helped in one or other way to accomplish this task. I truly thank, Anees Ahmad, Muhammad Javed, Fahad Ali Shah, Haleem Ud Din, Roshan Khan, Bin e Amin, Ghulam Murtaza, Imad Khan, Zahid Khan, Arshad Hayat, Fayaz Muhammad, Prof. Dr. Saleh Muhammad, Ijaz Ali, Muhammad Tariq, Abduraziq and many others for being genuinely nice, supportive and always stood beside me unconditionally when I was irritable and depressed in difficult time.

There have been times where things have failed and I am grateful for the technical assistance I have received from the Martin Shafranik.

I gratefully acknowledge the funding source of NTC (Czech Republic) that made my Ph.D. work possible. Finally the last but not the least, thank you so much Pakistan and Czech Republic for providing everything that I needed.

Contents

1	Introduction	1
1.1	The Chalcogenides	1
1.2	Materials Selected for the Current Study	2
1.2.1	Layered-Pb based Quaternary Chalcogenides (Tl_2PbXY_4 ($X=\text{Zr}$, Hf and $Y=\text{S}$, Se))	3
1.2.2	Quaternary Copper Palladium Polyselenides ($\text{Rb}_2\text{Pd}_3\text{UM}_6$ ($M=\text{S}$, Se))	4
1.2.3	Quaternary Uranium Chalcogenides ($\text{Rb}_2\text{Pd}_3\text{UM}_6$ ($M=\text{S}$, Se))	4
1.2.4	Quaternary Selenides (KBaMSe_3 ($M=\text{As}$, Sb))	5
1.2.5	New Quaternary Chalcogenide Selenides ($\text{Ba}_4\text{Ga}_4\text{SnSe}_{12}$)	6
1.2.6	The Present Study	7
1.3	Applications	7
1.4	Objective	8
2	Theoretical Background	10
2.1	Background	10
2.2	The Many-Body Problem	11
2.3	Level 1: The Born-Oppenheimer Approximation	11
2.3.1	Level 2: Density Functional Theory	13
2.3.2	Hohenberg-Kohn (H-K) Theorem	13
2.3.3	The Kohn-Sham (K-S) Equations	14
2.3.4	Exchange Correlation Functional $E_{XC}[n]$	16
2.3.5	The Local Density Approximation (LDA)	16
2.3.6	The gradient Generalized Approximation	16
2.3.7	modified Becke-Johnson potential (mBJ)	16
2.3.8	Self-Consistent Kohn-Sham (K-S Scheme)	17
3	Band structure method	19
3.1	Bloch's Theorem	21
3.2	Augmented Plane Wave Scheme	21
3.3	The Concept of LAPW Method	24

3.4	The full-potential linear augmented plane wave method (FP-LAPW)	25
3.5	Technical Parameters: Energy Cutoff and K-mesh	25
3.6	Structure of the WIEN2k code	27
3.7	Theory of Optical Properties (OP)	29
3.8	Dielectric Function	29
3.8.1	Intra-band Transitions	29
3.8.2	Direct inter-band transitions	32
3.9	Boltzmann Transport Theory	35
3.9.1	Thermoelectric (TE) Properties	36
4	Conclusion	39
5	Bibliography	40
6	Reprints of selected publications	45
7	Curriculum vitae	87
8	List of publications	91

List of Figures

2.1	Self-consistent K-S scheme.[42]	18
3.1	Schematic overview of the electronic structure methods that shows a spectrum of methods. Which are developed for many purposes, geometries, applications and symmetries requiring different approximations. [45]	20
3.2	Schematic division of (a) Space into Muffin-tin spheres and an interstitial region. b) Wave function in to black atomic partial waves in the MT sphere and red plane waves in I region [42]	22
3.3	Satisfying the secular equation $ H - ES = 0$ in APW by numerically finding the zeros [48]	23
3.4	Flowchart of APW method.[42]	23
3.5	Augmentation of a PW by a p-like partial wave inside the iron atomic sphere by APW (kink) and by LAPW (smooth derivative)[48]	24
3.6	Wien2k flow chart[55]	28
3.7	Intra-band transition.[56]	30
3.8	Inter-band transition[56]	33
3.9	Dependence of Seebeck coefficient, electrical conductivity, thermal conductivity and power factor on charge carrier concentration [58].	37

Chapter 1

Introduction

1.1 The Chalcogenides

From the very beginning of evolution, humans worked on the physical properties of materials in order to ensure that they meet their needs and this remains a key field of interest for scientists today. Thus far, scientists have succeeded in obtaining efficient materials for different technological applications and are still working on further improvement in this field.

Pn-junction and transistor brought a revolution in the field of condensed matter physics. The most valuable work in science, especially in the field of condensed matter, pertains to the semiconductor chips (integrated circuits). Today, many electronic devices are of very small size, due to the use of semiconductors in the electronic circuits, which also make these devices more efficient and reliable.

Technological and industrial development relies on the advances made in the field of semiconductors, magnetic and metallic materials, which are the basic building blocks of electronic devices. Promising devices are based on the chalcogenide compounds, owing to their advantageous properties.

Chalcogenide materials, i.e., those containing the chalcogen elements (S, Se, or Te), are widely investigated for their applications in technological uses, for instance, thermoelectric, non-linear optical materials, photoelectric, phosphors, and solid-state electrolytes for lithium secondary batteries, among others. Chalcogenide compounds have a very diverse and interesting structural chemistry and possess useful physical and chemical properties that may be applicable to modern technologies [1]. They have received much attention during the past decade, largely because of their optoelectronic and thermoelectric properties.

These materials have wide variations in their energy gaps (E_g), ranging from ultraviolet (UV) to infrared (IR). Such properties are useful in the development of light emitting diodes (LED), laser diodes, optoelectronic devices and optical detectors.

Most such compounds, especially metal sulfides, selenides and tellurides, belong to a large class of compounds known as metal chalcogenides. Sulfur, being able to catenate and bind to several metal centers, has great importance in chemistry of metal chalcogenides, and similar nature has been determined for Se and Te [1, 2]. Metalsulfur compounds have been widely studied in chemistry due to their important properties.

Significance of these compounds has been enhanced owing to their unique and diverse properties and their vital role in hydro-desulfurization, bioinorganic chemistry and other catalytic methods. Complexes of molecular transition metal with terminal/bridging sulfide ligands have been extensively studied for their catalytic activities [3, 4]. Using the solid-state approach or in solution, soluble metal fluorides and sulfides have been synthesized and their properties demonstrated [5, 6]. Some compounds, including selenium and tellurium, have structure types that are presently unknown in sulfur chemistry. Tellurium, due to its large size, diffused orbitals and greater metallic nature relative to other chalcogen elements, is characterized by very different non-classical chemistry.

Most of low-dimensional materials have been greatly modified by covalent bond nature of metal chalcogenides. The valence electrons of 4d- and 5d-elements make them highly suitable for forming M-M (metal-metal) bonds, which are restricted to directly coupled atoms, and clusters in particular. Such types of clusters are found in discrete molecular units joined by bridging ligands [7]. Chalcogenide clusters are presently the best known inorganic or high valence clusters and are typical for 4d- and 5d-metals of groups V-VII [8].

1.2 Materials Selected for the Current Study

Modification of binary chalcogenides results in more complex ternary and quaternary chalcogenides and leads to an increase in diversity of function and structure. Research on binary and ternary chalcogenides in the field of physics and chemistry has gained momentum during the past decade, and these studies have paved the way for a more comprehensive understanding of these compounds, causing significant advances in quaternary material preparation techniques. Chalcogenides are particularly interesting due to their rich structural chemistry [9].

More recently, experimental and technological research of quaternary metal chalcogenides has been particularly intensive [10, 11], resulting in a much greater structural diversity and wide functionality of these materials.

Yet, despite extensive body of research in this field, there is evident paucity of theoretical work related to the electronic structure, optical and thermal properties of quaternary chalcogenides. This thesis aims to address this gap in the literature.

Indeed, physics of these systems doped with different types of impurities requires further investigation.

The present study focuses on five different quaternary chalcogenide materials. In particular, the possibility of band-gap engineering is explored, as it can lead to remarkable thermoelectric and optical properties that are important for thermoelectric and optoelectronic device applications. The design of novel functional semiconductors with various values of the energy band gap is an area of intense research also explored in this work.

1.2.1 Layered-Pb based Quaternary Chalcogenides (Tl_2PbXY_4 ($\text{X}=\text{Zr, Hf}$ and $\text{Y}=\text{S, Se}$))

Transition metal chalcogenides are considered interesting candidates for thermoelectric materials because of low thermal conductivity. Examples of recently developed thermoelectric materials based on selenides include Bi_2Se_3 [6], doped PbSe [12], quaternary tin selenide $\text{K}_{1-x}\text{Sn}_{5x}\text{Bi}_{11+x}\text{Se}_{22}$ [13] and CsCdInQ_3 ($\text{Q}=\text{Se, Te}$) [14].

The Tl-based quaternary chalcogenides incorporating a group IV-B metal ($\text{X}=\text{Zr, Hf}$) are particularly attractive for use in thermoelectric devices. Thallium (Tl), being a heavy metal, reduces the thermal conductivity and creates complex coordination due to the presence of a lone pair electron and is very useful in thermoelectrics. This lone pair of electrons has a significant effect on thermal conductivity and creates the anharmonicity in the lattice.

Among complex inorganic compounds, a new class of quaternary compounds with the general formula $\text{Tl}_2\text{Pb}_X\text{Y}_4$ ($\text{X}=\text{Zr, Hf}$ and $\text{Y}=\text{S, Se}$) has been investigated. These compounds crystallize in the monoclinic crystal system with space group C2/c and have indirect band gaps below 1 eV, while their optical gaps range from 1.2 to 1.6 eV. The electrical transport properties of $\text{Tl}_2\text{Pb}_X\text{Y}_4$ indicate that this material is of a semiconducting nature [15]. A large positive Seebeck coefficient ranging from $S = +190 \sim \text{V/K}$ at room temperature to $S = +420 \sim \text{V/K}$ at 520 K has been observed for $\text{Tl}_2\text{PbHfSe}_4$ [15].

Extensive literature review conducted as a part of this study, however, failed to identify any studies related to the electronic, optical and thermoelectric properties of the Tl-based quaternary chalcogenides $\text{Tl}_2\text{Pb}_X\text{Y}_4$ ($\text{X}=\text{Zr, Hf}$ and $\text{Y}=\text{S, Se}$). Thus, this is the focus of the present study.

1.2.2 Quaternary Copper Palladium Polyselenides ($\text{Rb}_2\text{Pd}_3\text{UM}_6$ (M=S, Se))

Synthesis of novel quaternary chalcogenides has recently become an active area of research in solid state chemistry [16, 17, 18]. Most known quaternary chalcogenides are obtained using the molten alkali metal polychalcogenide flux technique, although low temperature solvo (hydro) thermal reactions have produced a limited number of quaternary chalcogenides [19]. Pd-obtaining compounds have received much consideration in extant studies because of the catalytic functions of the metal and its capacity to form polychalcogenide complexes in solution.

Several ternary Pd polychalcogenides have now been isolated and structurally characterized. These include $(\text{Ph}_4\text{P})_2[\text{Pd}(\text{Se}_4)_2]$ with distinct $[\text{Pd}(\text{Se}_4)_2]^{2-}$ anions in which each Pd^{2+} is coordinated by two chelating $(\text{Se}_4)^{2-}$ ligands [20] $(\text{CH}_3\text{N}(\text{CH}_2\text{CH}_2)_3\text{N}_2[\text{Pd}(\text{Se}_6)_2]$ and $(\text{enH})_2[\text{Pd}(\text{Se}_5)_2]$, featuring sheet-like, two-dimensional (2D) Pd polyselenide anionic frameworks [21] $\text{Rb}_2[\text{Pd}(\text{Se}_4)_2]\text{Se}_8$ encompassing sheet-like polyanion $[\text{Pd}(\text{Se}_4)_2]^{2-}$ with intercalated crown-like Se_8 eight-membered rings [22] and $\text{K}_4[\text{Pd}(\text{Se}_4)_2][\text{Pd}(\text{Se}_6)_2]$ ($=\text{K}_2\text{PdSe}_{10}$) and $\text{Cs}_2[\text{Pd}(\text{Se}_4)_2]$ ($=\text{Cs}_2\text{PdSe}_8$) having three dimensional (3D) structures assembled from two interpenetrating $[\text{Pd}(\text{Se}_x)_2]^{2-}$ structures ($x=4$ and 6 for the K^+ saline, $x=4$ and 4 for the Cs^+ salt) [23, 24].

In 2003, Chen et al. [25] reported the crystal structures, optical and thermal properties of two innovative mixtures, $\text{APdCu}(\text{Se}_2)(\text{Se}_3)$ ($A=\text{K}$ or Rb), which are the first quaternary copper palladium polychalcogenides obtained by solvothermal procedures utilizing ethylenediamine (en) as a reaction medium.

Still, to date, no theoretical studies relating to thermoelectric properties have been conducted. For this reason, the electrical transport parameters (conductivity, Seebeck coefficient, and power factor) for the compound system are the subject of this research.

1.2.3 Quaternary Uranium Chalcogenides ($\text{Rb}_2\text{Pd}_3\text{UM}_6$ (M=S, Se))

Recently, quaternary uranium chalcogenide compounds, such as $\text{Rb}_2\text{Pd}_3\text{UM}_6$ (M=S, Se), containing both a transition and an actinide metal, have been studied due to their important magnetic properties. Extant research in this field has, however, predominantly focused on the dependence of physical properties on U-U interatomic distances and uranium coordination environment [26]. The U-U interatomic distances determine whether long-range magnetic ordering occurs, whereas the crystalline electric field effect is produced by the coordination number [27].

Moreover, the interaction between f-orbital electrons of uranium (U) and the

valence orbitals of the palladium (Pd) complicates the magnetic behavior and results in orbital overlapping in close proximity of intermetallic compounds. An anion, such as sulfur (S) or selenium (Se), can be incorporated to position these magnetic atoms far apart and reduce the orbital overlaps. Additionally, the oxidation states are assigned to the atoms, which adopt characteristic coordination environments that are not present in intermetallic compounds. $\text{Rb}_2\text{Pd}_3\text{US}_6$ possesses unusually low magnetic moment to crystalline electric field effect as well as noticeable magnetic anisotropy. These quaternary compounds crystallize in orthorhombic structure with space group of Fmmm.

Literature review has revealed very few works relating the electronic structure of $\text{Rb}_2\text{Pd}_3\text{UM}_6$ ($\text{M} = \text{S}, \text{Se}$) compounds. Thus, the aim of this thesis is to perform some theoretical studies of the two crystals, including the band structure, density of states (total and partial), Fermi surface and optical properties.

1.2.4 Quaternary Selenides (KBaMSe_3 ($\text{M} = \text{As}, \text{Sb}$))

During the last few decades, the newly investigated multinary chalcogenides comprising of two or more metal cations have gained immense importance, as their structural and compositional complexity is suitable for applications based on various physical properties (e.g., thermoelectric, superconducting, magnetic, nonlinear optical properties), such as battery electrodes and photo-voltaic applications [28]. The stereochemical activity of ns^2 lone pair of electrons of M ($\text{M} = \text{As}, \text{Sb}$) strongly affects the structure, electronic nature and the properties of the resultant compound.

Over the past few years, the synthesis of new multinary chalcogenides containing elements of the 15th group has been performed and many chalcogenides with fascinating physical properties have been discovered [28, 29]. The isostructural quaternary KBaMSe_3 ($\text{M} = \text{As}, \text{Sb}$) selenides crystallize in the centrosymmetric space group P21/c of the monoclinic crystal system. The trivalent M atom coordinated to three Se atoms forms a trigonal pyramid with the Se atoms serving as the triangle base, which indicates the stereochemical activity of the ns^2 lone pair electron [30].

Microscopic packing of anions is greatly influenced by the size and charge of cations and generally determines various crystal properties [30, 28]. Therefore, the combination of different size and charge of the alkali and the alkaline-earth cations influences the packing of anions in various ways and exhibits a considerable effect on the stoichiometries, structures, and properties of KBaMSe_3 ($\text{M} = \text{As}, \text{Sb}$). An indirect band gap semiconductor nature with band gap values of 2.26 and 2.04 eV for KBaAsSe_3 and KBaSbSe_3 , respectively, has been investigated using the diffuse reflectance spectra [30].

The interesting properties discussed above make the electronic structure and

optical properties of KBaMSe_3 ($M = \text{As, Sb}$) an important study topic.

1.2.5 New Quaternary Chalcogenide Selenides ($\text{Ba}_4\text{Ga}_4\text{SnSe}_{12}$)

The noncentrosymmetric polar characteristics and simultaneous transmission of long wavelength radiation required of such crystals point to complex chalcogenides as a potential source of nonlinear optical (NLO) materials. As a source of new NLO materials, quaternary chalcogenides are attractive due to a variety of acentric arrangements resulting from the combination of two types of metal centers with different size, coordination preference, and packing characteristics [32].

Rare-earth chalcogenides exhibit not only rich structures resulting from the diverse geometry of the Ln-centered coordination polyhedra and the flexible connectivity among them, but also attractive magnetic, transport, and optical properties related to the 4f electrons [33]. Wenlong Yin et al. [34]. In their early studies, Wenlong Yin et al. developed the quaternary A/M/M'/Q ($A = \text{alkaline-earth metal}$; $M = \text{Al, Ga, In}$; $M' = \text{Si, Ge}$; $Q = \text{S, Se, Te}$) system and originated four iso-structural compounds, BaGa_2MQ_6 ($M = \text{Si, Ge}$; $Q = \text{S, Se}$), which were described as a new-fangled series of IR nonlinear optical materials showing promise for practical applications.

Recently, W. Yin et al. [34] have presented the syntheses, structural characterization, and band gaps measurement of new quaternary selenides. The authors also reported the electronic band structure calculated using the plane-wave pseudopotential method. The latter employed a method based on a pseudopotential that is not all-electron and thus might suffer from some shortcomings. In the present study, calculations are performed by considering all-electron potential approach, applying all full potential linear augmented plane wave method.

1.2.6 The Present Study

In this thesis, density functional calculation is used to study the electronic structure, bonding, optical and thermoelectric properties of quaternary chalcogenide compounds. Density Functional Theory (DFT) is widely used in computational solid state physics to calculate structural, magnetic, hyperfine and ground state properties of real materials from first principle.

The aim of this thesis is to bridge the gap between theoretical considerations and experimental investigations of the bonding. All material properties were calculated using the full potential linearized augmented plane wave (FP-LAPW) method within DFT. In the FP-LAPW scheme, the valence electrons are treated semi-relativistically, while the core electrons are treated fully relativistically. Most of the studies relating to these (optical and thermal) properties have been performed in the past few decades because these materials have numerous potential technological applications, such as photovoltaic, optoelectronic and electrochemical devices.

In this study, the focus is on quaternary chalcogenide semiconducting/metallic compounds. The electronic properties studied in this thesis are band structure (BS), density of states (DOS), Fermi surface, electronic charge density (ECD), effective mass, frequency dependent anisotropic complex dielectric function $\epsilon(\omega) = \epsilon_1(\omega) + i\epsilon_{12}(\omega)$ and thermal properties.

The goal of this thesis is gaining further insights into materials based on chalcogenides by means of computational methods. In Chapter 2, the theoretical methodology is briefly discussed, while the band structure methods are presented in Chapter 3. Chapter 4 provides conclusion to the study, and is followed by the results and discussions of different projects, which are the topic of Chapter 5. The discussions on these materials are already published in different journals. As the first author, the researcher was responsible for carrying out all the computations described in the papers and writing the manuscripts.

1.3 Applications

Rapid technological advancement we are presently witnessing would not be possible without materials that have the optimal combination of properties for the desired application. For example, without heat-resistant ceramics, space shuttles would burn up during atmospheric reentry, and without the unique properties of semiconductors, today's electronics would not exist. In other words, materials can become either enablers or obstacles for scientific and technological advancement. Thus, the primary aim of materials science and engineering is gaining a better understanding of the properties of matter and the processes that will combine those properties into

synergistic materials with the characteristics required for a given application.

In order to understand the phenomena that govern material behavior, scientists typically develop and perform countless experiments to determine the properties of interest, such as mechanical strength, stiffness, resistance to heat, conductivity of electricity and many others. With recent advances in computer hardware and software, the role of computer simulations in materials science is expanding and is yielding many useful insights. In particular, these virtual experiments with advanced *ab initio* method, within Kohn-Sham density functional theory which is now the most widely used method for electronic structure calculation in condensed matter physics and quantum chemistry can provide understanding of relative stability, chemical bonding, relaxation of atoms, phase transition, electronic, mechanical, optical or magnetic behavior, etc., of new materials.

In line with this approach, in this study, the properties of new materials based on sulfur (S), selenium (Se), tellurium (Te) are studied.

Chalcogenide materials greatly contributed to the development of various applications and have remained a topic of interest of solid state chemists/physicists for many decades. Synthesis processes of metal chalcogenides have greatly improved solid state chemistry methodologies. Gas separation, ion exchange, environmental remediation and energy storage are some of the applications of metal chalcogenides that have been examined so far [37].

Wide band gap makes chalcogenides promising candidates for nonlinear optics applications, particularly in the IR region. Search for new materials that can provide coherent light with tunable frequencies is very important task. Ternary and quaternary metal chalcophosphates are the few classes of materials that are in the main focus of initiatives aimed at developing nonlinear optical crystals as coherent mid-IR sources. The connection of tetrahedral building blocks to metals, in case of thiophosphate, gives rise to a broad structural variety. According to Azam et. al, [38], approximately one third of all known ternary and quaternary structures are acentric and are thus potential nonlinear optical materials [39].

1.4 Objective

The ultimate aim of the current research is to understand the electronic structure of quaternary chalcogenides, as this can contribute to the advancement in optical telecommunications and optical computing devices.

The primary objective of this study is to determine the ground state properties of quaternary chalcogenide materials that have different crystal structures. The main goal is to understand the electronic, optical and thermoelectric properties of quaternary chalcogenide compounds. The initial objective is to determine the

electronic structure of the quaternary chalcogenide materials that have different crystal structures. Once their electronic structure is obtained, the optical properties will be studied in greater detail.

To accurately predict the electronic structure and optical properties of quaternary chalcogenides, the Engel-Vosko GGA (EV-GGA), modified Becke Johnson (mBJ) and GGA+U were applied. The final objective is to obtain the electronic structure, optical and thermoelectric properties of the selected quaternary chalcogenides. The electronic structures (density of states) are evaluated using the *FPLAPW full potential linear augmented plane wave* method, as employed in WIEN2k. In addition, the TE (thermoelectric) properties are evaluated using the *BoltzTraP* code. The objective of the current work is thus:

- To study the electronic properties, such as BS (band structure), TDOS (total density of states) and PDOS (partial density of states), ECD (electronic charge density), and Fermi surface of the aforementioned systems.
- To study the detailed optical response functions, such as imaginary and real part of dielectric functions, refractive index and absorption coefficient.
- To show the thermoelectric properties of quaternary chalcogenide compounds.

Chapter 2

Theoretical Background

2.1 Background

Numerical computational is becoming an essential tools in condensed matter physics and material science due to their ability to describe the material properties. Properties of materials are often not directly accessible from experiments for many reasons. For example, the sample size of certain materials may not sufficiently large enough for certain experiments. One big advantage of computational methods work is to study hypothetical systems that have never been produced. However, as the reliability of computational results is always verified the experimental results, both the computational methods and the experimental methods should considered to be complement to each other.

Computational modeling approach is frequently used to predict complicated physiochemical phenomena to decrease the expense of experimental measurements and to save the labors.

In the last few decades, ability of computer to perform large scale calculations has been significantly increased. Understanding the behavior of interacting electrons in a solid possess a substantial importance in scientific as well as in technological applications. However, to treat the interacting electronic problem by means of many-body wave functions is very complicated task due to the large number of degrees of freedom. Therefore we need an approximation to solve this problem. This fact leads to two types of approaches; the first one is based on the wave function description. The second approach is the DFT developed by Hohenberg and Khon (H-K), which is based on the electron density. The following chapter is a brief overview of Density Functional Theory, and its role in solving the quantum mechanical problems.

2.2 The Many-Body Problem

The main aim of this work is to understand and investigate the properties of real materials, which necessitates an appropriate quantum-mechanical description of these systems. However, a quantum mechanical understanding of a given material system begins with a many-electron Schrödinger equation and its corresponding Hamiltonian:

$$\hat{H}\psi = E\psi. \quad (2.2.1)$$

Solids consist of heavy positively charged nuclei (n) and light negatively charged electrons (e). The many-body Hamiltonian can be written as :

$$\hat{H} = -\frac{\hbar^2}{2} \sum_i \frac{\nabla_{\vec{R}_i}^2}{M_i} - \frac{\hbar^2}{2} \sum_i \frac{\nabla_{\vec{r}_i}^2}{m_e} - \frac{1}{4\pi\epsilon_0} \sum_{i,j} \frac{e^2 Z_i}{|\vec{R}_i - \vec{r}_j|} + \frac{1}{8\pi\epsilon_0} \sum_{i \neq j} \frac{e^2}{|\vec{r}_i - \vec{r}_j|} + \frac{1}{8\pi\epsilon_0} \sum_{i \neq j} \frac{e^2 Z_i Z_j}{|\vec{R}_i - \vec{R}_j|}. \quad (2.2.2)$$

In the above Eq. (2.2.2), M_i is mass of nucleus at \vec{R}_i while m_e is the mass of the electron positioned at \vec{r}_i . The first and second term correspond to the kinetic energy operator of the nuclei and of the electrons, respectively, while the remaining terms describe the Coulomb interaction between electrons and nuclei, among electrons and among nuclei, respectively.

Given the wave functions $\psi(\vec{R}, \vec{r})$ with $\vec{R} = [\vec{R}_i | i = 1, \dots, N_n]$ and $\vec{r} = [\vec{r}_i | i = 1, \dots, N_e]$, the Schrödinger equation may be written as:

$$\hat{H}\psi(\vec{R}, \vec{r}) = E\psi(\vec{R}, \vec{r}). \quad (2.2.3)$$

However, due to the high degree of complexity, solving this equation and requires some approximations.

2.3 Level 1: The Born-Oppenheimer Approximation

Electrons have much smaller mass than a nucleus but have comparable electromagnetic forces acting on them. The nuclei, having large mass, move more slowly than do electrons. More specifically, given the electronic motion – the nuclear motion of the nuclei ($\approx 10^3 m/s$) and the electronic motion of electron ($\approx 10^6 m/s$) – it is assumed that, at any moment, the electrons will be in their ground state with respect to the instantaneous nuclear configuration.

Under this assumption, the electron wave function is a solution of the Schrödinger equation for electrons with the external potential produced by the nuclei in fixed nuclear positions:

$$\hat{H} = -\frac{\hbar^2}{2} \sum_i \frac{\nabla_{\vec{r}_i}^2}{m_e} - \frac{1}{4\pi\epsilon_0} \sum_{i,j} \frac{e^2 Z_i}{|\vec{R}_i - \vec{r}_j|} + \frac{1}{8\pi\epsilon_0} \sum_{i \neq j} \frac{e^2}{|\vec{r}_i - \vec{r}_j|} + \frac{1}{8\pi\epsilon_0} \sum_{i \neq j} \frac{e^2 Z_i Z_j}{|\vec{R}_i - \vec{R}_j|}. \quad (2.3.1)$$

This Hamiltonian (H) relates to the electronic motion in the external potential (V_{ext}) that is produced by the nuclei and can be expressed as:

$$\hat{H} = -\frac{\hbar^2}{2} \sum_i \frac{\nabla_{\vec{r}_i}^2}{m_e} - \frac{1}{4\pi\epsilon_0} \sum_{i,j} \frac{e^2 Z_i}{|\vec{R}_i - \vec{r}_j|} + \frac{1}{8\pi\epsilon_0} \sum_{i \neq j} \frac{e^2}{|\vec{r}_i - \vec{r}_j|}. \quad (2.3.2)$$

$$\hat{H} = \hat{H}_e + \hat{V}_{NN} \quad (2.3.3)$$

Eq. (2.3.2) represents electron Hamiltonian, whereby the nuclear repulsion (\hat{V}_{NN}) contributes to the total energy by a constant amount. Hence, removing this term from the Hamiltonian would not affect the corresponding wave function. The separate treatment of electronic and nuclear motion is known as the Born-Oppenheimer approach.

It can be seen from the Hamiltonian that the solution of the electronic SE is highly complex. Therefore, the quantum mechanical calculations must be simplified, which can be achieved by reducing the many-electron Hamiltonian to a physically equivalent/similar system that can be solved analytically. In this work, Density Functional Theory (DFT) is used to solve the Schrödinger equation.

2.3.1 Level 2: Density Functional Theory

Since the development of its theoretical foundations in the mid-1960s, DFT has been used in computational solid state physics to calculate ground state properties of real materials.

In 1964, Hohenburg and Khon [40] proved that, if the charge density of a system is known, all its properties can be determined.

2.3.2 Hohenberg-Kohn (H-K) Theorem

The first theorem developed by Hohenburg and Khon demonstrates one-to-one correspondence between external potential $v_{ext}(r)$ and electron density $n(r)$.

Thus, with the exception of the constant energy shift, the ground state particle density determines the full Hamiltonian. In principle, all the states – including ground and excited states of the many-body wave-functions – can be calculated. This assertion implies that the ground state particle density determines all properties of the system uniquely and completely.

The second theorem posits that the variational principle allows calculating the $n_0(r)$ (ground state electron density).

The proof of the first theorem is based on the minimum energy principle, which can be proved by taking $n(r)$ as a functional to obtain $v_{ext}(r)$ and the total electronic Hamiltonian. This approach makes the DFT more systematic and thus superior to the Thomas-Fermi model. Using the principle of reductio ad absurdum, one can more easily and simply derive its proof for a non-degenerate system. Consider a box containing a collection of electrons, influenced by $v_{ext}(r)$. Suppose that $v_{ext}(r)$ and all properties are determined by a known electron density $n(r)$. In addition, consider another external potential $v'(r)$ that differs from $v(r)$ by more than a constant and is calculated from the same $n(r)$ for the ground state. This allows two different Hamiltonians \hat{H} and \hat{H}' having same ground state electron density ($n_0(r)$) and different normalized wave functions to be obtained. This may be expressed as:

$$E'_0 < \langle \psi' | \hat{H} | \psi' \rangle < \langle \psi' | \hat{H}' | \psi' \rangle + \langle \psi' | \hat{H} - \hat{H}' | \psi' \rangle < E'_0 + \int n_0(r) [v_{ext}(r) - v'_{ext}(r)] dr, \quad (2.3.4)$$

where E_0 and E'_0 represent the $n_0(r)$ for \hat{H} and \hat{H}' , respectively. In addition, we can write:

$$E'_0 < \langle \psi | \hat{H}' | \psi \rangle < \langle \psi | \hat{H} | \psi \rangle + \langle \psi | \hat{H}' - \hat{H} | \psi \rangle < E_0 - \int n_0(r) [v_{ext}(r) - v'_{ext}(r)] dr. \quad (2.3.5)$$

By adding Eq. (2.3.4) and Eq. (2.3.5), a contradiction is revealed, as $E_0 + E'_0 < E'_0 + E_0$. As a result, it is possible that no two different $v(r)$ can give the same $n_0(r)$.

Now, if $v(r)$ is known, the energy E_v as a function of the $n_0(r)$ (electron density) may be given as:

$$E_v[n] = T[n] + V_{ne}[n] + V_{ee} = \int n(r)v_{ext}(r)dr + F_{HK}[n]. \quad (2.3.6)$$

Whereas

$$F_{HK}[n] = T[n] + V_{ee}[n], \quad (2.3.7)$$

here, $F_{HK}[n(r)]$ is a universal functional and $F_{HK}[n(r)]$ is a known three-dimensional functional $n(r)$. Thus, it is possible to obtain both $n_0(r)$ and density in a given $v_{ext}(r)$. However, in a many-body system, the problem becomes more complex, as there is a need to determine the $F_{HK}[n(r)]$ exactly. In the second H-K theorem, it is stated that $n_0(r)$ is achievable by variational principle and can be written as:

$$E_0[n_0] \leq E_v[n] \quad (2.3.8)$$

Let ψ be the ground state wave function related to electron density. This allows the external potential $v(r)$ to be evaluated uniquely. If we consider another wave-function ψ' related to electron density $n'(r)$, it follows:

$$(\psi'|\hat{H}'|\psi') = \int n'(r)v(r)dr + F_{HK}[n'] = E[n'] \geq E[n]. \quad (2.3.9)$$

This shows that, by minimizing the total energy functional of the system with respect to variations in the density $n(r)$, the exact ground state density and energy can be obtained.

2.3.3 The Kohn-Sham (K-S) Equations

Kohn and Sham presented a transformation of DFT to practical electronic structure theory [41]. The functional $F_{HK}[n(r)]$ can be written as:

$$F_{HK}[n(r)] = T_s[n(r)] + E_H[n(r)] + E_{XC}[n(r)]. \quad (2.3.10)$$

Which (Eq. (2.3.6))becomes:

$$E[n(r)] = F_{HK}[n(r)] + \int n(r)v_{ext}(r)dr = T_s[n(r)] + E_H[n(r)] + E_{XC}[n(r)] + \int n(r)v_{ext}(r)dr. \quad (2.3.11)$$

The exchange and correlation energy E_{XC} accounts for all the many-body effects. Thus, subject to the constraint that the number of electrons N is conserved, the following holds:

$$\delta F_{HK}[n(r)] + \int n(r)V_{ext}(r)dr - \mu \left(\int n(r)dr - N \right) = 0. \quad (2.3.12)$$

And the resulting equation is:

$$\mu = \frac{F_{HK}[n(r)]}{\delta(n(r))} + V_{ext}(r) = \frac{\delta T_S[n(r)]}{\delta(n(r))} + V_{KS}(r), \quad (2.3.13)$$

where μ is the chemical potential. Moreover,

$$V_{KS} = V_{ext}(r) + V_H(r) + V_{XC}(r). \quad (2.3.14)$$

Is the KS one-particle potential with the Hartree potential $V_H(r)$ given by:

$$V_H = \frac{\delta E_H(n(r))}{\delta(n(r))}, \quad (2.3.15)$$

where $V_{XC}(r)$ is the exchange-correlation potential and is given as:

$$V_{XC}(r) = \frac{\delta E_{XC}[n(r)]}{\delta n(r)}. \quad (2.3.16)$$

This leads to one-electron Schrödinger-like equation:

$$[-\frac{1}{2}\nabla^2 + V^{eff}]|\psi_i|^2 = \epsilon_i\psi_i, \quad (2.3.17)$$

where ψ_i represents the K-S one-electron orbitals, and the $n(r)$ can be presented as:

$$n(r) = \sum_{i=1}^N |\psi_i|^2. \quad (2.3.18)$$

The Kohn-Sham one-electron orbital energies are represented by ϵ_i 's. Its format resembles that of the Hartree-Fock-like single particle equation. Additionally, the total energy can be found from the density, using the expression below:

$$E = \sum_{i=1}^N \epsilon_i - \frac{1}{2} \int \int \frac{n(r)n(r')}{r-r'} + E_{XC}[n] - \int v_{XC}(r)n(r)dr. \quad (2.3.19)$$

Equations Eq. (2.3.13), Eq. (2.3.17) and Eq. (2.3.18) are the K-S equations and have to be solved self-consistently. For example, suppose the electron density has a known value, determine the μ using Eq. (2.3.19), allowing the K-S orbitals to be obtained. Based on these orbitals, a new density is obtained from Eq. (2.3.18). and the process has to be repeated until convergence is achieved. Subsequently, the total energy may be calculated from Eq. (2.3.19). using the final electron density.

The exact ground state density and total energy could potentially be obtained if all terms in the K-S energy functional were known. However, the exchange-correlation (XC) functional E_{XC} is unknown. More specifically, it contains the non-classical part of the electron-electron interaction, along with the part of the system kinetic energy, which differs from that of the auxiliary non-interacting system.

An approximation to the E_{xc} is given in the next section.

2.3.4 Exchange Correlation Functional $E_{XC}[n]$

Density functional theory with K-S equation provides a scheme that can be applied in order to reduce the many-body problem to a Schrödinger-like effective single-particle equation. However, this approach is also hindered by several problems, one of which pertains to the exchange-correlation energy E_{XC} the exact form of which is not known and requires approximation. The simplest and historically the first approximation of E_{XC} is the Local Density Approximation (LDA).

2.3.5 The Local Density Approximation (LDA)

The oldest approximation is the LDA which defines the exchange-correlation functional as:

$$V_{XC}^{LDA}[n(r)] = \int n(\vec{r})\epsilon_{XC}(n(\vec{r}))d\vec{r}, \quad (2.3.20)$$

here ϵ_{XC} stands for the exchange-correlation function (not functional) for the homogeneous electron gas with interacting electrons and is numerically known from Monte Carlo calculations. The underlying idea is very simple. At each point in space the exchange-correlation energy is approximated locally by the exchange-correlation energy of a homogeneous electron gas with the same electron density as present at that point. LDA is based on the local nature of exchange-correlation and the assumption that the density distribution does not vary too rapidly. In spite of its simplicity, LDA performs quite well even for more realistic systems.

2.3.6 The gradient Generalized Approximation

As mentioned above, the LDA neglects the inhomogeneity of the charge density. To overcome this deficiency, generalized-gradient approximations (GGA) was developed. It includes density gradient corrections of the electron density and gives better results than LDA in many cases.

This resulting XC functional can be written as

$$E_{XC}^{GGA} = \int f_{XC}(n(r), |\nabla n(r)|n(r))d(r), \quad (2.3.21)$$

where f_{XC} can be split into exchange contribution (f_X) and correlation contribution (f_C) as $f_{XC} = f_X + f_C$.

2.3.7 modified Becke-Johnson potential (mBJ)

Both the LDA and GGA can reproduce the band structure even in cases of complex metallic systems. However, neither is successful in reproducing the exact band gap for semiconductor materials.

As LDA and GGA cannot produce a band gap of comparable value to that obtained experimentally, Becke and Johnson (BJ) developed a BJ potential [44], that improves the band gap in comparison with LDA and GGA functionals. It can be formulated as:

$$V_{x,\sigma}^{BJ}(r) = V_{x,\sigma}^{BR}(r) + \frac{1}{\pi} \frac{\sqrt{5}}{6} \frac{\sqrt{t_\sigma(r)}}{\rho_\sigma(r)}, \quad (2.3.22)$$

where ρ_σ denotes electron density and can be defined as: $\rho_\sigma = \sum_{i=1}^{N_\sigma} |\psi_{i,\sigma}|^2$ and t_σ represents kinetic energy density and can be defined as: $t_\sigma = \sum_{i=1}^{N_\sigma} \nabla \psi_{i,\sigma}^* \nabla \psi_{i,\sigma}$

$$V_{x,\sigma}^{BR}(r) = -\frac{1}{b_\sigma} (1 - e^{-x_\sigma(r)} - \frac{1}{2} x_\sigma(r) e^{-x_\sigma(r)}). \quad (2.3.23)$$

Blaha et al. [43] modified the exchange and correlation potential of the BJ [44] approach, and developed the mBJ potential, capable of better reproducing the experimental gap of semiconductors relative to the LDA or the GGA. The mBJ potential is given by:

$$V_{x,\sigma}^{mBJ}(r) = cV_{x,\sigma}^{BR}(r) + (3c - 2) \frac{1}{\pi} \frac{\sqrt{5}}{12} \frac{\sqrt{2t_\sigma(r)}}{\rho_\sigma(r)}, \quad (2.3.24)$$

where $\rho_\sigma(r)$, $t_\sigma(r)$ and $V_{x,\sigma}^{BR}(r)$ are the spin-dependent density of states, kinetic energy density and the Becke-Roussel potential (BR), respectively.

In the TB-mBJ, the value of c is calculated by:

$$C = \alpha + \beta \left(\frac{1}{V_{cell}} \int_{cell} \frac{|\nabla \rho(r')|}{\rho(r')} \right)^{\frac{1}{2}}, \quad (2.3.25)$$

where V_{cell} is the unit cell volume, an α and β are the free parameters with the value of -0.012 and 1.023 Bohr, respectively. The only disadvantage of the TB-mBJ potential is that the derivative of a XC functional cannot be obtained. Consequently, this potential cannot be used for the calculation of forces that act on the nuclei, which is required for the optimization of the geometry.

2.3.8 Self-Consistent Kohn-Sham (K-S Scheme)

Iterative procedure has to be adopted to obtain the solution to the K-S equation, as the effective potential is density dependent. According to this procedure, an initial guess for density is obtained using Hartree potential in XC, whereby applying the density functional method, its potential can be derived from the relationship between the total energy E and the density. New density, K-S potential and total energy are obtained on the basis of newly generated set of K-S orbitals that resulted from

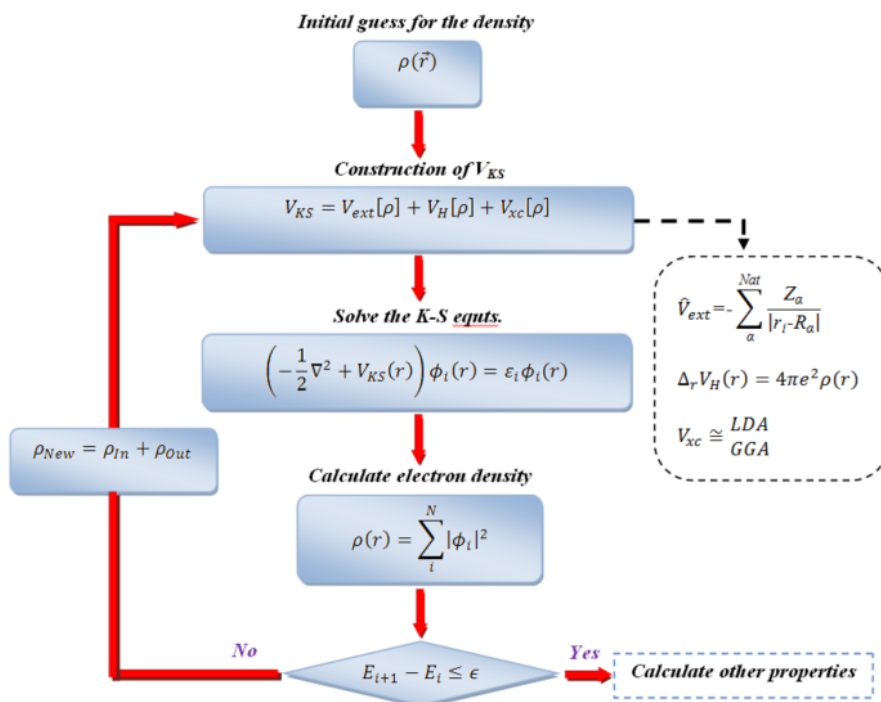


Figure 2.1: Self-consistent K-S scheme.[42]

the solution of equations using the currently developed information. These steps are repeated until no change is observed between the output and input densities. A typical K-S self-consistent scheme is defined in Fig. (2.1).

Chapter 3

Band structure method

In the previous chapter, we have shown that from Kohn-Sham equation one can determine both energy and density of ground state of a many-body system. However the problem is how to get the ψ which determines the $n(r)$ and kinetic energy?

One of the most efficient solutions is to expand the single-particle wave-function in the form of basis function and Bloch theorem. Set of plane waves is a best choice for a set of this function. For calculating Hartree-potential it has been proven that the plane wave is diagonally behave to the Laplace-operator (Δ), which consist of the operator of kinetic energy and Poisson relation (see Fig 3.2). Though, it has been found that oscillations of the charge density and wave-function around electrons are very fast and to get the precise results enough number of plane-waves are required. One way to cope with this problem is to use modified potential around the atoms so as to avoid rapid oscillations of charge-density, which recalls a group of pseudo potential methods. Another way is rest on the space separation and the use of suitably modified basis-functions for different regions of space, is the FP-LAPW, which is a method used in the calculations of our present work.

In this section we are going to present a small introduction into a newly developed scheme for solving the K-S equation with the FP-(L)APW+lo formalism. We introduce a brief description of Bloch theorem, the original method of LAPW, APW and the concept of FP-(L)APW+lo method.

To go in a detail, in Fig. (3.1), we presented a schematic overview of the electronic structure methods that shows a spectrum of methods. These methods each of them requires for many purposes, geometries, applications and symmetries requiring different approximations.

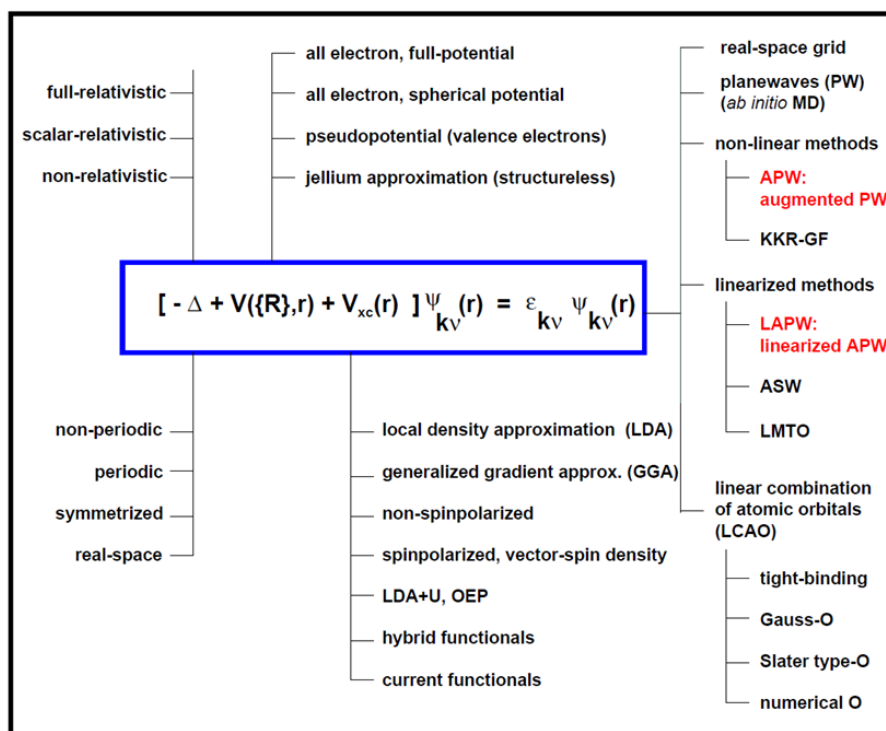


Figure 3.1: Schematic overview of the electronic structure methods that shows a spectrum of methods. Which are developed for many purposes, geometries, applications and symmetries requiring different approximations. [45]

3.1 Blochs Theorem

Bloch's theorem [46] proves that if the potential V has translation symmetry, we can write any eigenfunction $\psi(r)$ as a product of a function $\mu(r)$, having periodicity for plane wave $e^{ik \cdot r}$ may be written as:

$$\psi_{j,k} = \mu_j(r) e^{ik \cdot r}. \quad (3.1.1)$$

The function μ_j , possesses the periodicity of the potential. In Eq. (3.1.1) j and μ_j are the band index and wave vector confined to the first Brillouin Zone (BZ). Moreover the μ_j can expand it in terms of a Fourier series as:

$$\mu_j(r) = \sum_G C_{j,G} e^{iG \cdot r}, \quad (3.1.2)$$

where the G (i.e. the reciprocal lattice vector) defined by $G \cdot R = 2\pi m$. The $\psi_{j,k}$ (i.e. the electron wave functions) may be written as a linear combination of plane waves:

$$\psi_{j,k} = \sum_G C_{j,k+G} e^{iG \cdot r}. \quad (3.1.3)$$

Given that each electron occupies a state of definite k , the infinite number of electrons within the solid gives rise to an infinite number of k -points.

3.2 Augmented Plane Wave Scheme

This method is based on Slater [47] observation that:

- Electrons will strongly be bound closer to the nucleus. The electrons behave similarly as in a free atom and can be efficiently described by atomic functions.
- Far away from nuclei, electrons are nearly free in space and can suitably be described by plane waves.

The whole space has been divided into muffin-tin (MT) spheres (spheres centered at each atomic site) and interstitial (I) region (see (Fig. (3.2)a).

Within the MT potential is considered to be spherically symmetric in shape, while potential is kept constant in the interstitial area. Different Basis sets are used in two different regions (see Fig. (3.2)b):

$$\phi = \left[\begin{array}{cc} \frac{1}{\sqrt{\Omega}} e^{i(G+\vec{k}) \cdot r} & (r \in I) \\ \sum_{lm} A_{lm} u_l^\alpha(r, E_l) Y_{lm}(\hat{r}) & (r \in Mt) \end{array} \right]. \quad (3.2.1)$$

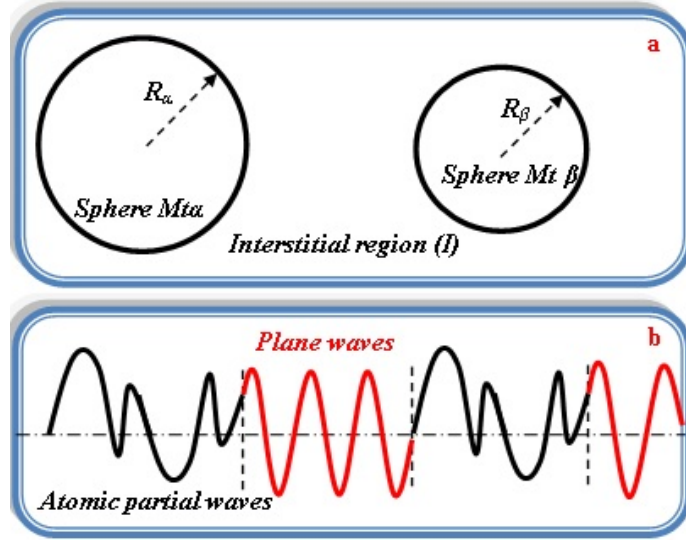


Figure 3.2: Schematic division of (a) Space into Muffin-tin spheres and an interstitial region. b) Wave function in to black atomic partial waves in the MT sphere and red plane waves in I region [42]

Where, Ω is the cell volume, u_l atomic radial function, Y_{lm} spherical harmonic and A_{lm} coefficients, which we can calculate, by requiring that the wave-function is continuous in the Mt spheres boundary.

$$A_{lm} = \frac{4\pi i^l}{\sqrt{\Omega} U_l(R_\alpha)} \sum_G J_l(|k+g|R_\alpha) Y_{lm}^*(k+g). \quad (3.2.2)$$

In the interstitial region the plane waves solve SE in a constant potential. In the MT spheres, the spherical harmonics times radial function is a solution of SE in a potential $V(r)$ and energy E_l :

$$-\frac{1}{r^2} \frac{d}{dr} \left(r^2 \frac{du_l}{dr} \right) + \left(\frac{l(l+1)}{r^2} + V(r) - E_l \right) r u_l = 0. \quad (3.2.3)$$

The biggest disadvantage of the APW scheme is that the factor E_l in Eq. (3.2.1) which is required to get the Eigen-state $\psi_{kn}(r)$ is unknown, and requiring the E_l 's to be the same as the band energies. The APW method cannot get this energy from the diagonalization of the Hamiltonian matrix. The radial function u_l 's depend on the band energies, hence, the secular equation becomes a nonlinear problem. One has to set a trial energy for E_l , obtaining the APW basis by solving Eq. (3.2.3), to set up the matrix elements and to compute the determinant $|H - ES|$ (see Fig. (3.3)). If the Eigen energy is not equal to E_l , then the trial energy must be selected until the Eigen energy becomes equal to E_l (see Fig. (3.4)). This makes the APW method inefficient. Another disadvantage is that, when u_l in Eq. (3.2.2) becomes zero, the radial function and the plane wave become decoupled. That means there is no

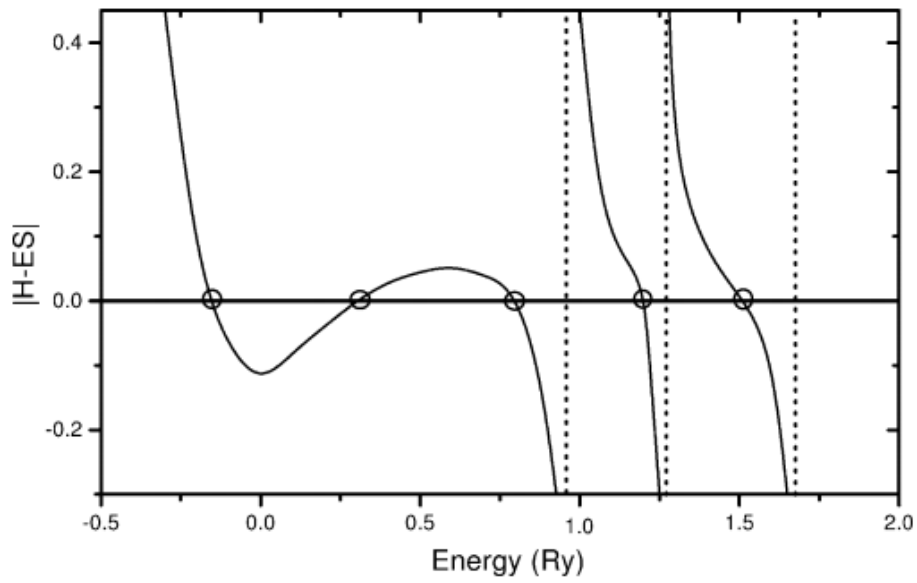


Figure 3.3: Satisfying the secular equation $|H - ES| = 0$ in APW by numerically finding the zeros [48]

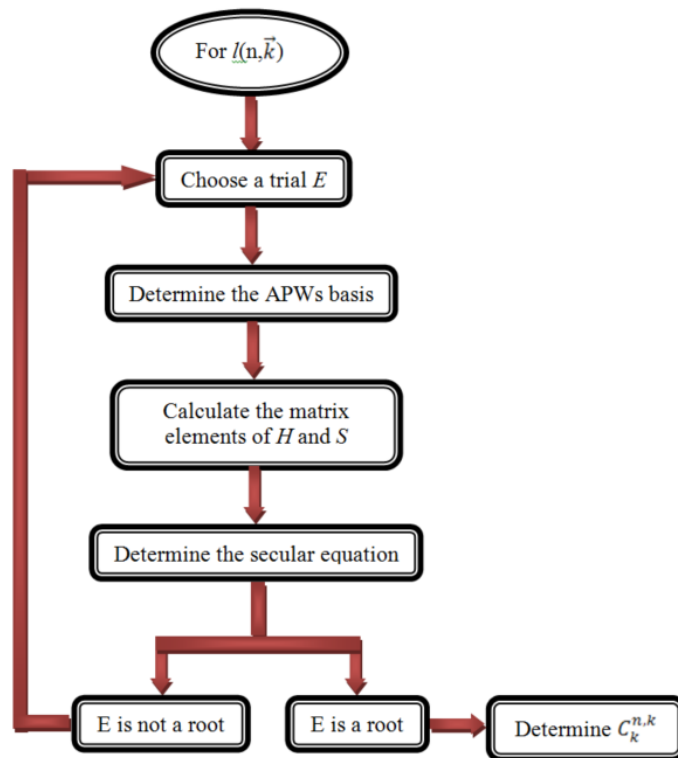


Figure 3.4: Flowchart of APW method.[42]

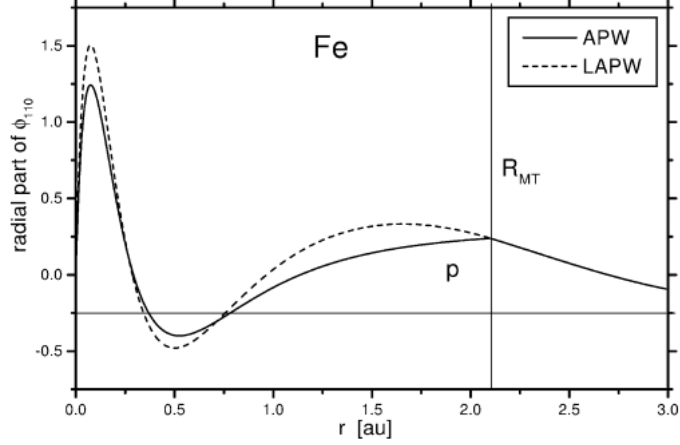


Figure 3.5: Augmentation of a PW by a p-like partial wave inside the iron atomic sphere by APW (kink) and by LAPW (smooth derivative)[48]

continuity between the radial function and the plane wave in the boundary of MT sphere (see Fig. (3.2)b).

3.3 The Concept of LAPW Method

To avoid the non-linearity of the problem and the discontinuity in the APW technique, the linearized plane wave LAPW technique was developed [49], [50]. The radial function u_l within Mt sphere be supplemented by their energy derivative ($\dot{u}_l = \frac{\partial u_l}{\partial E_l}$) however, u_l and \dot{u}_l can be calculated at a fixed energy E_l (see Fig. (3.5)). In the LAPW method the basis set in the interstitial part is almost same as in APW method, while in the MT spheres, the basis function depends on u_l as well as on its energy derivative:

$$\phi = \begin{bmatrix} \frac{1}{\sqrt{\Omega}} e^{i(G+\vec{k})r} & (r \in I) \\ \sum_{lm} [A_{lm} u_l^\alpha(r, E_l) + B_{lm} \dot{u}_l^\alpha(r, E_l)] Y_{lm}(\hat{r}) & (r \in Mt) \end{bmatrix}, \quad (3.3.1)$$

the A_{lm} and B_{lm} are the coefficients and can be calculated because u_l as well as \dot{u}_l are continuous at the Mt spheres border is calculated from SE , by taking the energy derivative of Eq. (4.7) with respect to E_l :

$$-\frac{1}{r^2} \frac{d}{dr} (r^2 \frac{du_l}{dr}) + (\frac{l(l+1)}{r^2} + V(r) - E_l) r \dot{u}_l = r u_l. \quad (3.3.2)$$

Furthermore, if u_l is zero at the sphere boundary, its radial derivative is in general non zero. Hence, the boundary conditions can always be satisfied and there is no asymptote problem. Now if there is a change in the E_l from band energy ϵ , then linear arrangement may replicate the APW radial function which is constructed at

the band energy as follow:

$$u_l(\epsilon, r) = u_l(E_l, r) + (\epsilon - E_l)\dot{u}_l(E_l, r) + O((\epsilon - E_l)^2). \quad (3.3.3)$$

Some materials contain chemical elements with states between band and core states. Such state are called semi core states.

$$\phi = \left[\begin{array}{c} 0 \\ \sum_{lm} [A_{lm}u_l^\alpha(r, E_l) + B_{lm}\dot{u}_l^\alpha(r, E_l^1) + C_{lm}u_l^\alpha(r, E_l^2)]Y_{lm}(\hat{r}) \\ 0 \end{array} \begin{array}{l} (r \in I) \\ (r \in Mt) \end{array} \right]. \quad (3.3.4)$$

This LO remains zero in the interstitial and Mt sphere regions of the other atoms. The coefficients (A_{lm} , B_{lm} and C_{lm}) can be calculated by requiring that LO approaches smoothly zero at the Mt boundary.

3.4 The full-potential liner augmented plane wave method (FP-LAPW)

Since 1970, the muffin-tin approximation is frequently used in the APW and LAPW techniques. Let us recall that MT approximation means that the potential is constant in the interstitial region, while is spherical symmetric elsewhere. This approximation is efficient in highly coordinated systems such as the face centered metallic structures but for the covalent bonded and open structure solids is not very efficient. So, to obtain better predications for these (covalent bonded and open structure solids) compounds, shape approximation must not be used. These systems are treated with FP-LAPW method.

This method combines the LAPW basis with the treatment of the full potential (FP) in both Mt and interstitial regions [18]. In this approach the potential is expanded in both parts of the unit cell in the following way

$$V(\vec{r}) = \sum_{LM} V_{LM}(r)Y_{LM}(\vec{r}). \quad (3.4.1)$$

$$V(\vec{r}) = \sum_K V_K \exp(i\vec{K} \cdot \vec{r}). \quad (3.4.2)$$

Where Eq. (3.4.1) and Eq. (3.4.2) are for inside the atomic sphere and outside the atomic sphere, respectively. This form is termed as the FP (full-potential) scheme.

3.5 Technical Parameters: Energy Cutoff and K-mesh

In order to measure the accuracy in the computational results depends on l_{max} , E_{cut} (cutoff energy) and the k-points (k-mesh) are considered an important basis set

parameters in the DFT codes for the solid state calculations. In DFT calculations these parameters should be used in order to balance the computational load and accuracy.

In order to construct the wave functions, we use the plane waves. Generally using more plane waves results in better results. But for the computation mechanism the wave functions, using the infinitely plane wave are not necessary. We have to limit the energy cutoff that defines the number of plane waves used. The equations between plane wave coefficient and energy cutoff is given below

$$E_{cut} = \frac{\hbar K_{max}^2}{2m_e}. \quad (3.5.1)$$

Based on the K_{max} , the ψ is written as

$$\psi_{k_n}(r) = \sum_K^{K_{max}} C_{K,k_n} e^{i(k+K).r}. \quad (3.5.2)$$

In FPLAPW, the E_{cut} is used in the interstitial region.

The l_{max} parameter, controls the size of the LAPW augmentation which consists of an infinite sum over angular momenta l . This summation will be truncated at l_{max} . While the the plane wave cutoff K_{max} parameter, determines the size of the basis set. Only those basis functions with a $|\vec{K}|$ that satisfies the condition $|\vec{K}| \leq K_{max}$. k_{max} are included in the basis set. As a consequence, l_{max} and k_{max} control the accuracy of the calculation (completeness and quality). Good choices for these parameters are therefore very important.

So, evaluating the Kohn-Sham equations requires many system quantities i.e., the charge density to be integrated over the Brillouin Zone (BZ).

$$\int_{IBZ} \frac{1}{\Omega_{IBZ}} dk \rightarrow \sum_k \omega_k. \quad (3.5.3)$$

Hence, using the more k-mesh, the integrand will be more accurate. Similarly as in case of E_{cut} , we should also find an optimum k-mesh at which the quantities of interest are converged. Commonly there exist two kinds of methods to get the k-points. (a) tetrahedron method and (b) the special k-point method. Here we use the last one, which produce a grid of uniform k-points in the BZ.

3.6 Structure of the WIEN2k code

All calculations performed in this work utilized WIEN2k code, version 13 [55]. This package is based on the full potential linearized augmented plane wave (FPLAPW) method for solving the DFT problems, considered one of the most accurate methods.

WIEN2k provides user-friendly environment that ensures that calculations can be easily implemented. In addition, crystal structure and symmetry can be developed either manually or data can be imported from a crystallographic database. On the basis of self-consistent calculations, several other packages are used to perform physical properties calculations from the obtained ground state density, including total and projected density of states, optical and phonon properties, atomic sites, energy band structure and X-ray absorption and emission spectra.

The basis set for WIEN2k is augmented plane waves that represent the electrons of a periodic crystalline system [51]. Spherical harmonics in the non-overlapping region centered at the atomic sites and block plane waves in the interstitial area between nuclei are part of this set. The intersection point of the two regions is muffin-tin radii. At the beginning of the calculation, such radius is chosen to restrict the core state electrons to atomic nucleus and allow semi-core and valence electrons to delocalize, forming plane waves. A converged set is produced to reduce number of basis set functions, whereby WIEN2k augments the basis sets with local orbitals, namely constructed radial functions that are constrained by an appropriate choice of coefficients to zero magnitude and radial derivative at the muffin-tin radius of a particular nucleus. System of plane waves is represented diagonally and achieves continuity at muffin-tin radii. These new basis sets are utilized to calculate the state density required to iteratively solve the DFT problem.

WIEN2k only determines the basis sets at discrete positions in reciprocal space, known as k-space. Therefore, mesh of k-points must be specified prior to commencing calculations. Parallel calculations can be performed over a number of processors as the k-points are discretely distributed. This approach allows WIEN2k to rapidly process a large grid of k-points if sufficient resources are available. Once the calculations are complete and a converged density of states is achieved, the output is compared with the actual experimental data in order to validate the results obtained. By comparing these results, it is possible to assess the validity of the proposed crystal structure used for the DFT calculation. If there is a sufficient agreement, the DFT calculation can be used as an aid in interpreting experimental results, such as the identification of secondary peaks from hybridizing atoms in an X-ray emission spectrum.

The process described above is depicted in the flow chart of WIEN2K given in Fig. (3.6).

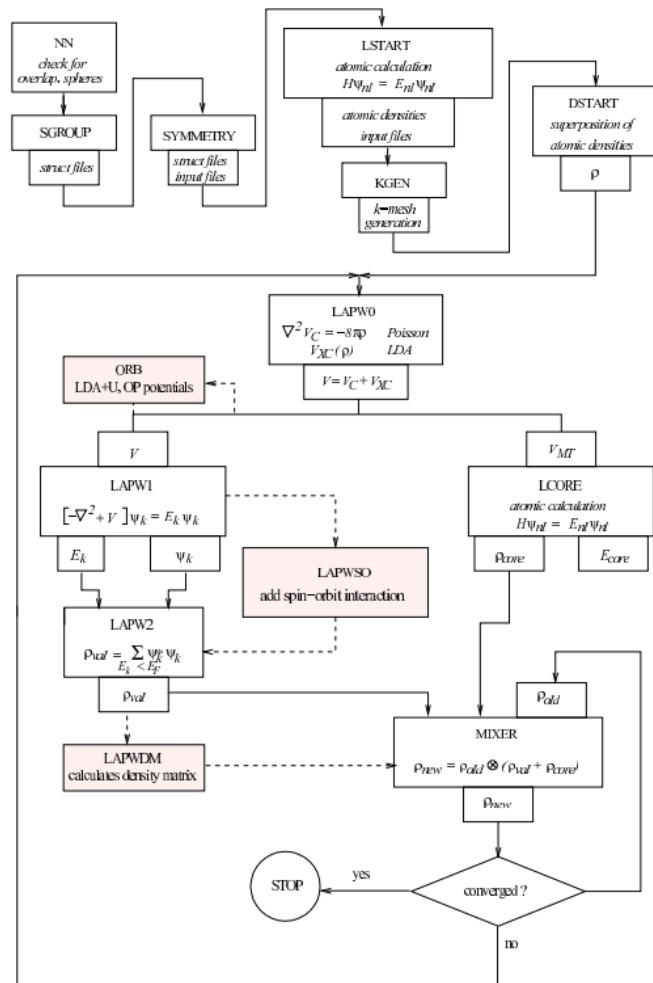


Figure 3.6: Wien2k flow chart[55]

3.7 Theory of Optical Properties (OP)

The OP of solid materials provide a significant means for studying localized defects, excitons, lattice vibrations, energy band structure, impurity levels, and certain magnetic excitations. The light interacts with matter in many ways, whose effects are of great interest for materials. For example, when light of a particular energy falls on the material surface, transition of electrons takes place between the occupied valence bands and the unoccupied conduction bands. These transitions act as a source of information about the energy bands, as energy-dependent optical properties are related to the band structure. Complex dielectric function (Eq. (3.7.1)) is one of the most important optical characteristic of materials

$$\varepsilon(\omega) = \varepsilon_1(\omega) + i\varepsilon_2(\omega), \quad (3.7.1)$$

where $\varepsilon_1(\omega)$ and $\varepsilon_2(\omega)$ are the real and imaginary part of the dielectric function. Intra-band and inter-band are the two main transition effects that occur in the dispersion of dielectric function.

3.8 Dielectric Function

3.8.1 Intra-band Transitions

Intra-band transitions are particularly important in metals and contribute mostly to the dielectric function. When electrons are excited from a partly filled band to an empty state within the same band, this excitation is known as the intra-band transition, as shown in Fig. (3.7). If we consider only the electron-phonon interaction, the real band transition is not feasible, as the required momentum changes with the transition to another state in the same band cannot be supplied by the photon. On the other hand, this is possible with simultaneous scattering of mobile carrier by phonon/impurities. Using a classical approach, Drude developed a theory for such an absorption process, which is known as the Drude model.

The main premise behind this model is that, by considering the motion of quasi-free electrons, the dielectric function and the optical conductivity can be determined under the influence of the oscillating electric field vector of the electromagnetic wave.

Moreover, the intra-band absorption can be discussed in terms of classical dispersion theory. For electron of charge e and mass m , the equation of motion is given by:

$$m(\ddot{x} + \gamma\dot{x} + \omega_0^2) = e\vec{E}_0 \exp(i\omega t), \quad (3.8.1)$$

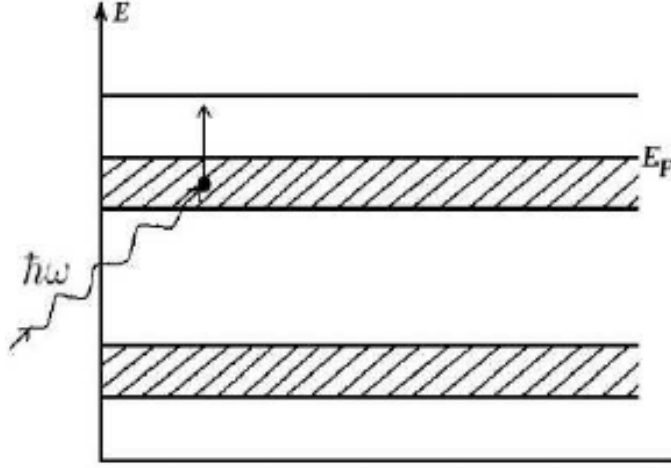


Figure 3.7: Intra-band transition.[56]

where γ is the damping constant and $m\omega_0^2x$ is the restoring force, applicable to electron binding. This leads to the following expressions:

$$\varepsilon_1(\omega) = \varepsilon_1(\omega) + i\varepsilon_2(\omega) = 1 + \frac{4\pi Ne^2}{m} \left[\frac{\omega_0^2 - \omega}{(\omega_0^2 - \omega)^2 + \gamma^2\omega^2} \right]. \quad (3.8.2)$$

While there are no restoring force for free electrons, it can be assessed as a system of oscillators of Eigen frequency $\omega_0 = 0$. Therefore,

$$\varepsilon_1(\omega) = 1 - \frac{4\pi Ne^2}{m} \left[\frac{1}{(\omega^2 + \gamma^2)} \right]. \quad (3.8.3)$$

$$\varepsilon_2(\omega) = 1 - \frac{4\pi Ne^2}{m} \left[\frac{\gamma}{\omega^2(\omega^2 + \gamma^2)} \right]. \quad (3.8.4)$$

While m is replaced by m_{eff} the effective mass and γ by $1/\tau$, where τ denotes the electron-lattice collision time.

$$\varepsilon_1(\omega) = 1 - \frac{4\pi Ne^2}{m_{eff}} \left[\frac{1}{(\omega^2 + \tau^{-2})} \right]. \quad (3.8.5)$$

$$\varepsilon_2(\omega) = 1 - \frac{4\pi Ne^2}{m_{eff}} \left[\frac{1}{\omega\tau(\omega^2 + \tau^{-2})} \right]. \quad (3.8.6)$$

The Drude term includes, when the optical properties of metallic compounds are calculated, hence

$$\varepsilon_2(\omega) = \varepsilon_{inter}(\omega) + \varepsilon_{2intra}(\omega), \quad (3.8.7)$$

$$\varepsilon_{2intra}(\omega) = \left[\frac{\omega_p^2\tau}{\omega(1 + \omega^2\tau^2)} \right], \quad (3.8.8)$$

Where ω_p and τ denote the plasma frequency and the mean free time between collisions, respectively [53]. For the material characterized by anisotropy, the ω_p can be calculated from electronic structure using:

$$\omega_p^2 = \frac{8\pi}{3} e^2 \sum_{kn} \vec{\theta}_{kn} \delta(\epsilon_{kn}), \quad (3.8.9)$$

where ϵ_{kn} is $|E_n \vec{k} - E_F|$ and $\vec{\theta}_{kn}$ is the electron velocity.

Experimentally, the dielectric functions cannot be achieved directly from optical measurements. On the other hand, reflectivity $R(\omega)$, the refractive index $n(\omega)$, and the extinction coefficient $k(\omega)$ can be directly accessed. These experimentally observable quantities are given by:

$$I(\omega) = \sqrt{2}(\omega) \sqrt{\sqrt{\epsilon_1^2(\omega) + \epsilon_2^2(\omega)} - \epsilon_1(\omega)}. \quad (3.8.10)$$

$$L(\omega) = \frac{\epsilon_2(\omega)}{[\epsilon_1^2(\omega) + \epsilon_2^2(\omega)]}. \quad (3.8.11)$$

$$n(\omega) = \frac{\sqrt{\sqrt{\epsilon_1^2(\omega) + \epsilon_2^2(\omega)} + \epsilon_1(\omega)}}{2}. \quad (3.8.12)$$

$$R(\omega) = \left| \frac{\sqrt{\epsilon(\omega)} - 1}{\sqrt{\epsilon(\omega)} + 1} \right|^2. \quad (3.8.13)$$

The above stated dielectric functions are associated with the electric polarization \vec{P} and electric field \vec{E} through the following equation:

$$\vec{P}_i = \epsilon^{ij} \vec{E}^j. \quad (3.8.14)$$

The term ϵ^{ij} is a second rank tensor, having six independent component, $\epsilon^{xx}(\omega)$, $\epsilon^{yy}(\omega)$, $\epsilon^{zz}(\omega)$, $\epsilon^{xy}(\omega)$ and $\epsilon^{yz}(\omega)$, in which some components can be zero, depending on the crystal symmetry. Each of these six components is involved in elucidating the behavior of the dielectric function of the crystals possessing the triclinic symmetry. In the case of monoclinic symmetry, ϵ^{yy} and ϵ^{zz} are equal to zero, while the off-diagonal components are zero, for the tetragonal, trigonal and hexagonal symmetry and $\epsilon^{xx}(\omega) = \epsilon^{yy}$ (these symmetries are referred to as uniaxial). All three diagonal components of the cubic symmetry are equal [54].

In this thesis, hexagonal symmetric, layered transition quaternary chalcogenide is also discussed. This symmetry has three nonzero dielectric components, $\epsilon^{xx}(\omega)$, ϵ^{yy} and ϵ^{zz} with $\epsilon^{xx}(\omega) = \epsilon^{yy}$ [55] and the dielectric properties are measured on the basis of a single crystal. While performing the experiments, the electric field \vec{E} is taken either parallel or perpendicular to the c-axis. The parallel and perpendicular components obtained experimentally are $\epsilon^\perp(\omega)$ and $\epsilon^\parallel(\omega)$, respectively. These components are related to the dielectric components using the equations given below:

$$\frac{\epsilon^{xx} + \epsilon^{yy}}{2} = \epsilon^\perp(\omega). \quad (3.8.15)$$

$$\epsilon^{zz} = \epsilon^\parallel(\omega). \quad (3.8.16)$$

Experiments are usually carried out on polycrystalline samples, as it can be very difficult to grow single crystals. Average or total dielectric function in case of polycrystalline samples can be calculated using the following expressions:

$$\frac{\varepsilon^{xx}(\omega) + \varepsilon^{yy}(\omega) + \varepsilon^{zz}(\omega)}{3} = \frac{2\varepsilon^{\parallel}(\omega) + \varepsilon^{\perp}(\omega)}{3}. \quad (3.8.17)$$

$$\varepsilon_{poly}(\omega) = \varepsilon_{av}(\omega). \quad (3.8.18)$$

All the components of $\varepsilon(\omega)$ are complex.

3.8.2 Direct inter-band transitions

Inter-band transitions (direct and indirect) are the most common phenomena in semiconductors. Dielectric function ($\varepsilon(\omega)$) explores highly useful information about the optical nature of the material. Optical spectra of metals, semiconductors or disordered systems generally have more structures in the energy region between 2.3 ~ 10.0 eV, which are seen in the form of peaks, edges, etc., in the absorption VS energy curve (visible to the far UV region) than the one that arises from Drude absorption, and the plasma oscillations of free electron is accelerated by the electric field of the light wave. These structures emerge when the electrons interact with photons, and thus become excited, allowing them to transition from one band to another. This phenomenon is referred to as inter-band transitions (see Fig. (3.8)).

This type of transition occurs only in insulators, semiconductors or their alloys, because the conduction band is completely unfilled in these materials. The transition takes place from the filled valence band to the unfilled conduction band. For such cases, the Drude absorption is not possible. For this process, it is necessary to develop a quantum transport theory, whereby the electron-photon interaction is treated as the exciting part of the Hamiltonian.

Thus, the total Hamiltonian is given as:

$$H = \frac{1}{2m}(\vec{P} + e\vec{A}) + V\vec{r}. \quad (3.8.19)$$

where \vec{A} is the vector potential of the *EMF* (electromagnetic field), and \vec{P} and $V\vec{r}$ symbolize the momentum and the periodic crystal potential, respectively. The *ist* order perturbation describes the correspondence among the radiation and electrons. It is the time-dependent linear term given by:

$$H_0(\vec{r}, t) = \frac{e}{m}(\vec{A} + e\vec{P}). \quad (3.8.20)$$

The vector potential (i.e. for the plane wave) is given as

$$(\vec{A} = (\vec{A}_0 \hat{e} \exp[i(\vec{k} \cdot \vec{r} - \omega t)] + cc, \quad (3.8.21)$$

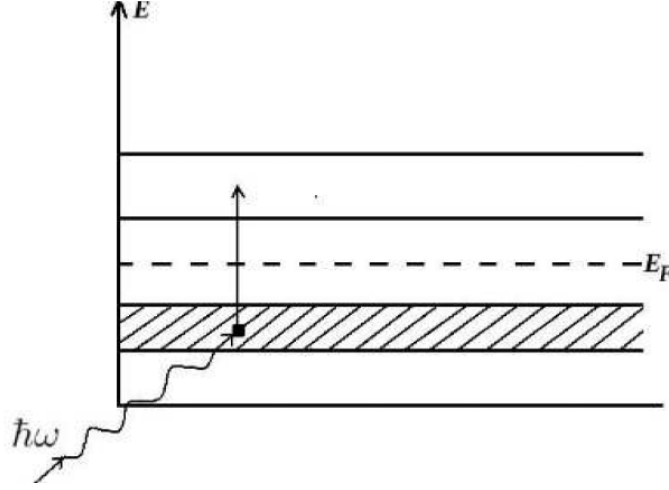


Figure 3.8: Inter-band transition[56]

where cc and \hat{e} are the complex conjugate and unit vector of polarization in electric field. The electron transition probability from an occupied valence band state $E_v(\vec{k}_v)$ to an empty conduction band state $E_c(\vec{k}_c)$ is then

$$W(\omega, t, \vec{k}_v, \vec{k}_c) = \frac{e^2}{m^2 \hbar} \left| \int_0^t dt' \int_V d\vec{r} \psi_c(\vec{k}_c, \vec{r}, t) \vec{A} \cdot \vec{p} \psi_v(\vec{k}_v, \vec{r}, t) \right|^2, \quad (3.8.22)$$

the ψ_v and ψ_c Eigen functions relating to E_v and E_c , Hence,

$$\psi_v(\vec{k}_v, \vec{r}, t) = \exp[-i\hbar E_v(\vec{k}_v)t] \exp(i\vec{k}_v \cdot \vec{r}) \cdot u_v(\vec{k}_v, \vec{r}). \quad (3.8.23)$$

The following equation, along with Eq. (3.8.21), Eq. (3.8.22) and Eq. (3.8.23)

$$\vec{E} = -\frac{\delta \vec{A}}{\delta t}, \quad (3.8.24)$$

results in:

$$W(\omega, t, \vec{k}_v, \vec{k}_c) = \frac{e^2 E_0^2}{m^2 \omega^2} \left| \int_0^t dt' \exp[i\hbar^{-1}(E_c - E_v - \hbar\omega)t'] \vec{e} \cdot \vec{M}_{ev} \right|^2 \quad (3.8.25)$$

In addition,

$$\vec{e} \cdot \vec{M}_{ev} = \int_V d\vec{r} \exp[-i(\vec{k}_c - \vec{k}) \cdot \vec{r}] u_c^* \cdot \delta \exp(i\vec{k}_v \cdot \vec{r}) u_v. \quad (3.8.26)$$

Integrating Eq. (3.8.25) by t' yields:

$$W(\omega, t, \vec{k}_v, \vec{k}_c) = \frac{e^2 E_0^2}{m^2 \omega^2} \left| \frac{\exp[i(E_c - E_v - \hbar\omega)t/\hbar] - 1}{i(E_c - E_v - \hbar\omega)t/\hbar} \vec{e} \cdot \vec{M}_{ev} \right|. \quad (3.8.27)$$

Giving transition probability per unit time, expressed as:

$$\vec{W}_{ev} = \frac{\hbar^2 E_0^2}{2\pi m^2 \omega^2} \int d\vec{k} |\vec{e} \cdot \vec{M}_{ev}|^2 \delta(E_c - E_v - \hbar\omega). \quad (3.8.28)$$

If the difference in energy between final and initial states is the same as the photon energy then the transition probability is different from zero. Various optical constant can be attained, such as the conductivity, given by:

$$\delta(\omega) = 2W_{ev}\hbar\omega/E_0^2. \quad (3.8.29)$$

As a result, the imaginary part is given by:

$$\epsilon_2(\omega) = \frac{4\hbar e^2}{\pi^2 m^2 \omega^2} \int d\vec{k} |\vec{e} \cdot \vec{M}_{ev}|^2 \delta(E_c - E_v - \hbar\omega). \quad (3.8.30)$$

$$\epsilon_2(\omega) = \frac{4\hbar e^2}{\pi^2 m^2 \omega^2} \int d\vec{s} \frac{|\vec{e} \cdot \vec{M}_{ev}|^2}{\vec{\nabla}_k} (E_c - E_v)_{(E_c - E_v)\hbar\omega}. \quad (3.8.31)$$

From the imaginary part $\epsilon_2(\omega)$, the real part can be calculated using the Kramers-Kronig relations:

$$\epsilon_1(\omega) = 1 + \frac{2}{\pi} \int_0^\infty \frac{\omega'}{\omega'^2 - \omega^2} \epsilon_2(\omega') d\omega'. \quad (3.8.32)$$

3.9 Boltzmann Transport Theory

Using the Boltzmann Transport Theory, the thermoelectric transport coefficients can be computed. This theory describes the distribution function $f(n, k)$, produced by an external electric field E and a temperature gradient ∇T . This $f(n, k)$ (distribution function) provides the probability of finding the electron in n (band) with k (wave vector). The Boltzmann equation is given as:

$$-\left(\frac{\partial f^0(n, \vec{k})}{\partial \varepsilon(n, \vec{k})}\right) \vec{v}(n, \vec{k}) \left[\frac{\varepsilon(n, \vec{k})}{T} \nabla T + e\vec{E} - \nabla \mu \right] = -\left(\frac{\partial g(n, \vec{k})}{\partial t}\right)_{SC}, \quad (3.9.1)$$

where the $\partial f(n, k)$, $\varepsilon(n, k)$, $v(n, k)$, T , e , E and μ denote the equilibrium distribution function, energy of an electron, velocity of an electron in band n with wave vector k , temperature, charge of an electron, external electric field, and the chemical potential, respectively. In the above equation, the $g(n, k)$ represents the difference between the equilibrium Fermi function $f^0(n, k)$ and the Fermi function that is produced by an external electric field/temperature gradient $f(n, k)$. In order to obtain the simplified form of the Boltzmann equation, the constant relaxation time approximation (RTA) is used. Then, Boltzmann transport equation becomes:

$$-\left(\frac{\partial f^0(n, \vec{k})}{\partial \varepsilon(n, \vec{k})}\right) \vec{v}(n, \vec{k}) \left[\frac{\varepsilon(n, \vec{k})}{T} \nabla T + e\vec{E} - \nabla \mu \right] = -\left(\frac{g(n, \vec{k})}{t}\right). \quad (3.9.2)$$

When the right side of the above equation is replaced by the RTA (i.e., $g(n, k) = f(n, k) - f^0(n, k)$), it can be solved for $f(n, k)$. For the calculations, the band structure data $\varepsilon(n, k)$ is needed from which the Boltzmann equation may be calculated, where the group velocity $v(n, k)$ is given as:

$$\vec{v}(n, \vec{k}) = \frac{1}{\hbar} \left(\frac{\partial \varepsilon(n, \vec{k})}{\partial \vec{k}} \right). \quad (3.9.3)$$

As the $f(n, k)$ is now known, using the electrical-current density, the thermoelectric properties can be calculated. On the other hand, the current density is given by the Onsager relations:

$$J = -\frac{16\pi e\sqrt{2m}}{3h^3} \int E^{3/2} \tau(E) \frac{\partial f_0}{\partial E} \left(\frac{E - \mu}{T} \nabla \mu + eE_0 \right) dE. \quad (3.9.4)$$

$$J_Q = -\frac{16\pi\sqrt{2m}}{3h^3} \int E^{3/2} (E - \mu) \tau E \frac{\partial f_0}{\partial E} \left(\frac{E - \mu}{T} \nabla \mu + eE_0 \right) dE. \quad (3.9.5)$$

Evaluating the above equations results in the Onsager relations, given below:

$$\vec{J} = \sigma E_0 - \sigma S \nabla T, \quad (3.9.6)$$

$$\vec{J} = \sigma S T E_0 - \kappa \nabla T, \quad (3.9.7)$$

the terms σ , S , E_0 and ∇T denote the electric conductivity, Seebeck coefficient, external electric field and the temperature gradient, respectively. The κ' symbolizes for the thermal conductivity that is achieved from the electrical conductivity using the Wiedmann-Franz law. Given the above, it is possible to calculate all thermoelectric properties.

$$\sigma = \frac{ne^2\tau(E_f)}{m}. \quad (3.9.8)$$

$$S = -\frac{\pi^2 k_B^2}{3e} \frac{\partial}{\partial E} \ln[E^{3/2}\tau(E)]_{E-E_f}. \quad (3.9.9)$$

$$\kappa = \frac{\pi^2 k_B^2}{3e^2} \sigma T. \quad (3.9.10)$$

3.9.1 Thermoelectric (TE) Properties

Thermoelectric properties are effects that occur in some materials due to the temperature difference between two dissimilar metals, which create an electric potential and vice versa. Seebeck coefficient, Peltier effect and Thomson effect are phenomena that are responsible for thermoelectric properties. In extant literature, a considerable attention has been given to thermoelectric materials due to their useful applications, such as electric generators, thermoelectric coolers, clean energy, photon sensing devices and mechanic free heat pumps [57]. Material selection criteria for thermoelectric are based on dimensionless quantity called Figure of Merit (ZT) [57].

$$ZT = \frac{S^2\sigma}{k_e + k_l} T, \quad (3.9.11)$$

where S represents Seebeck coefficient, σ is the electric conductivity, T is the absolute temperature and k_e, k_l are the thermal conductivities due electrons and lattice, respectively. The above equation clearly shows that, to obtain high ZT , the material should have maximum value of Seebeck coefficient and lower thermal conductivities of electrons and lattice [58] (see Fig. (3.9)). In this work, the transport properties were computed using the BoltzTraP code based on the Boltzmann theory. In the real compounds, the variations in the hole and electron distribution is explained by the Boltzmann transport relations. Using BoltzTraP code, all pertinent parameters (electrical/thermal conductivities, Seebeck coefficient, power factor and Figure of Merit) can be investigated with constant relaxation time. The transport tensors vs. temperature and chemical potential [57, 59, 60, 61] are expressed as:

$$\sigma_{\alpha\beta}(\mu, T) = \frac{1}{\Omega} \int \bar{\sigma}_{\alpha\beta}(\epsilon) \left[\frac{-\partial f_0(T, \epsilon, \mu)}{\partial \epsilon} \right] d\epsilon, \quad (3.9.12)$$

$$S_{\alpha\beta}(\mu, T) = \frac{1}{eT\Omega\sigma_{\alpha\beta}(T, \mu)} \int \sigma_{\alpha\beta}(\epsilon) (\epsilon - \mu) \left[\frac{-\partial f_0(T, \epsilon, \mu)}{\partial \epsilon} \right] d\epsilon, \quad (3.9.13)$$

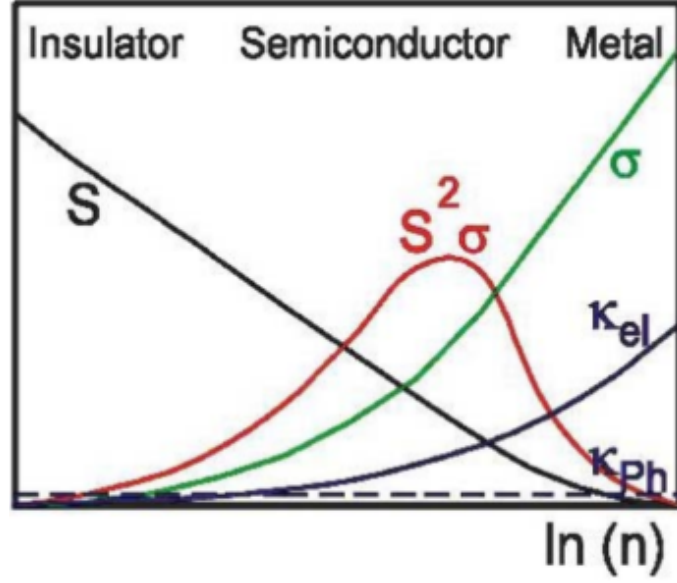


Figure 3.9: Dependence of Seebeck coefficient, electrical conductivity, thermal conductivity and power factor on charge carrier concentration [58].

where α and β denote tensor subscripts while Ω , μ , and f_0 symbolize the volume (unit cell), Fermi level (charge carrier) and Fermi distribution function, respectively. Using the constant relaxation time approximation, the Seebeck coefficient can be

$$S = \pm \frac{1}{eT} [E_F - \int_0^\infty g(E) \tau_e E^2 \frac{df_0(E)}{dE} / \int_0^\infty g(E) \tau_e E^2 \frac{df_0(E)}{dE}], \quad (3.9.14)$$

where the e , E_F , $g(E)$, τ_e are the electron charge, Fermi level, the density of state and relaxation time, respectively. The Fermi level (E_F) and the density of state ($g(E)$) as a function of E can be obtained from the calculated DFT results and the relaxation time τ_e is treated as a constant. Therefore, the Seebeck coefficient as a function of temperature T can be determined using the expression above.

The Seebeck coefficient plays a significant role in determining the performance of the thermoelectric material. Seebeck measurements are frequently used to measure the sign of the dominant charge carriers in a material.

The $\sigma_{\alpha\beta}$ (conductivity distribution), a particularly significant part of σ , is expressed as:

$$\bar{\sigma}_{\alpha\beta} = \frac{e^2}{N} \sum_{i,k} \tau \cdot v_\alpha(i, k) \cdot v_\beta(i, k) \cdot \frac{\delta(\epsilon - \epsilon_{i,k})}{d\epsilon}. \quad (3.9.15)$$

In the stated expression, k , i and N , are the wave vector, band indices, and number of k points, respectively, whereas $v_\alpha/v_\beta(i, k)$ denotes the α/β components of the group velocity $v(i, k)$ of charge carrier. The $v(i, k)$ (group velocity) is expressed as:

$$v(i, k) = \frac{1}{\hbar} \frac{\partial \epsilon(i, k)}{\partial k_\alpha}. \quad (3.9.16)$$

The velocity featuring in the expression above can be evaluated using the energy band structures, also known as the band crossing [62].

The electrical conductivity is comparatively larger for metals, in the order of $10^6(\Omega cm)^{-1}$. In semiconductors, for conduction to occur, the carriers must be thermally excited across a gap.

$$\sigma \approx \sigma_0 \exp\left[\frac{+E_G}{K_\beta T}\right]. \quad (3.9.17)$$

Using the BoltzTraP code, the electrons mobility is considered as semi-classical. The thermal conductivity tensor (dependent on temperature and chemical potential) can be expressed as:

$$\kappa_{\alpha\beta}(\mu, T) = \frac{1}{eT\Omega} \int \sigma_{\alpha\beta}(\epsilon)(\epsilon - \mu)^2 \exp\left[\frac{-\partial f_0(T, \epsilon, \mu)}{\partial \epsilon}\right] d\epsilon. \quad (3.9.18)$$

On the other hand, the electronic thermal conductivity is given by:

$$\kappa_e = \kappa^0 - S^2 \sigma T. \quad (3.9.19)$$

Using these expressions, the power factor ($S^2 \sigma$) and Figure of Merit ($ZT = \frac{S^2 \sigma}{k_e + k_l} T$) can be computed, thus revealing valuable information regarding the material efficiency.

Chapter 4

Conclusion

Combined study of the electronic structure, optical and thermal properties were performed by first principle methods. The calculated electronic band structure results shows P1 and P5 shows indirect while the P2 and P5 shows the direct band gap. Whereas the P3 shows the metallic nature. Our investigated electronic band structure results show good agreement with previous theoretical and experimental results. From the density of states we found covalent nature due to strong hybridization among the atoms of the P1 P2 and P5. The frequency dependent dielectric function was calculated to study optical properties. The calculated results showed inter/intra-band absorption in the low frequency region within the band gap. As we found that the P1 and P5 are wide (direct) band gap material. Our results for the dielectric function show strong and direct absorption at the sharp peak. We found that the P1 and P2 has a maximum reflectivity in the visible and UV regions of electro-magnetic spectrum leading to consider it for potential application as photo-voltaic material. In addition we also focused on the thermal properties for the P1 and P2. The effects of substitution for these compounds on the electrical and thermal transport were emphasized. This substations shows incorporate a significant increased in the thermoelectric figure of merit that mainly resulted from the reduction of thermal conductivity. Therefore, substitutions have been a feasible and common way to enhance thermoelectric properties in these quaternary chalcogenides compounds, especially for P1.

The reported calculations in this thesis provide new structural, electronic, optical and thermoelectric results for new materials based on sulfur (S), selenium (Se), tellurium (Te). Hence, this study forms part of a large theoretical effort to explore the properties of these compounds, so it is our ambition that these calculations will inspire further experimental research on these compounds.

Chapter 5

Bibliography

Bibliography

- [1] Whittingham, M. S. *Prog. Solid State Chem.*, 12, (1978) 60.
- [2] Fritz, I. J.; Isaacs, T. J.; Gottlieb, M.; Morosin, B. *Solid State Commun.*, 27, (1978) 535.
- [3] Rabenau, A. *Angew. Chem.*, 24, (1985) 1026.
- [4] DuBois, M. R. *Chem. Rev.*, 89, (1989) 1.
- [5] Schultz, L. D.; Koehler, W. H. *Inorg. Chem.* 1987, 26, 1989
- [6] Kadel K, Kumari L, Li W Z, Huang J Y and Provencio P P 2011 *Nanoscale Res. Lett.* 6 57
- [7] Simon, A. *Angew. Chem.*, 20, (1981) 1.
- [8] *ChemInform.*, (2007) 38.
- [9] P. Klchambare, M. Sharon, Y. Seki, T. Hagino, S. Nagata, *Solid State Ionics* 101- 103 (1997) 125
- [10] S. Azam, S.A. Khan, and S. Goumri-Said, *Mater. Res. Bull.* 430 70, 847 (2015).
- [11] S. Azam, S.A. Khan, and S. Goumri-Said, *Mater. Sci.* 432 *Semicond. Process.* 39, 606 (2015).
- [12] Zhang Q, Cao F, Liu W, Lukas K, Yu B, Chen S, Opeil C, Broido D, Chen G and Ren Z 2012 *J. Am. Chem. Soc.* 134 100318
- [13] Mrotzek A, Chung D Y, Hogan T and Kanatzidis M G 2000 *J. Mater. Chem.* 10 1667
- [14] Khan W and Goumri-Said S 2015 *RSC Adv.* 5 945561
- [15] Sankar C R, Assoud A and Kleinke H 2013 *Inorg. Chem.* 52 1386974
- [16] W. S. Sheldrick and M. Wachhold, *Coord. Chem. Rev.*, 1998, 176, 211.

- [17] M. G. Kanatzidis, *Curr. Opin. Solid State Mater. Sci.*, 1997, 2, 139.
- [18] M. G. Kanatzidis and B. K. Das, *Comments Inorg. Chem.*, 1999, 21, 29.
- [19] W. S. Sheldrick and M. Wachhold, *Angew. Chem., Int. Ed. Engl.*, 1997, 36, 206.
- [20] G. Krauter and K. Dehnicke, *Chem.-Ztg.*, 1990, 114, 79.
- [21] K.-W. Kim and M. G. Kanatzidis, *J. Am. Chem. Soc.*, 1998, 120, 81248135.
- [22] M. Wachhold and M. G. Kanatzidis, *J. Am. Chem. Soc.*, 1999, 121, 41894195.
- [23] K.-W. Kim and M. G. Kanatzidis, *J. Am. Chem. Soc.*, 1992, 114, 4878.
- [24] J. Li, Z. Chen, R.-J. Wang and J. Y. J. Lu, *Solid State Chem.*, 1998, 140, 149.
- [25] X. Chen, K. J. Dilks, X. Huang and J. Li, *Inorg. Chem.*, 2003, 42, 37233727.
- [26] N. Oh George, E.S. Choi, J.A. Ibers, *Inorg. Chem.* 51 (2012) 4224.
- [27] N. Oh George, E.S. Choi, J. Lu, Lukasz A. Koscielski, M.D. Ward, D.E. Ellis, J.A. Iber, *Inorg. Chem.* 51 (2012) 8873.
- [28] D. Mei, Z. Lin, L. Bai, J. Yao, P. Fu, Y. Wu, *J. Solid. Stat. Chem.* 183 (2010) 16401644.
- [29] G. Zhang, B. Zhang, H. Chen, X. Zhang, C. Zheng, J. Lin, F. Huang, *J. Alloys Comp.* 591 (2014) 610.
- [30] W. Yin, K. Feng, L. Kang, B. Kang, J. Deng, Z. Lin, J. Yao, Y. Wu, *J. Alloys Comp.* 617 (2014) 287291.
- [31] A. Chatterjee, K. Biswas, *Angew. Chem. Int. Ed.* 54 (2015) 5623.
- [32] S.N. Guin, J. Pan, A. Bhowmik, D. Sanyal, U.V. Waghmare, K. Biswas, *J. Am. Chem. Soc.* 136 (2014) 12712.
- [33] W. Liu, J.-S. Lee, D.V. Talapin, *J. Am. Chem. Soc.* 135 (2013) 1349.
- [34] W.-W. Xiong, J. Miao, K. Ye, Y. Wang, B. Liu, Q. Zhang, *Angew. Chem. Int. Ed.* 54 (2015) 546.
- [35] Vaughan, D. J. *Encyclopedia of Geology, MINERALS* Elsevier: Selley RC, (2005).
- [36] Bouroushian, M. *Electrochemistry of Metal Chalcogenide*; Springer-Verlag Berlin Heidelberg, (2010).

- [37] Liao, J. H.; Marking, G. M.; Hsu, K. F.; Matsushita, Y.; Ewbank, M. D.; Borwick, R.; Cunningham, P.; Rosker, M. J.; Kanatzidis, M. G. J. *Am. Chem. Soc.*, 125, (2003) 9484.
- [38] Sikander Azam, Saleem Ayaz Khan, Souraya Goumri-Said, *Journal of Solid State Chemistry* 229 (2015) 260265
- [39] Chung, I.; Kanatzidis, M. G. *Chem. Mater.*, 26, (2013) 849.
- [40] Hohenberg P and Kohn W 1964 *Phys. Rev. B* 136 864.
- [41] W. KOHN, L.J. S HAM. Self-consistent Equations Including Exchange and Correlation Effects. *Phys. Rev.* 140, A1133A1138,(1965).
- [42] S. Cottenier, *Density Functional Theory and the family of (L)APW-methods: a step-by-step introduction* (Instituut voor Kern- en Stralings-fysica, K.U.Leuven, Belgium), 2002, ISBN 90-807215-1-4 (to be found at <http://www.wien2k.at/reguser/textbooks>).
- [43] F. Tran and P. Blaha, *Phys. Rev. Lett.* 102, 226401 (2009)
- [44] A. D. Becke and E. R. Johnson, *J. Chem. Phys.* 124, 221101 (2006) bibitemP. A. M. Dirac1930 P. A. M. Dirac, *Proc. Cambridge Philos. Soc.* 26 376,(1930)
- [45] Stefan Blugel and Gustav Bihlmayer, *Computational Nanoscience*, John von Neumann Institute for Computing, Julich, NIC Series, Vol. 31, ISBN 3-00-017350-1, pp. 85-129, 2006.
- [46] N.W. Achcroft et N.D. Mermin, *Solid State Physics*, editions internationals Holt-Saunders,(Japon, 1981).
- [47] J. C. Slater, *Wave Functions in a Periodic Potential*, *Phys. Rev.* 51, 846, (1937).
- [48] K. Schwarz, P. Blaha, G.K.H. Madsen, *Computer Physics Communications* 147 (2002) 7176
- [49] O. K. Andersen, *Linear methods in band theory*, *Phys. Rev. B* 12, 3060, (1975).
- [50] D. D. Koelling and G. O. Arbman, *Use of energy derivative of the radial solution in an augmented plane wave method: application to copper*, *J. Phys. F (Metal Phys.)* 5,2041, (1975).
- [51] Cottenier, S. *Density Functional Theory and the family of (L)APW-methods: a step-by-step introduction* isbn: 90-807215-1-4 (Instituut voor Kern- en Stralingsfysica, K.U.Leuven, Belgium, 2002).

- [52] P. Blaha, K. Schwarz, and J. Luitz, WIEN2k, An Augmented Plane Wave + Local Orbitals Program for Calculating Crystal Properties, (Karlheinz Schwarz, Techn. Univ. Wien, Austria),2001. ISBN 3-9501031-1-2
- [53] G. Tarrach, D. Brgler, T. Schaub, R. Wiesendanger, and H. Gntherodt, Surf. Sci. 285, (1993) 1.
- [54] C. Martos, J. Dufour, and A. Ruiz, Int. J. Hydrogen Energy 34, (2009) 4475.
- [55] P. Blaha, K. Schwarz, and J. Luitz, WIEN2k, An Augmented Plane Wave + Local Orbitals Program for Calculating Crystal Properties, (Karlheinz Schwarz, Techn. Univ. Wien, Austria), (2001). ISBN 3-9501031-1-2
- [56] OPTICAL PROPERTIES OF SOLIDS Prof. Mark Fox
- [57] Chakraborty B., Pickett W. E., and Allen P. B., Phys. Rev. B 14, 3227 (1976).
- [58] Mayasree Oottil, M.Sc thesis (2010).
- [59] Bhagavantam, Crystal symmetry and physical properties, Academic press, New York, (1966).
- [60] Landau L., Liftshitz E., and Pitaevskii L., Electrodynamics of continuous media, Pergamon press, Oxford, 1960.
- [61] GUO Kai, CAO Qigao, ZHAO Jingtai, JOURNAL OF RARE EARTHS, 31 (2013) 1029
- [62] Sikander Azam, Saleem Ayaz Khan, Fahad Ali Shah, Saleh Muhammad, Haleem Ud Din, R. Khenata, Intermetallics 55 (2014) 184-194

Chapter 6

Reprints of selected publications

- P1 Sikander Azam, Saleem Ayaz Khan, Jan Minar, Wilayat Khan, Haleem Ud Din, R Khenata, G Murtaza, S Bin-Omran and Souraya Goumri-Said, *Semi-cond. Sci. Technol.* 00 (2015) 000000 (9pp)
- P2 Sikander Azam and A. H. Reshak, *RSC Adv.*, 2014, 4, 20102 - 20113
- P3 Haleem Ud Din, Sikander Azam, Saleem Ayaz Khan, R. Khenata, *Journal of Alloys and Compounds* 615 (2014) 507513
- P4 Sikander Azam, Saleem Ayaz Khan, Souraya Goumri-Said, *Journal of Solid State Chemistry* 229 (2015) 260265
- P5 Sikander Azam, Saleem Ayaz Khan, Wilayat Khan, Saleh Muhammad, Haleem Udin, G. Murtaza, R. Khenata, Fahad Ali Shah, Jan Minar, W.K. Ahmed *Journal of Alloys and Compounds* 644 (2015) 9196

[Home](#) [Search](#) [Collections](#) [Journals](#) [About](#) [Contact us](#) [My IOPscience](#)

Coulomb interaction and spin-orbit coupling calculations of thermoelectric properties of the quaternary chalcogenides Tl_2PbXY_4 (X = Zr, Hf and Y = S, Se)

This content has been downloaded from IOPscience. Please scroll down to see the full text.

2015 Semicond. Sci. Technol. 30 105018

(<http://iopscience.iop.org/0268-1242/30/10/105018>)

View [the table of contents for this issue](#), or go to the [journal homepage](#) for more

Download details:

IP Address: 137.149.200.5

This content was downloaded on 02/09/2015 at 07:28

Please note that [terms and conditions apply](#).

Coulomb interaction and spin-orbit coupling calculations of thermoelectric properties of the quaternary chalcogenides Tl_2PbXY_4 ($X = Zr, Hf$ and $Y = S, Se$)

Sikander Azam¹, Saleem Ayaz Khan¹, Jan Minar¹, Wilayat Khan¹, Haleem Ud Din², R Khenata³, G Murtaza⁴, S Bin-Omran⁵ and Souraya Goumri-Said^{6,7}

¹New Technologies—Research Center, University of West Bohemia, Univerzitni 8, 306 14 Pilsen, Czech Republic

²Materials Modeling Lab, Department of Physics, Hazara University, Mansehra, Pakistan

³Laboratoire de Physique Quantique et de Modélisation Mathématique (LPQ3M), Département de Technologie, Université de Mascara, Mascara 29000, Algeria

⁴Materials Modeling Lab, Department of Physics, Islamia College Peshawar, Pakistan

⁵Department of Physics and Astronomy, College of Science, King Saud University, PO Box 2455, Riyadh 11451, Saudi Arabia

⁶School of Chemistry and Biochemistry and Center for Organic Photonics and Electronics, Georgia Institute of Technology, Atlanta, Georgia 30332-0400, USA

⁷School of Science, Alfaisal University, Riyadh 11533, Saudi Arabia

E-mail: Souraya.Goumri-Said@chemistry.gatech.edu

Received 2 May 2015, revised 14 July 2015

Accepted for publication 27 July 2015

Published 1 September 2015



CrossMark

Abstract

The increase in energy demands is leading to growing interest in new thermoelectric inorganic materials, such as the chalcogenides. The recently synthesized quaternary chalcogenide, Tl_2PbXY_4 ($X = Zr, Hf$ and $Y = S, Se$), compounds were investigated using the full potential linear augmented plane wave method based on density functional theory. We used the generalized gradient approximation plus the optimized effective Hubbard parameter U to treat the exchange correlation. The existence of heavy metals (Tl, Pb and Hf) required the application of relativistic spin-orbit coupling via a second variational procedure. Tl_2PbHfS_4 , $Tl_2PbHfSe_4$, Tl_2PbZrS_4 and $Tl_2PbZrSe_4$ compounds were found to be semiconductors with indirect band gaps of 0.911, 0.659, 0.983 and 0.529 eV, respectively. The types of carriers and electrical transport properties of Tl_2PbXY_4 ($X = Zr, Hf$ and $Y = S, Se$) are attributed to the $Tl-d$ and $S/Se-s$ electronic states near the Fermi level. Optical properties were investigated via the calculation of dielectric function and reflectivity. Using Boltzmann theory, we compared the thermoelectric properties and we found that Tl_2PbHfS_4 could be a good candidate for thermoelectric devices.

Keywords: chalcogenides, thermoelectric, semiconductors, Seebeck coefficient, optical properties, DFT, inorganic materials

(Some figures may appear in colour only in the online journal)

1. Introduction

Recently, inorganic compound semiconductors have been considered of great interest because of the increasing attention on energy conversion and renewable energy sources. One important application of these compounds is thermoelectric energy conversion [1–3]. Materials with low thermal conductivity, a high Seebeck coefficient and electrical conductivity, and a figure of merit (ZT) equal to one are good candidates for thermoelectric devices [4]. One of the most challenging tasks for solid state physicists and chemists is to increase the figure of merit, ZT of the synthesized thermoelectric materials. Transition metal chalcogenides are considered as interesting candidates for thermoelectric materials where the anion–anion bonding in chalcogenides can enhance the molecular anion and provide higher covalency. Some thermoelectrics based on selenides that have been reported in the recent literature are: Bi_2Se_3 materials [5], doped PbSe [6], quaternary tin selenide $\text{K}_{1-x}\text{Sn}_{5-x}\text{Bi}_{11+x}\text{Se}_{22}$ [7] and CsCdInQ_3 ($Q = \text{Se}, \text{Te}$) [8].

The TI-based quaternary chalcogenides incorporating a group IV-B metal ($X = \text{Zr}, \text{Hf}$) are attractive for thermoelectric devices. Thallium (TI), as a heavy metal, reduces the thermal conductivity and creates complex coordination due to the presence of a lone electron pair and is very useful in thermoelectrics. Among complex inorganic compounds, a new class of quaternary compounds with the general formula TI_2PbXY_4 ($X = \text{Zr}, \text{Hf}$ and $Y = \text{S}, \text{Se}$) has been investigated. These compounds crystallize in the monoclinic crystal system with space group $C2/c$ and have indirect band gaps below 1 eV and optical gaps of 1.2–1.6 eV. The electrical transport properties of TI_2PbXY_4 indicate that this material exhibits a semiconducting nature [9]. A large positive Seebeck coefficient from $S = +190 \text{ V K}^{-1}$ at room temperature to $S = +420 \text{ V K}^{-1}$ at 520 K has been observed for $\text{TI}_2\text{PbHfSe}_4$ [9]. The presence of thallium might necessitate considerable caution in manipulating $\text{TI}_2\text{PbHfSe}_4$, due to the toxicity of TI.

In this paper, we determined the electronic, optical and thermoelectric properties of the TI-based quaternary chalcogenides TI_2PbXY_4 ($X = \text{Zr}, \text{Hf}$ and $Y = \text{S}, \text{Se}$) using the full potential linear augmented plane wave (FP-LAPW) method within density functional theory (DFT) [10, 11]. Thermoelectric properties, such as the thermal conductivity, Seebeck coefficient, electrical conductivity and figure of merit (ZT), are calculated from 300 K to 800 K using the BoltzTraP code [12]. This article is organized into four sections. In section 1, we have given a brief introduction to the topic and the main aims. The computational methodology is presented in section 2. The results and discussion of the calculations are described in detail in section 3. Finally, a summary completes the current work in section 4.

2. Computational methodology

The TI-based quaternary chalcogenides TI_2PbXY_4 ($X = \text{Zr}, \text{Hf}$ and $Y = \text{S}, \text{Se}$) have been investigated as new types of structures in the monoclinic crystal system with space group $C2/c$ ($Z = 4$) (as shown in figure 1). The lattice

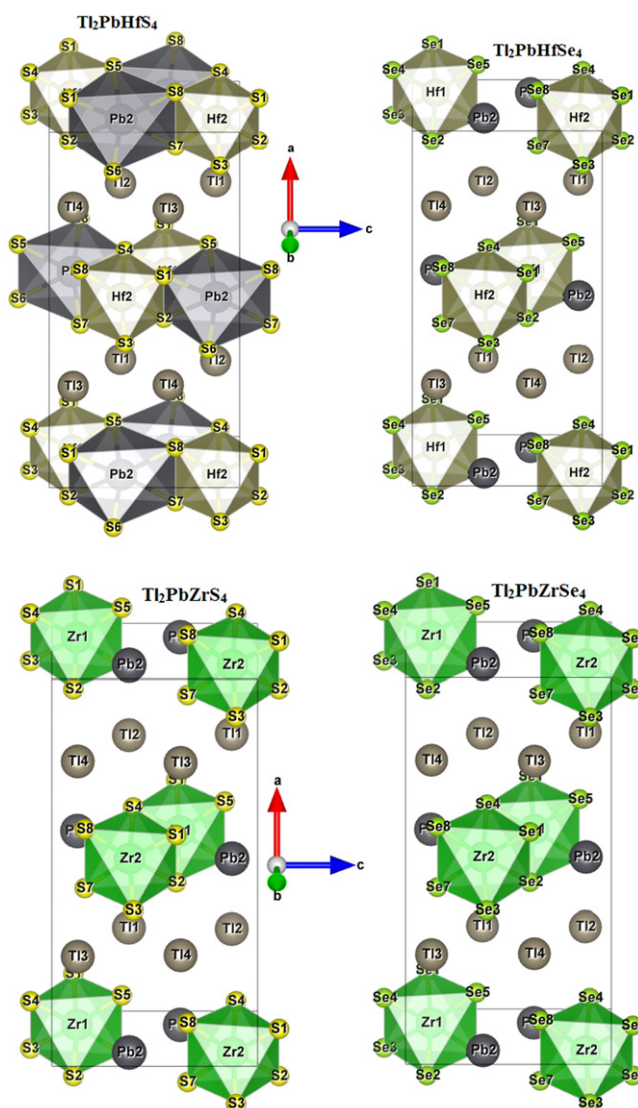


Figure 1. Unit cell structure of the considered chalcogenides TI_2PbXY_4 ($X = \text{Zr}, \text{Hf}$ and $Y = \text{S}, \text{Se}$).

parameters, $a = 15.455 \text{ \AA}$, $b = 8.214 \text{ \AA}$ and $c = 6.751 \text{ \AA}$ (for $\text{TI}_2\text{PbZrS}_4$), $a = 15.906 \text{ \AA}$, $b = 8.472 \text{ \AA}$ and $c = 7.016 \text{ \AA}$ (for $\text{TI}_2\text{PbZrSe}_4$), $a = 15.470 \text{ \AA}$, $b = 8.226 \text{ \AA}$ and $c = 6.7103 \text{ \AA}$ (for $\text{TI}_2\text{PbHfS}_4$), and $a = 15.9480 \text{ \AA}$, $b = 8.4720 \text{ \AA}$ and $c = 6.9733 \text{ \AA}$ (for $\text{TI}_2\text{PbHfSe}_4$) were obtained from [9]. We performed electronic, optical and thermoelectric calculations of the TI_2PbXY_4 compounds.

In this study, a very efficient and successful approach, the FP-LAPW method within the framework of DFT as implemented in the WIEN2k package [13], was used to solve the Kohn–Sham equations [10]. The exchange correlation was treated within the generalized gradient approximation plus the optimized effective Hubbard parameter U (GGA + U) [14–18]. Spin–orbit coupling (SOC) was also taken into consideration using the variational approach [13]. We used a mesh of 2000 k -points in the irreducible Brillouin zone and the muffin-tin radius (R_{MT}) for TI, Pb, Zr, Hf, S and Se. The wave function inside the sphere was expanded in spherical harmonics up to $l_{\text{max}} = 10.0$, and the charge density was

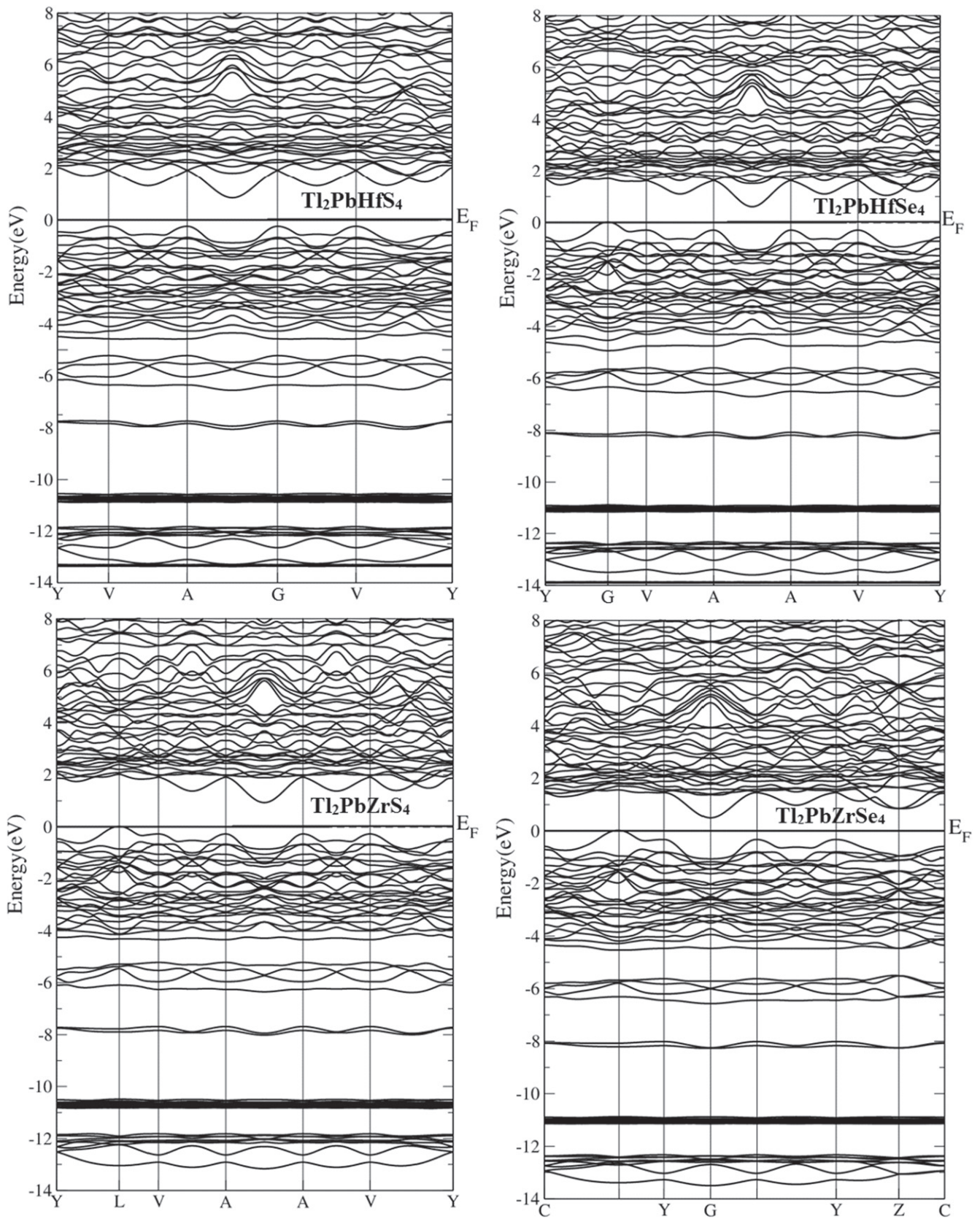


Figure 2. Calculated band structure of Tl_2PbXY_4 ($X = \text{Zr, Hf}$ and $Y = \text{S, Se}$).

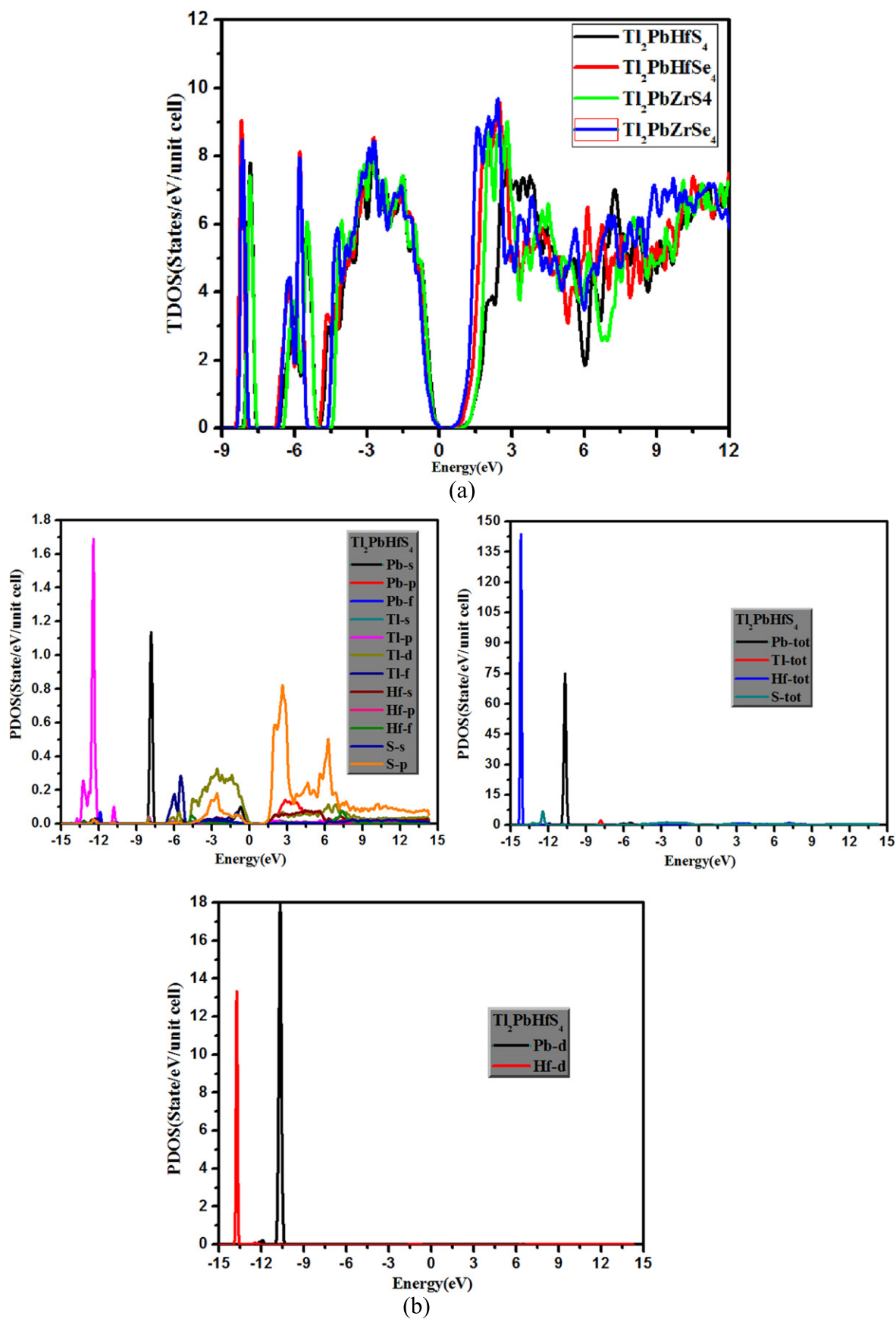


Figure 3. Calculated total and partial DOS (states/eV unit cell).

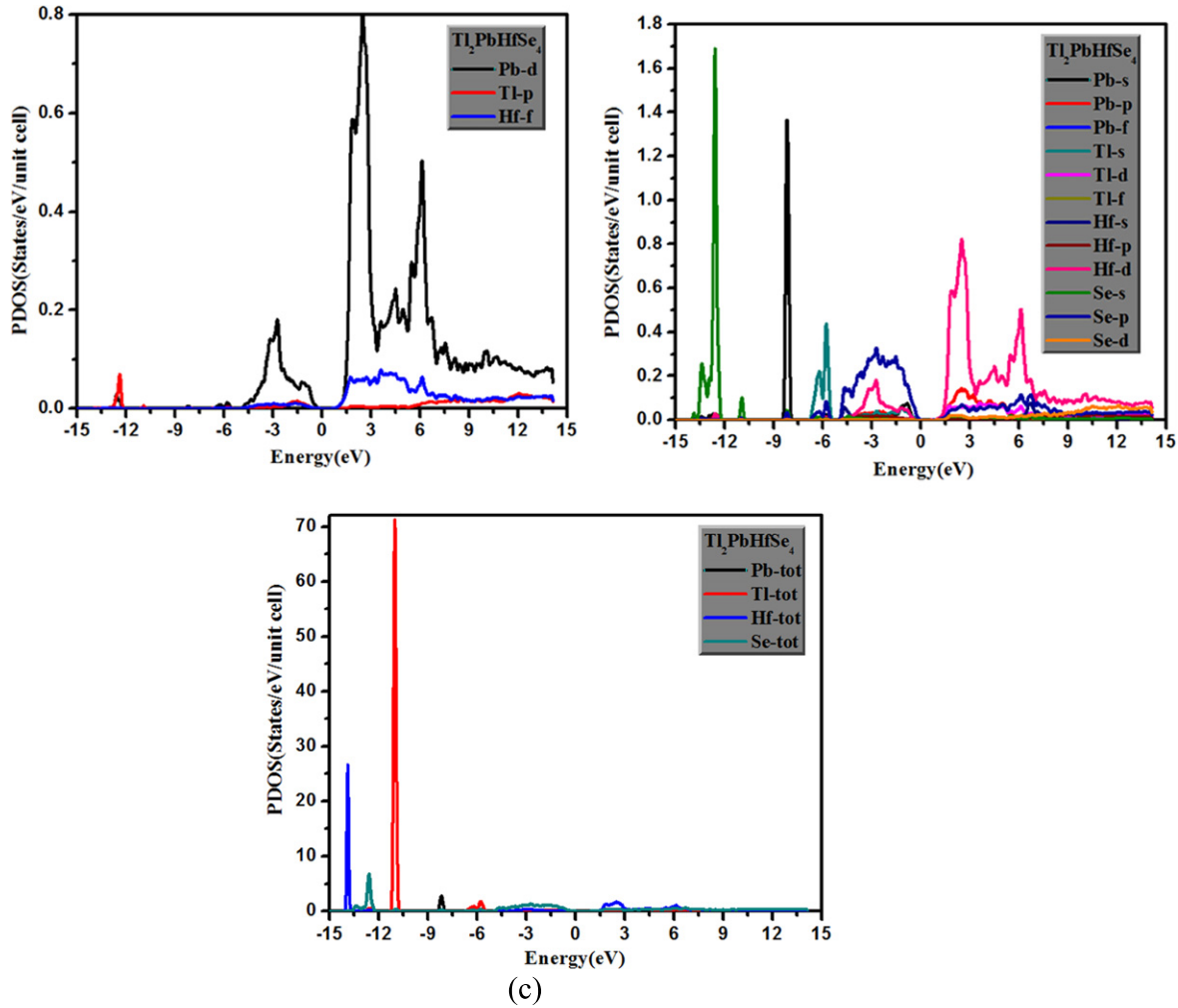


Figure 3. (Continued.)

Fourier expanded to $G_{\max} = 12.0$. The value of $R_{\text{MT}} \times K_{\max}$ was taken as 7.0. The self-consistent calculations were considered to be converged when the total energy was 10^{-4} Ry.

Using Boltzmann transport theory and the rigid band approach implemented in the BoltzTraP code [12] we calculated the transport coefficient under constant scattering time of the crystalline materials [12]. In fact, this package is efficient in elucidating the electronic structure and transport coefficients of the considered compounds. In the present approximation, we ignored the temperature dependence on the E - K curve (band structure). Combining DFT outputs and the BoltzTraP code, we were able to determine the Seebeck coefficient (S), along with the electrical conductivity (σ), thermal conductivity (k_{ele}) and power factor ($S^2\sigma$), as function of constant relaxation time (s).

3. Results and discussion

3.1. Electronic properties

The band structures of the investigated compounds are shown in figure 2, illustrating the semiconducting nature of these

compounds. We observed a very negligible interaction of the Pb-d/f states in the projected densities of states (PDOS) figure and a small contribution of Tl-p states, whereas a remarkable contribution of the f-states of Hf is observed. Figure 2 shows the energy band structures of the $\text{Tl}_2\text{PbHfSe}_4$, $\text{Tl}_2\text{PbHfSe}_4$, $\text{Tl}_2\text{PbZrS}_4$ and $\text{Tl}_2\text{PbZrSe}_4$ compounds, which were calculated using the FP-LAPW method. In the band structure, the valence band (VB) region appears from -13.82 to 0 eV, and the conduction band region appears from 0.911 , 0.659 , 0.983 and 0.529 eV onwards for the $\text{Tl}_2\text{PbHfSe}_4$, $\text{Tl}_2\text{PbHfSe}_4$, $\text{Tl}_2\text{PbZrS}_4$ and $\text{Tl}_2\text{PbZrSe}_4$ compounds, respectively. We should emphasize that our calculated band gap using GGA + U + SOC produces better results than previous calculations [10]. The substantial dispersion of the bands corresponds to delocalized electrons in real space. Near the Fermi level, the maximum of the VB for $\text{Tl}_2\text{PbHfSe}_4$, $\text{Tl}_2\text{PbHfSe}_4$, $\text{Tl}_2\text{PbZrS}_4$ and $\text{Tl}_2\text{PbZrSe}_4$ occurs at the A, Γ , L and L points, respectively. While the conduction band minimum occurs at the G point for $\text{Tl}_2\text{PbZrSe}_4$ and along the A- Γ , A-A and A-A directions for $\text{Tl}_2\text{PbHfSe}_4$, $\text{Tl}_2\text{PbHfSe}_4$, and $\text{Tl}_2\text{PbZrS}_4$, respectively, resulting in indirect band gap materials.

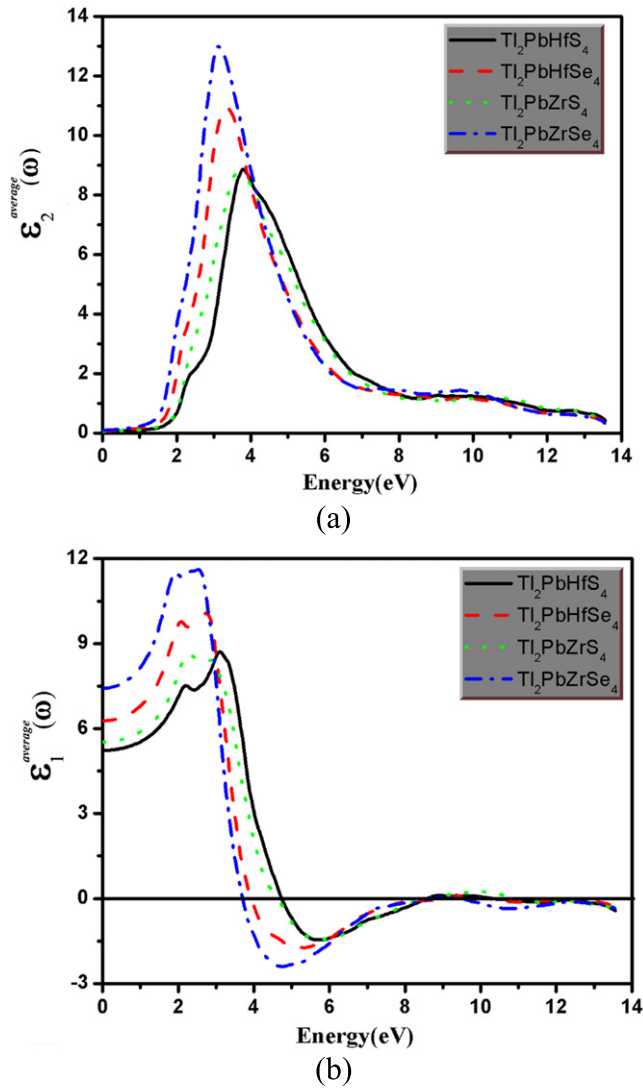


Figure 4. Calculated imaginary $\varepsilon_2(\omega)$ (a) and real part $\varepsilon_1(\omega)$ (b) of the dielectric tensor.

To further elucidate the nature of the electronic band structure and contribution of each atom in the structures, we calculated the total and atomic site PDOS for these compounds. Figure 3 shows the calculated DOS of only the $\text{Tl}_2\text{PbHfS}_4$ and $\text{Tl}_2\text{PbHfSe}_4$ compounds as an example since the band profiles are quite similar for the remaining compounds with very small differences in the details. The investigated DOS can be divided into various group structures separated by energy gaps. Based on the PDOS, the angular momentum is the origin of diverse bands. The lowest energy group from -15.0 to 12.0 eV has arisen mainly from the Tl-p and Hf/Zr-d states. The second group from -11.0 to -7.5 eV has mainly arisen from the Pb-s/d states. The structure between -7.0 eV and the Fermi level is due to the contribution of the Pb-f, Tl-d and S/Se-p states. The structure above E_f is mainly composed of the S/Se-p, Pb-p, Hf/Zr-s/f and Tl-d states. From the partial DOS, one can see that a strong hybridization exists between S/Se-p and Tl-d in the VB; in the conduction, hybridization also exists between Hf/Zr-s and Tl-d in the conduction bands.

3.2. Optical properties

Knowledge of the complex dielectric tensor components allows the calculation of various optical constants, such as the reflectivity $R^{\text{average}}(\omega)$, the absorption coefficient $\alpha^{\text{average}}(\omega)$ and the energy-loss function $L^{\text{average}}(\omega)$. All the investigated compounds exhibit monoclinic symmetry, which has five nonzero components of the dielectric tensor. However, as we are discussing the Tl-based quaternary chalcogenide Tl_2PbXY_4 ($X = \text{Zr, Hf}$ and $Y = \text{S, Se}$) compounds, there are three major components; therefore, we will discuss the average of the three ($\varepsilon^{\text{average}}(\omega) = (\varepsilon^{\text{zz}}(\omega) + \varepsilon^{\text{yy}}(\omega) + \varepsilon^{\text{xx}}(\omega))/3$) components for all the compounds. The calculated average imaginary part $\varepsilon_2^{\text{average}}(\omega)$ is shown in figure 4(a). As observed in the imaginary spectra, the investigated compounds exhibit approximately the same behavior and the anisotropy only exists at the critical point. The height of the peaks for all the compounds is located between 1.0 and 8.0 eV. The maximum peaks for the chalcogenide Tl_2PbXY_4 compounds are situated between 3.0 and 4.0 eV. These peaks, which emerge in figure 4, are related to the energy transition between orbital numbers (i.e. $\varepsilon_2(\omega)$ is related to the DOS behavior). In contrast to figure 5, it is apparent that the peaks are mostly located due to the transitions from Y-p VBs to Pb-p conduction bands. Far from the main peaks, the next peaks frequently arise from direct transitions between X-s and Tl-p orbitals. Below 8.0 eV, the imaginary spectra decrease incredibly rapidly with photon energy. The consequences for the scattered part of the dielectric function, $\varepsilon_1^{\text{average}}(\omega)$, are observed in figure 4(b).

At higher frequencies, the zero crossing of $\varepsilon_1^{\text{average}}(\omega)$ is related to the position of the screened plasma frequency, as reported in table 1, for all the chalcogenides. The static dielectric constant $\varepsilon_1(0)$ is specified by the small energy edge of $\varepsilon_1(\omega)$. It is necessary to highlight here that we do not include phonon assistance in the dielectric screening, and $\varepsilon_1(0)$ refers to the static optical dielectric constant. The attained optical dielectric constants following the GGA + U + SOC formalism alongside the crystal axes are given in table 1 for the investigated compounds.

Using the estimated dispersions of the imaginary and real components of the frequency-dependent dielectric function, one can further evaluate the optical properties including the refractive index $n^{\text{average}}(\omega)$, absorption coefficient $I^{\text{average}}(\omega)$, reflectivity $R^{\text{average}}(\omega)$ and energy-loss function $L^{\text{average}}(\omega)$. These results are presented in figures 5(a)–(d). The absorption bands in the explored chalcogenides are due to the inter-ion transitions observed in figure 5(a). Our calculated absorption spectra show close agreement with previous experimental work and similar chalcogenides [8, 9]. We observe that all the compounds exhibit an interesting powerful optical absorptions at higher energies. The absorption coefficients of these crests are large, where the peaks represent the optical transitions due to excitons. In the vicinity of the absorption peaks, the absorption coefficients are large and indicate an allowed optical transition, almost certainly due to an exciton level. The intended outcome is that all of the absorption spectra of the compounds exhibit numerous absorption peaks in the fundamental absorption region. In addition, we calculated the electron

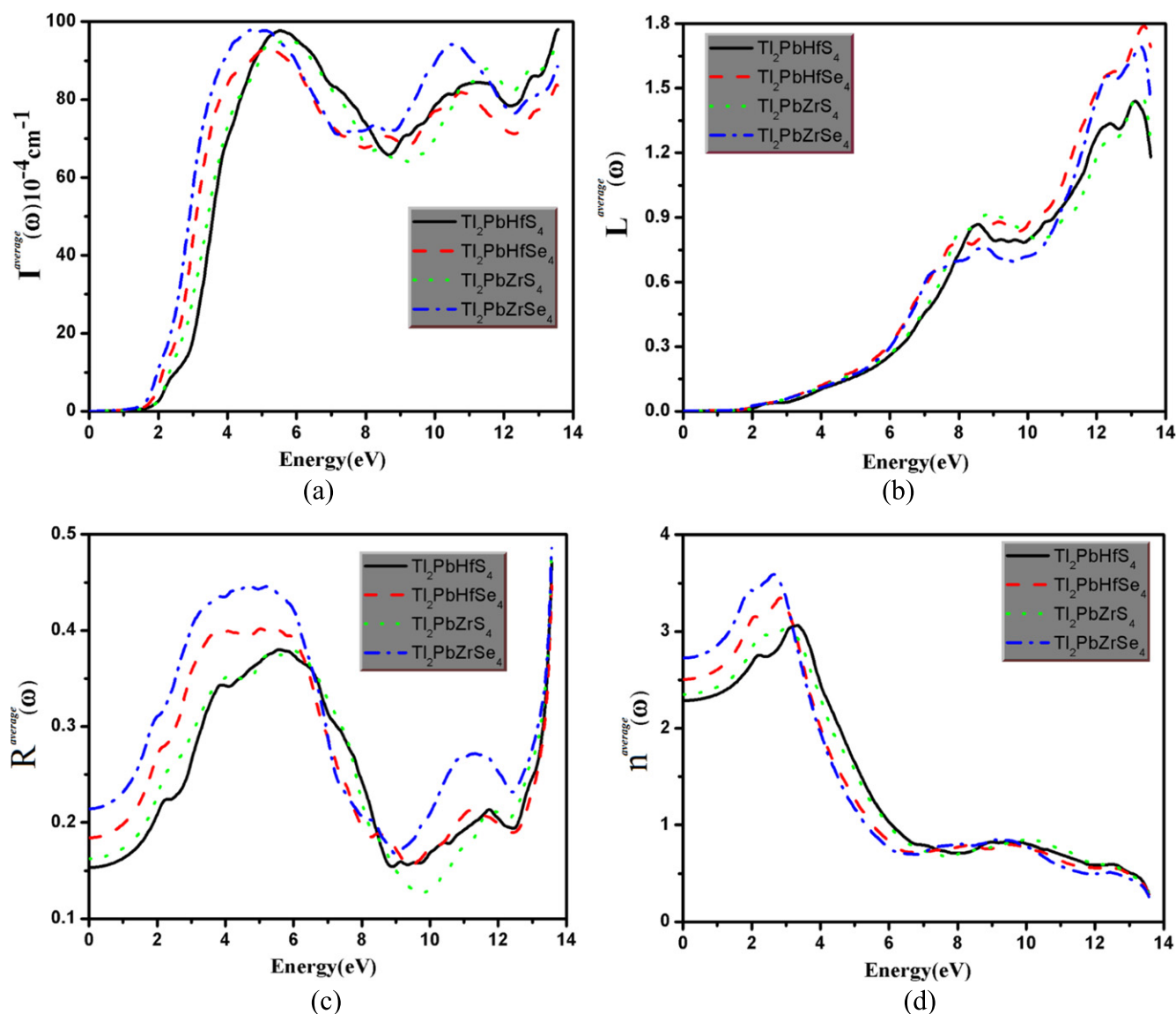


Figure 5. Calculated absorption coefficient $I(\omega)$ (a), energy-loss spectrum $L(\omega)$ (b), reflectivity $R(\omega)$ (c) and refractive index $n(\omega)$ (d).

Table 1. Calculated plasma frequency ω_p and dielectric constant $\epsilon_1(0)$ of the compounds.

Compound	ω_p (eV)	$\epsilon_1(0)$
Tl_2PbHfS_4	4.52	5.22
$Tl_2PbHfSe_4$	3.93	6.27
Tl_2PbZrS_4	4.58	5.52
$Tl_2PbZrSe_4$	3.60	7.42

energy-loss function that describes the interaction responsible for the release of energy by a fast-moving electron traveling in these materials. The interactions may encompass phonon excitation, inter-band and intra-band transitions, plasmon excitations and inner-shell ionizations. The energy loss is generally large at the plasma frequencies. The energy-loss spectra are presented in figure 5(b) for the investigated chalcogenides. The peaks at different energy ranges correspond to electrical device excitations of different orbitals. The greatest

peaks in the energy-loss function are associated with plasma oscillations. Furthermore, figure 5(c) displays the calculated reflectivity spectra. These compounds exhibit medium reflectivity, 45%, in the visible and ultraviolet regions. Figure 5(d) displays the variation of the refractive index as a function of incident photon energy. We note that in the low energy range, the material has a high refractive index, which decreases at high powers.

3.3. Thermoelectric properties

Recently, thermoelectric materials have attracted attention due to their important role in electricity generation from heat, sustainable energy solutions and their widespread use as solid-state Peltier coolers. Thermoelectric ability can be characterized by the dimensionless figure of merit (ZT), which is defined as [1–5, 19, 20]: $ZT = S^2 T \sigma / (\kappa_e + \kappa_l)$. Here, S , T , σ , κ_e and κ_l represent the Seebeck coefficient, absolute

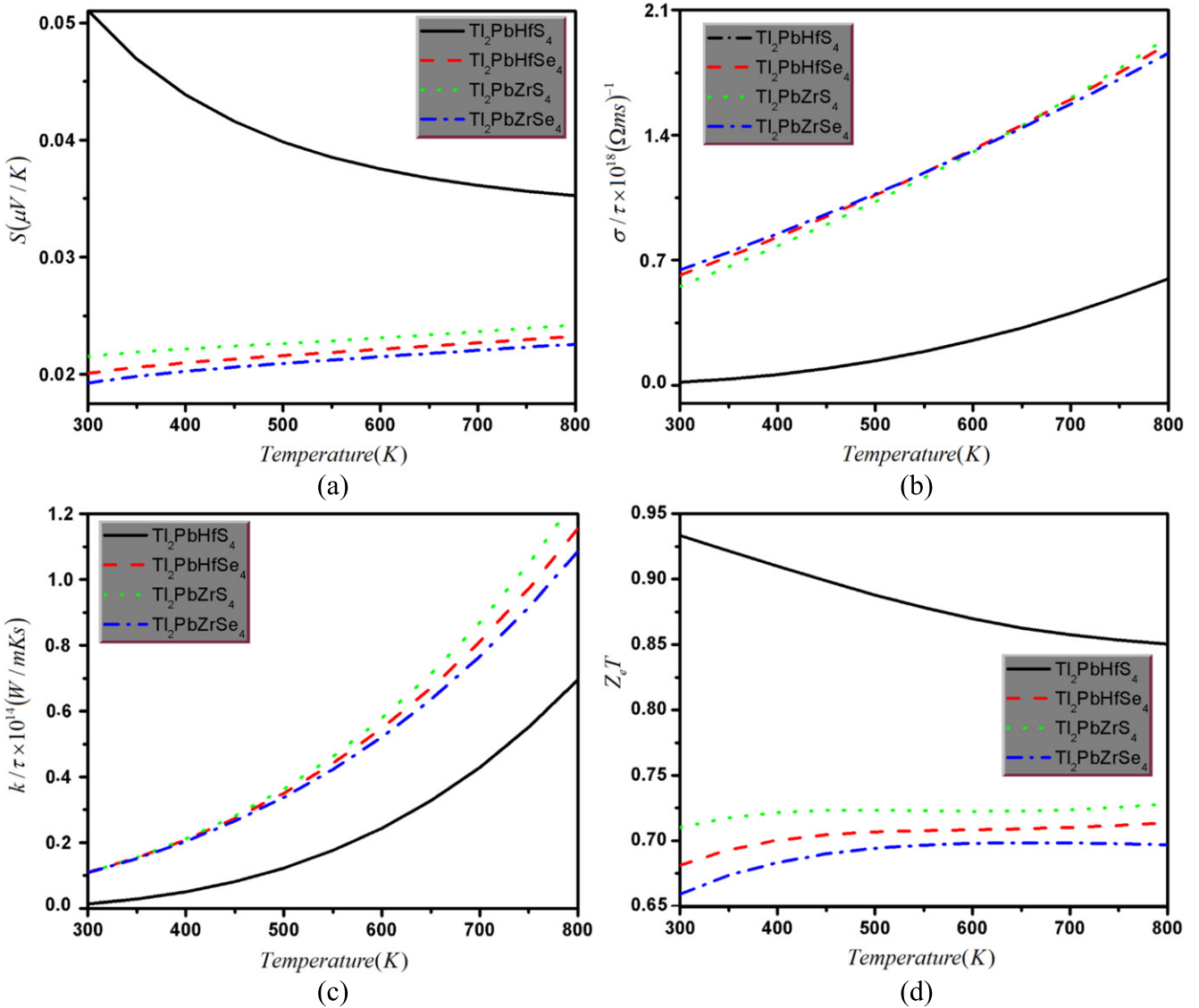


Figure 6. Calculated Seebeck coefficient S (a), electrical conductivity σ (b), thermal conductivity κ (c) and figure of merit $Z_e T$ (d).

temperature, electrical conductivity, and thermal conductivity due to electrons and the lattice, respectively. Using the Boltzmann theory as implemented in the BoltzTraP code [9, 12], we calculated the average Seebeck coefficient (S^{ave}), thermal conductivity (κ^{ave}), electrical conductivity (σ^{ave}) and figure of merit (ZT) for Tl_2PbXY_4 ($X = Zr, Hf$ and $Y = S, Se$) compounds from 300 K to 800 K. In figure 6(a), the variation in the average Seebeck coefficient as a function of temperature is shown. Materials possessing a high Seebeck coefficient (S) are considered good thermoelectric materials for converting maximum heat to electrical power. It is apparent from figure 6(a) that the Seebeck coefficient (S^{ave}) is positive for all the Tl_2PbXY_4 compounds, indicating the existence of p-type conduction. For Tl_2PbHfS_4 , a comparatively large S^{ave} is observed with a peak value of $5.110 \times 10^{-4} V K^{-1}$ at 300 K followed by a steep decrease in S^{ave} up to 540 K. Furthermore, S^{ave} decreases with increasing temperature to reach a value of $3.610 \times 10^{-4} V K^{-1}$ at 800 K. At 300 K, the S^{ave} values for $Tl_2PbHfSe_4$, Tl_2PbZrS_4 and

$Tl_2PbZrSe_4$ are $2.010 \times 10^{-4} V K^{-1}$, $2.1510 \times 10^{-4} V K^{-1}$ and $1.910 \times 10^{-4} V K^{-1}$, respectively. As the temperature increases, small variations in S^{ave} occur, and maximum values of 2.2510×10^{-4} , 2.4010×10^{-4} and $2.1510 \times 10^{-4} V K^{-1}$ are attained at 800 K for $Tl_2PbHfSe_4$, Tl_2PbZrS_4 and $Tl_2PbZrSe_4$, respectively. The calculated Seebeck coefficient for $Tl_2PbHfSe_4$ shows good agreement with the experimental work of [9]. The lattice and electronic parts contribute to the total thermal conductivity and each of them varies differently with temperature. In the theoretical model, we ignore the lattice thermal conductivity k_{lat} and pay attention to the electronic part of the thermal conductivity k_{ele} . Thermal conductivity varies directly with the following parameters: (i) carrier concentration, (ii) electrical conductivity and (iii) mobility of the carrier, i.e. $k_{ele} = \sigma \mu n$. The temperature-dependent electronic thermal conductivity (κ^{ave}) spectra for Tl_2PbXY_4 ($X = Zr, Hf$ and $Y = S, Se$) are shown in figure 6(c). From the overall trend of the κ^{ave} spectra, more heat transfers are observed when moving toward higher temperatures, resulting in an

increase in the thermal conductivity with increasing temperature. The average electronic thermal conductivity (κ^{ave}) for $\text{Ti}_2\text{PbHfS}_4$ is nearly zero at 300 K, and a steep increase is observed at 450 K. At 800 K, a maximum value of $6.310^{13} \text{ Wm}^{-1} \text{ K}^{-1}$ for κ^{ave} is observed. Similarly, for $\text{Ti}_2\text{PbHfSe}_4$, $\text{Ti}_2\text{PbZrS}_4$ and $\text{Ti}_2\text{PbZrSe}_4$, a κ^{ave} value of $1.010^{13} \text{ Wm}^{-1} \text{ K}^{-1}$ is observed at 300 K, and this value then increases rapidly above 400 K. The maximum peak values (at 800 K) of κ^{ave} for $\text{Ti}_2\text{PbHfSe}_4$, $\text{Ti}_2\text{PbZrS}_4$ and $\text{Ti}_2\text{PbZrSe}_4$ are 1.0910^{13} , 1.1610^{13} and $1.210^{13} \text{ Wm}^{-1} \text{ K}^{-1}$, respectively.

The average electrical conductivity (σ^{ave}) as a function of temperature was calculated, as shown in figure 6(b). Our calculated electrical conductivity for $\text{Ti}_2\text{PbHfSe}_4$ shows good agreement with the experimental work [10]. A material with greater electrical conductivity is a good thermoelectric device because it minimizes the Joule heating effect. It is apparent from figure 6(b) that σ^{ave} increases with increasing temperature from 300 K to 800 K. For $\text{Ti}_2\text{PbHfS}_4$, the average electrical conductivity is very small, nearly zero, at 300 K and then begins to increase gradually above 300 K. Further increasing the temperature above 450 K results in a steep increase in σ^{ave} . The value reaches a maximum at 800 K with a peak value of $5.810^{17} (\Omega \cdot \text{m} \cdot \text{s})^{-1}$. For the remaining three compounds, the average electrical conductivity starts with a value above $5.610^{17} (\Omega \cdot \text{m} \cdot \text{s})^{-1}$ at 300 K and then increases linearly with further increases in temperature. At 800 K, the peak values of σ^{ave} are 1.8810^{18} , 1.9310^{18} and $1.9710^{18} (\Omega \cdot \text{m} \cdot \text{s})^{-1}$ for $\text{Ti}_2\text{PbHfSe}_4$, $\text{Ti}_2\text{PbZrS}_4$ and $\text{Ti}_2\text{PbZrSe}_4$, respectively. The thermoelectric figure of merit (ZT) is plotted as a function of temperature in figure 6(d). The figure of merit (ZT) for $\text{Ti}_2\text{PbHfS}_4$ has a maximum value of 0.93 at 300 K and then the value decreases with increasing temperature, reaching a value of 0.85 at 800 K. For the $\text{Ti}_2\text{PbHfSe}_4$, $\text{Ti}_2\text{PbZrS}_4$ and $\text{Ti}_2\text{PbZrSe}_4$ compounds, ZT starts with lower values of 0.68, 0.71 and 0.66, respectively, at 300 K and increases up to 420 K. Above 420 K, no considerable incremental variations in ZT are noted with further increases in temperature. At 800 K, the largest values of ZT for the $\text{Ti}_2\text{PbHfSe}_4$, $\text{Ti}_2\text{PbZrS}_4$ and $\text{Ti}_2\text{PbZrSe}_4$ compounds are 0.70, 0.725 and 0.675, respectively. Because a material with ZT equal to one is considered the most suitable for thermoelectric device applications [1–5], $\text{Ti}_2\text{PbHfS}_4$ with $ZT = 0.93$ is considered a good candidate for thermoelectric devices.

4. Conclusions

The electronic structures of $\text{Ti}_2\text{PbHfS}_4$, $\text{Ti}_2\text{PbHfSe}_4$, $\text{Ti}_2\text{PbZrS}_4$ and $\text{Ti}_2\text{PbZrSe}_4$ have been studied using DFT. In this paper, we used GGA + U and SOC to treat the exchange correlation potential and to address the strongly correlated f-electrons. In addition, we examined the thermoelectric properties of the investigated compounds using the Boltzmann transport theory. The presented chalcogenides exhibit indirect band gaps of approximately 0.911, 0.659, 0.983 and 0.529 eV for $\text{Ti}_2\text{PbHfS}_4$, $\text{Ti}_2\text{PbHfSe}_4$, $\text{Ti}_2\text{PbZrS}_4$ and $\text{Ti}_2\text{PbZrSe}_4$, respectively. These relatively low band gap values might lead us to consider them to be potentially suitable for thermoelectric devices. The

calculated thermoelectric properties were then reported as functions of temperature. At 800 K, the largest values for the figure of merit for the $\text{Ti}_2\text{PbHfSe}_4$, $\text{Ti}_2\text{PbZrS}_4$ and $\text{Ti}_2\text{PbZrSe}_4$ compounds were found to be 0.70, 0.725 and 0.675, respectively. One can conclude that $\text{Ti}_2\text{PbHfS}_4$ with $ZT = 0.93$ is a good candidate for thermoelectric devices. We completed this investigation by reporting the optical properties where we observed that the reflectivity for all investigated chalcogenides was approximately 45%.

Acknowledgments

The first four authors were supported within the CENTEM project, reg. no. CZ.1.05/2.1.00/03.0088, co-funded by the ERDF as part of the Ministry of Education, Youth and Sports OP RDI program and, in the follow-up sustainability stage, supported through CENTEM PLUS (LO1402) with financial support from the Ministry of Education, Youth and Sports under the National Sustainability Programme I. Meta-Centrum (LM2010005) and CERIT-SC (CZ.1.05/ 3.2.00/08.0144) infrastructures. The authors RK and SBO acknowledge support from the National Plan for Science, Technology and Innovation under research project No. 11-NAN1465-02.

References

- [1] Kleinke H 2010 *J. Chem. Mater.* **22** 604–11
- [2] Toberer E S, May A F and Snyder G 2010 *J. Chem. Mater.* **22** 624–34
- [3] Kanatzidis M G 2010 *J. Chem. Mater.* **22** 648–59
- [4] Rowe D M 2006 *Thermoelectrics Handbook: Macro to Nano* (Boca Raton, FL: CRC Press)
- [5] Kadel K, Kumari L, Li W Z, Huang J Y and Provencio P P 2011 *Nanoscale Res. Lett.* **6** 57
- [6] Zhang Q, Cao F, Liu W, Lukas K, Yu B, Chen S, Opeil C, Broido D, Chen G and Ren Z 2012 *J. Am. Chem. Soc.* **134** 10031–8
- [7] Mrotzek A, Chung D Y, Hogan T and Kanatzidis M G 2000 *J. Mater. Chem.* **10** 1667
- [8] Khan W and Goumri-Said S 2015 *RSC Adv.* **5** 9455–61
- [9] Sankar C R, Assoud A and Kleinke H 2013 *Inorg. Chem.* **52** 13869–74
- [10] Kohn W and Sham L S 1965 *Phys. Rev. A* **140** 1133
- [11] Hohenberg P and Kohn W 1964 *Phys. Rev. B* **136** 864
- [12] Madsen G K H and Singh D J 2006 *Comput. Phys. Commun.* **67** 175
- [13] Blaha P, Schwarz K, Madsen G K H, Kvasnicka D and Luitz J 2001 *WIEN2k, an Augmented Plane Wave Plus Local Orbitals Program for Calculating Crystal Properties* (Vienna: Vienna University of Technology)
- [14] Petukhov A G 2003 *Phys. Rev. B* **67** 153106
- [15] Ud Din H and Reshak A H 2014 *Comput. Mater. Sci.* **83** 474–80
- [16] Ali R, Murtaza G, Takagiya Y, Khenata R, Uddin H, Ullah H and Khan S A 2014 *Chin. Phys. Lett.* **31** 047102
- [17] Ud Din H, Azam S, Khan S A and Khenata R 2014 *J. Alloys Compd.* **615** 507–13
- [18] Azam S and Reshak A H 2013 *Int. J. Electrochem. Sci.* **8** 10359–75
- [19] Snyder G J and Toberer E S 2008 *Nat. Mater.* **7** 105
- [20] Hochbaum A I, Chen R, Delgado R D, Liang W, Garnett E C, Najarian N, Majumdar A and Yang P 2008 *Nature* **451** 2008



Transport properties of APdCu(Se₂)(Se₃) (A = K and Rb): new quaternary copper palladium polyselenides

Sikander Azam^{*a} and A. H. Reshak^{ab}

Cite this: *RSC Adv.*, 2014, 4, 20102

Received 20th March 2014

Accepted 7th April 2014

DOI: 10.1039/c4ra02465f

www.rsc.org/advances

The electronic structure, effective mass, optical properties and electrical transport coefficients of APdCu(Se₂)(Se₃) (where A = K and Rb), a new quaternary copper palladium polyselenide, were investigated using a density functional theory calculation within a generalized gradient approximation (GGA) plus the Hubbard term (*U*) (GGA + *U*). The electronic band structure shows that the calculated compounds have a direct band gap. From the partial density of states we found that, at an energy of −5.0 eV: (1) the Pd-s state strongly hybridizes with the Se-p state; (2) near the Fermi level the Se-p state hybridizes with the Cu-p state; and (3) at the lower conduction band the Pd-s state forms a strong hybridization with the Cu-s state. The investigation of electronic charge density shows that the Pd–Se and Cu–Se atoms form weak covalent bonds and have strong ionicity, whereas the K/Pd atoms exhibit pure ionic bonding. We also calculated the dielectric function, refractive index, extinction coefficient, absorption coefficient and reflectivity of the compounds. The calculated transport coefficients show the anisotropic nature of the compounds, in agreement with their electronic states. The transport properties reveal stronger carrier transport along the Cu-p/d and Pd-d orbitals, indicating that these orbitals are mainly responsible for the electrical transport. The maximum power factor values of the KPdCu(Se₂)(Se₃) (RbPdCu(Se₂)(Se₃)) compounds as a function of relaxation time reach 2.2 (1.8) × 10¹¹, 4.4 (3.5) × 10¹¹ and 1.3 (1.4) × 10¹¹ within *P^{xx}*, *P^{yy}* and *P^{zz}* components, respectively.

1. Introduction

Chalcogenide compounds have a very diverse and interesting structural chemistry and show useful physical and chemical properties that may be applicable to modern technologies.¹ The synthesis of binary and ternary chalcogenides has been extensively studied using high temperature solid state, intermediate temperature flux, and low temperature solvothermal techniques. However, comparatively little is known about quaternary chalcogenides, which may also demonstrate interesting properties.^{2–5} The synthesis of novel quaternary chalcogenides has recently become an active area of research in solid state chemistry.^{2,4,5} Most known quaternary chalcogenides are made using the molten alkali metal polychalcogenide flux technique, although low temperature solvo(hydro)thermal reactions have produced a limited number of quaternary chalcogenides.⁶

Pd-holding compounds have received much consideration as a result of the catalytic functions of the metal and its capacity to form polychalcogenide complexes in solution. Several ternary Pd polychalcogenides have now been isolated and structurally

characterized. These include: (Ph₄P)₂[Pd(Se₄)₂], with distinct [Pd(Se₄)₂]^{2−} anions in which each Pd²⁺ is coordinated by two chelating (Se₄)^{2−} ligands;⁷ {(CH₃)N(CH₂CH₂)₃N}₂[Pd(Se₆)₂] and (enH)₂[Pd(Se₅)₂], which feature sheet-like, two-dimensional Pd polyselenide anionic frameworks;⁸ Rb₂[Pd(Se₄)₂]Se₈, encompassing the sheet-like polyanion [Pd(Se₄)₂]^{2−} with intercalated crown-like Se₈ eight-membered rings;⁹ and K₄[Pd(Se₄)₂][Pd(Se₆)₂] (= K₂PdSe₁₀) and Cs₂[Pd(Se₄)₂] (= Cs₂PdSe₈) with three-dimensional structures assembled from two interpenetrating [Pd(Se_{*x*})₂]^{2−} structures (*x* = 4 and 6 for the K⁺ saline, *x* = 4 and 4 for the Cs⁺ salt).^{10,11}

In the system A–M–M′–Q (A = alkali steel, M = assembly I element, M′ = assembly VIII steel, Q = chalcogen), only a few Fe compounds with the crystal formula AMFeQ₂ (A = Li, Na, K, Cs; M = Cu, Ag; Q = S, Se, Te) are known.^{12–16} In 2003, Chen *et al.*¹⁷ reported the groundwork, crystal organization, and optical and thermal properties of two innovative mixtures: APdCu(Se₂)(Se₃) (A = K and Rb), which were the first quaternary copper palladium polychalcogenides obtained by solvothermal procedures utilizing ethylenediamine (en) as the reaction medium. The target of the present study was the evaluation of APdCu(Se₂)(Se₃) (A = K and Rb). We calculated the thermoelectric properties of the compounds, which have not previously been reported.

This paper aims provide a systematic study of the electronic band structure and optical and thermoelectric properties of

^aNew Technologies – Research Centre, University of West Bohemia, Univerzityni 8, 306 14 Pilsen, Czech Republic. E-mail: sikander.physicst@gmail.com

^bCenter of Excellence Geopolymer and Green Technology, School of Material Engineering, University Malaysia Perlis, 01007 Kangar, Perlis, Malaysia

Paper

APdCu(Se₂)(Se₃) (A = K and Rb) using density functional theory (DFT) + *U* calculations. The generalized gradient approximation (GGA) + *U* exchange potential approximation was used to calculate accurately the electronic band structure and optical and thermoelectric properties of APdCu(Se₂)(Se₃) (A = K and Rb) as the DFT + *U* scheme for solids has been shown to give better band gaps than semi-local DFT methods.^{18,19}

The optical properties help us to obtain a deep insight into the structure of APdCu(Se₂)(Se₃) (A = K and Rb). The electrical transport parameters (conductivity, Seebeck coefficient, power factor) for the compound system were obtained theoretically based on the DFT calculations and the rigid band approach.

We briefly describe the computational method used in this study and then present and discuss the most relevant results obtained for the electronic, optical and thermoelectric properties of APdCu(Se₂)(Se₃) (A = K and Rb).

2. Methodology

It was recently reported that the local density approximation (LDA) and GGA schemes are insufficient to describe correctly the electronic structure of transition metal oxides.²⁰ The GGA + *U* (where *U* is the Hubbard term) method was therefore applied here to account for on-site correlation at the transition metal sites. The GGA + *U* method, which accounts for an orbital dependence of the Coulomb-exchange interaction, was used. The crystal structure of the new quaternary copper palladium polyselenides with monoclinic symmetry was determined by Chen *et al.*¹⁷ The unit cell with the formula APdCu(Se₂)(Se₃) (A = K and Rb) was modeled for the pure phase property calculation simulations, *i.e.* the electronic states and transport parameter calculation. The unit cell crystal structures for both compounds are illustrated in Fig. 1. Calculations with the full potential linear augmented plane wave method based on DFT^{21,22} theory were performed using the Wien2k package.²³ The exchange and correlation were computed within GGA + *U*.²⁴

The ground state properties of the resulting optimized structures were computed by performing self-consistent interactions until the iterative convergence of energy and charge to values of $<10^{-5} R_y$ and $<10^{-4} C$, respectively. We calculated the bond lengths and angles, which show good agreement with the experimental data¹⁷ (Tables 1 and 2). We used the parameter $R_{MT}K_{MAX} = 7$ (where R_{MT} is the smallest of the muffin-tin radii and K_{MAX} is the plane wave cutoff) to control the size of the basis set for the wave functions. The electronic band structure, total and partial density of states and the linear optical susceptibilities were calculated using summation over 1000 *k*-points within the IBZ. The Monkhorst-pack grid $11 \times 10 \times 8$ was used for *k*-point sampling in the electronic state calculation. The high symmetry *k*-points in the Brillouin zone (BZ) within our calculated band structure are $Z \rightarrow B \rightarrow G \rightarrow Y \rightarrow G \rightarrow Z$. To initiate the calculations, we used the experimental values for lattice parameters from Chen *et al.*¹⁷ The atomic positions are fully optimized by minimizing the forces acting on each atom. The optical properties of matter can be described by the dielectric function $\epsilon(\omega)$. In the limit of linear optics, neglecting electron polarization effects and within the frame of random

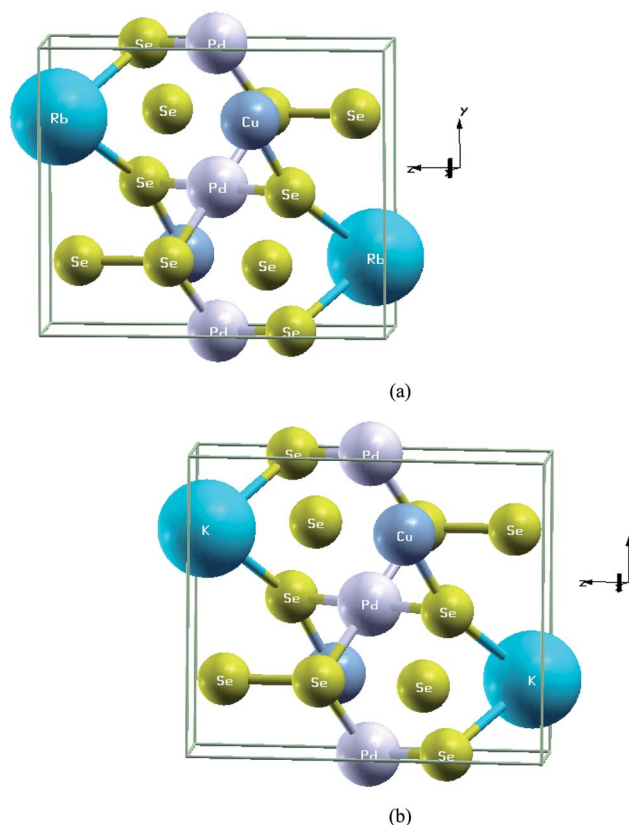


Fig. 1 Unit cell structures. (a) RbPdCu(Se₂)(Se₃) unit cell structure; and (b) KPdCu(Se₂)(Se₃) unit cell structure.

phase approximation, the expression for the imaginary part $\epsilon_2(\omega)$ of the dielectric function is calculated from the momentum matrix elements between the occupied and unoccupied wave functions. The real part $\epsilon_1(\omega)$ of the dielectric function is evaluated from the imaginary part $\epsilon_2(\omega)$ by the Kramers–Kronig transformation. The other optical constants, such as the reflective index, extinction coefficient, reflectivity and energy-loss spectrum can be obtained from $\epsilon_1(\omega)$ and $\epsilon_2(\omega)$.

The electrical transport coefficients were calculated within the framework of semi-classical Boltzmann theory and the rigid band approach by analyzing the band structure from the DFT calculations.^{25,26} The transport distribution function to conductivity within the rigid band approach is based on the following tensor:

$$\sigma_{\alpha\beta}(\epsilon) = \frac{1}{N} \sum_{i,k} \sigma_{\alpha\beta}(i, k) (\epsilon - \epsilon_{i,k}) \quad (1)$$

where $1/N$ accounts for the normalization of the sum so it is the integral in the limit where the number of grid points becomes dense, $\epsilon_{i,k}$ is the electron band energy for band *i* at the Brillouin *k* point and $\sigma_{\alpha\beta}(i, k)$ is the *k*-dependent conductivity tensor expressed as

$$\sigma_{\alpha\beta}(i, k) = e^2 \tau_{i,k} \nu_{\alpha}(i, k) \nu_{\beta}(i, k) \tau \quad (2)$$

where the $\nu_{\alpha}(i, k)$, $\nu_{\beta}(i, k)$, τ are the components of the band velocities and the relaxation time, respectively. In the band velocity expression, $\nu_{\alpha}(i, k)$ *i* denotes the bands, *k* denotes the

Table 1 Bond lengths in angstroms

KPdCu(Se ₂)(Se ₃)	Optimized	Experimental	RbPdCu(Se ₂)(Se ₃)	Optimized	Experimental
Cu–Se4	2.3657	2.369(1)	Pd–Se4	2.4760	2.454(2)
Cu–Se1	2.4571	2.467(2)	Cu–Se4	2.3598	2.362(2)
Cu–Se3	2.3765	2.411(2)	Cu–Se3	2.3748	2.411(4)
K–Se3	3.4387	3.458(4)	Cu–Se1	2.4583	2.479(3)
Pd–Se1	2.4723	2.4515(9)	Se1–Se2	2.3794	2.337(4)
Pd–Se4	2.4758	2.458(1)	Se3–Se4	2.4441	2.383(2)
Se1–Se2	2.3851	2.338(2)	Rb–Se2	3.4140	3.407(3)
K–Se4	3.4121	3.423(3)	Rb–Se2	3.6681	3.420(3)
K–Se2	3.6625	3.6656(7)	Rb–Se2	3.6681	3.6702(7)
K–Se2	3.3297	3.349(4)	Rb–Se3	3.5010	3.524(4)
K–Se2	3.2941	3.299(3)	Pd–Se1	2.4746	2.455(2)
Se3–Se4	2.4484	2.390(1)	Rb–Se4	3.6209	3.525(3)
K–Se4	3.5072	3.541(3)	Rb–Se4	3.5089	3.656(3)

Table 2 Bond angles in degrees

KPdCu(Se ₂)(Se ₃)	Experimental	Optimized	RbPdCu(Se ₂)(Se ₃)	Experimental	Optimized
Se(1)–Pd–Se(4)	87.20(4)	87.22	Se(4)–Pd–Se(1)	87.55(7)	87.47
Se(1)–Pd–Se(4)	92.80(4)	92.78	Se(4)–Pd–Se(1)	92.45(7)	92.53
Se(1)–Pd–Se(1)	180	180	Se(1)–Pd–Se(1)	180	180
Se(4)–Pd–Se(4)	180	180	Se(4)–Pd–Se(4)	180	180
Se(3)–Cu–Se(1)	85.19(7)	85.48	Se(3)–Cu–Se(1)	84.6(1)	85.15
Se(4)–Cu–Se(4)	108.08(8)	106.77	Se(4)–Cu–Se(4)	107.8(1)	106.16
Se(4)–Cu–Se(1)	112.06(6)	111.11	Se(4)–Cu–Se(1)	114.2(1)	113.60
Se(4)–Cu–Se(3)	118.77(5)	120.15	Se(4)–Cu–Se(3)	117.4(1)	118.69
Se(4)–Se(3)–Se(4)	91.78(6)	90.26	Se(4)–Se(3)–Se(4)	92.8(1)	91.24
Se(3)–Se(4)–Pd	107.53(5)	106.20	Se(3)–Se(4)–Pd	107.74(9)	106.21
Se(2)–Se(1)–Pd	111.05(4)	109.65	Se(2)–Se(1)–Pd	110.73(8)	109.25
Pd–Se(1)–Pd	95.67(5)	94.60			

wave vector and α denotes the direction. The transport coefficients can then be determined by integrating the tensor within eqn (1) as a function of temperature as:

$$\sigma_{\alpha\beta}(T, \mu) = \frac{1}{\Omega} \int \sigma_{\alpha\beta}(\varepsilon) \left[-\frac{\partial f_{\mu}(T, E)}{\partial \varepsilon} \right] d\varepsilon \quad (3)$$

where f is the Fermi distribution function, T is absolute temperature, μ is the chemical potential, ε is the energy and Ω is the volume. In the rigid band approach, the bands and $\sigma(\varepsilon)$ are fixed as only one band structure assessment is required.²⁷ The amount of carriers can be altered by varying the chemical potential μ . The thermal properties can be calculated from the band structure results except for the relaxation time. Theoretically, the relaxation time period is correlated with the crystal structure, temperature, doping content, microstructure and texture of specific materials.²⁸

In general, the value of τ_e is determined by the ratio of the carrier energy $\varepsilon_{i,k}$ and the attained vibrational energy of atoms. The carrier power, $\varepsilon_{i,k}$ is dependent on the power catalogue i and the wave vector k , and the attained vibrational power of atoms is of the order of magnitude of $K_{\beta}T$. Much analytical research is needed to elucidate the scattering means and to determine the approximate value of τ_e for specific materials. Regardless of this, the relaxation time τ_e has been broadly measured as a constant and the carrier scattering has been assumed to be

independent of the vector direction and temperature for the approximation of the real scattering means for convenience of calculation.^{29,30}

Using the constant relaxation time approximation, the Seebeck coefficient can be determined by:

$$\alpha = \pm \frac{1}{eT} \left[E_F - \int_0^{\infty} g(E) \tau_e E^2 \frac{df_0(E)}{dE} \right] / \left[\int_0^{\infty} g(E) \tau_e E \frac{df_0(E)}{dE} \right] \quad (4)$$

where e , E_F , $g(E)$ and τ_e are the electron charge, the Fermi level, the density of state and the relaxation time, respectively.³¹ The Fermi level (E_F) and the density of state $g(E)$ as a function of E can be obtained from the calculated DFT results and the relaxation time τ_e is treated as roughly constant, therefore the Seebeck coefficient as a function of temperature T can be determined. The BoltzTraP program was used for the assessment of the k -dependent conductivity tensor. The BoltzTraP program relies on a smoothed Fourier interpolation to obtain an analytical expression of the bands.³² The initial k mesh was interpolated up to a mesh five times denser than the original.

3. Results and discussion

3.1. Electronic structure

The GGA method is insufficient to describe systems in which the d-electrons are well localized and in which the spin orbital

Paper

interactions cannot be neglected, particularly their electronic properties. However, the GGA + U approach has been suggested to describe these systems. In this approach, the Hubbard term (U), which describes the d–d or f–f orbital interaction, is added to the GGA energy. This method has proved to be effective for describing strongly correlated systems.

We noticed that the band structures of the spin-up states are similar to those of the spin-down states. The electronic band structures of the monoclinic symmetry $\text{KPdCu}(\text{Se}_2)(\text{Se}_3)$ and $\text{RbPdCu}(\text{Se}_2)(\text{Se}_3)$ compounds were calculated and the calculated band structure profiles using the GGA + U approach are shown in Fig. 2. The electronic band dispersion curves are shown in addition to some high symmetry directions of the BZ for $\text{KPdCu}(\text{Se}_2)(\text{Se}_3)$ and $\text{RbPdCu}(\text{Se}_2)(\text{Se}_3)$ compounds. We will only consider the consequences of EV-GGA due to its improved band gap. The valence band maximum (VBM) and the conduction band minimum (CBM) are positioned at the Y

point of BZ, resulting in a direct energy band gap of about 1.258/1.275 for $\text{KPdCu}(\text{Se}_2)(\text{Se}_3)/\text{RbPdCu}(\text{Se}_2)(\text{Se}_3)$. The calculated electronic structure of $\text{KPdCu}(\text{Se}_2)(\text{Se}_3)$ and $\text{RbPdCu}(\text{Se}_2)(\text{Se}_3)$ verifies that the investigated compounds are narrow gap semiconductors. To determine the nature of the electronic band structures, we calculated the total (TDOS) and partial (PDOS) density of states (DOS) for both compounds. A study of the DOS using the GGA + U approximation in both the spin-up and spin-down states shows that there is no remarkable difference between the two states (Fig. 3). Fig. 3 shows that there are three distinct structures separated by gaps. The first structure encountered in the TDOS (starting from the lower energies) consists entirely of K-p, Se-s and Rb-d states. These peaks are centered at about -14.0 to -10.0 eV for both compounds. The next structure, between -5.0 and 0.0 eV for both compounds, consists of the Pd-s/p, Cd-p/d and Se-p states. The conduction bands consist of Pd-s, Cu-s, Se-d, K-s

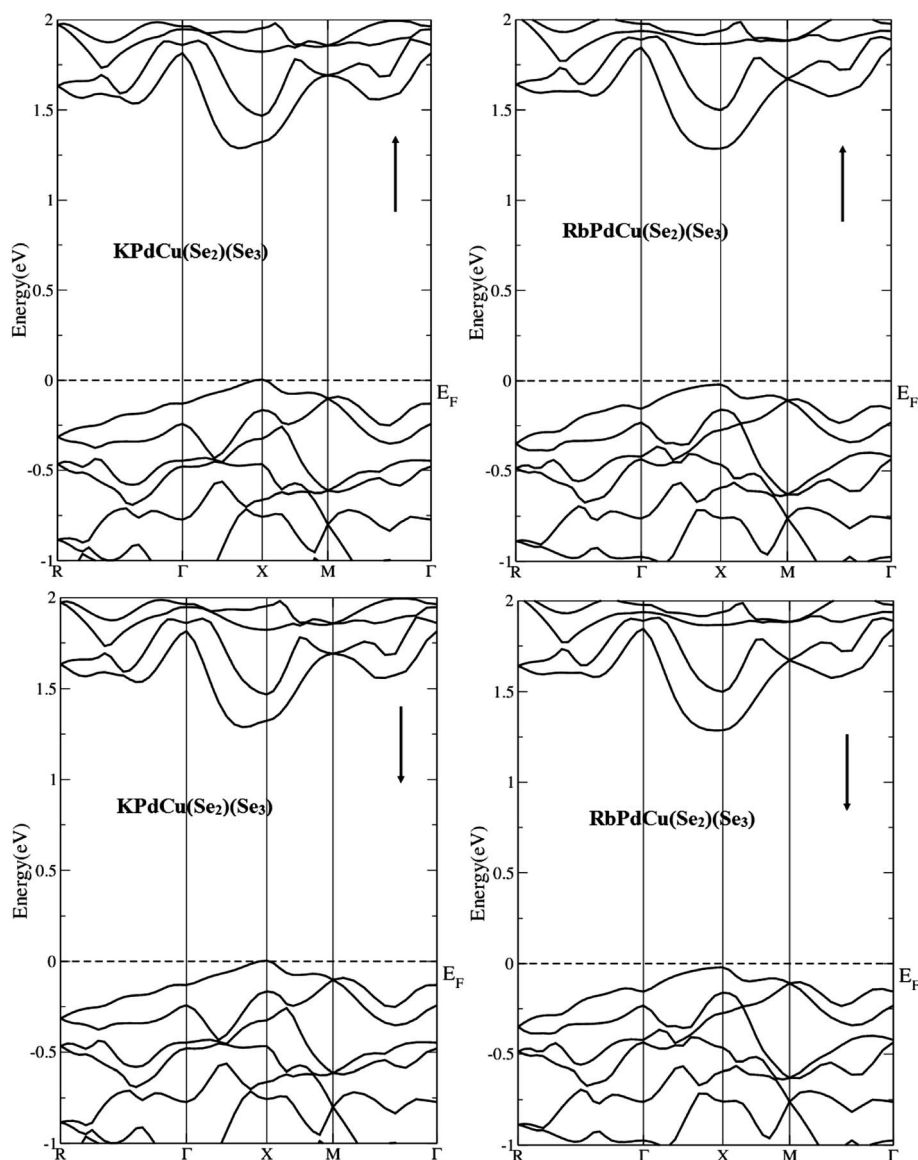


Fig. 2 Calculated band structures.

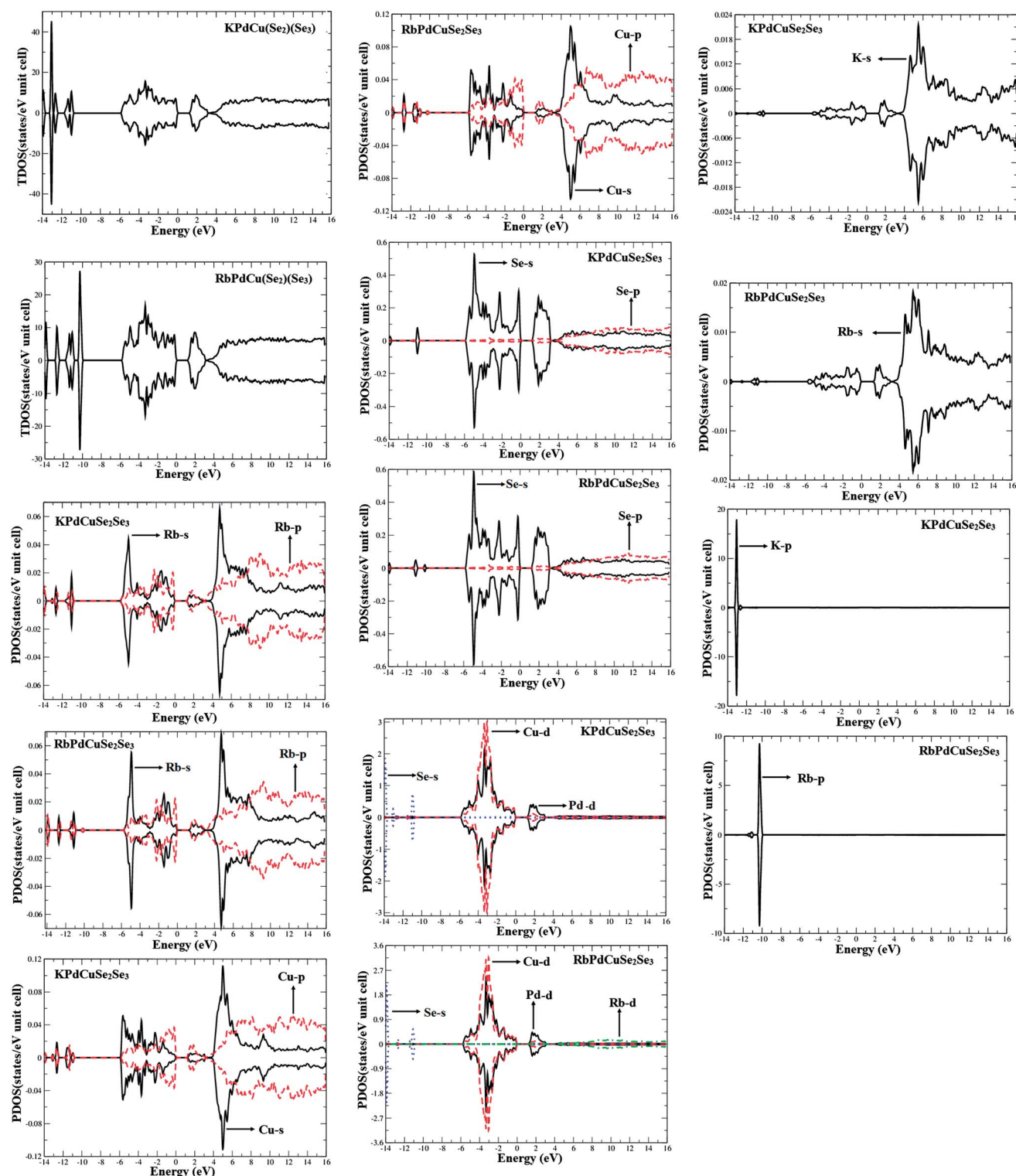


Fig. 3 Calculated total and partial densities of states (states per eV unit cell).

and Rb-d states. From the PDOS, we also concluded that at an energy of -5.0 eV, the Pd-s state forms a strong hybridization with the Se-p state. Near the Fermi level, the Se-p state hybridizes with the Cu-p state and at the low conduction band the Pd-s state strongly hybridizes with the Cu-s state.

3.2. Electron charge density

To establish a quantitative estimation for the type of bonding present in a particular molecule, it is necessary to have a measure of the extent of charge transfer present in the molecule relative to the charge distributions of the separated atoms. To

Paper

calculate the type of bonding in both the investigated compounds, we evaluated the atomic charge distributions using the FP-LAPW method based on the DFT. The electron density contours give another approach to investigating the bonding interactions in solid materials and the changes in bonding which consequently lead to changes in the DOS.

The valence electronic charge density spectra are shown in Fig. 4 along the (110) crystallographic plane to help to understand the distribution of the total electronic charge density maps of the KPdCu(Se₂)(Se₃) and KPdCu(Se₂)(Se₃) compounds. The crystallographic planes show that there is both ionic and partial covalent bonding between the K, Rb, Pd, Cu and Se atoms depending on the Pauling electronegativity difference, *i.e.* the higher the associated electronegativity number, the more an element or compound attracts electrons towards it. The electronegativity of the K atom is (0.82), and the values for the other atoms are: Rb (0.79), Pd (2.20), Cu (1.90) and Se (2.55). The atoms Pd–Se and Cu–Se form weak covalent bonds and have strong ionicity, while the K/Pd atoms show pure ionic bonding. From these contour plots it can be seen that most of the Pd and Cu electronic charge is transferred to the Se atom. This can easily be seen by the color charge density scale, where blue (+1.0000) corresponds to the maximum charge accumulating site. The charge density along Pd and Se is pronounced. It is clear that when we replace K by Rb, the charge density decreases. As is clear from Fig. 4a, the charge density around Rb and Se is greater in KPdCu(Se₂)(Se₃) than in RbPdCu(Se₂)(Se₃).

3.3. Effective mass

We calculated the effective mass of electrons (m_e^*) from the electronic band structure. As we were interested in the energy bands around the Fermi level (E_F), we enlarged the band structure near E_F to show the bands which govern the energy band gap, *i.e.* the CBM and VBM. The values for the effective mass of electrons (m_e^*) were anticipated from the curvature of

the conduction band minimum, band 125 for KPdCu(Se₂)(Se₃) and band 135 for RbPdCu(Se₂)(Se₃); these bands are highlighted in different colors (Fig. 2e and f). The diagonal elements of the effective mass tensor, m_e , for the electrons in the conduction band are calculated in the $\Gamma \rightarrow \Gamma$ direction in k space using the following well-known relation:

$$\frac{1}{m_e^*} = \frac{1}{\hbar^2} \frac{\partial^2 E(k)}{\partial k^2} \quad (5)$$

The effective mass of the electron is determined by fitting the electronic band structure to a parabolic function [eqn (5)] in the first BZ using the GGA + U approach. The effective mass of the electron for the (symmetry) is obtained from the curvature of the conduction band at the point Γ – Γ . The calculated effective mass ratios of the electron (m_e^*/m_e) for KPdCu(Se₂)(Se₃) and RbPdCu(Se₂)(Se₃) in the $\Gamma \rightarrow \Gamma$ direction are 0.0332 and 0.0225, respectively. The calculated value for KPdCu(Se₂)(Se₃) is larger than that for RbPdCu(Se₂)(Se₃). This is attributed to the fact that the parabolic curvature of RbPdCu(Se₂)(Se₃) is greater than that of KPdCu(Se₂)(Se₃) because the effective electron mass is inversely proportional to the curvature. We also calculated the effective mass of the heavy holes (the maximum valence band) and the light holes (the second maximum valence band) for KPdCu(Se₂)(Se₃) and RbPdCu(Se₂)(Se₃) from bands (134 and 133) and (124 and 123), respectively. The calculated values of the heavy holes and light holes for KPdCu(Se₂)(Se₃) are 0.1350 and 0.1858 and for RbPdCu(Se₂)(Se₃) 0.0202 and 0.0198, respectively.

3.4. Optical properties

The optical response functions of solids are often described by the complex dielectric function $\epsilon(\omega) = \epsilon_1(\omega) + i\epsilon_2(\omega)$ or by the complex refractive index $N(\omega) = n(\omega) + ik(\omega)$.

$$\epsilon_1(\omega) = n^2 - k^2 \quad (6)$$

$$\epsilon_2(\omega) = 2nk \quad (7)$$

In determining the interaction between light and a solid, an adiabatic approximation and single-electron approximation are generally used. As the transition frequencies both within-band and between bands are much larger than the phonon frequency in the calculation of electronic structure and the method used is a single-electron approximation, phonon participation in the indirect transition process can be ignored and only electronic excitation considered. According to the definitions of the direct transition probabilities and the Kramers–Kronig dispersion relations, the imaginary and the real parts of the dielectric function, absorption coefficient, reflectivity and complex optical conductivity^{33–35} can be deduced using:

$$\epsilon_2(\omega) = \frac{\pi e^2}{\epsilon_0 m^2 \omega^2} \sum_{V,C} \left\{ \int_{BZ} \frac{2dk}{(2\pi)^2} |a \times M_{V,C}|^2 \delta[E_C(k) - E_V(k) - \hbar\omega] \right\} \quad (8)$$

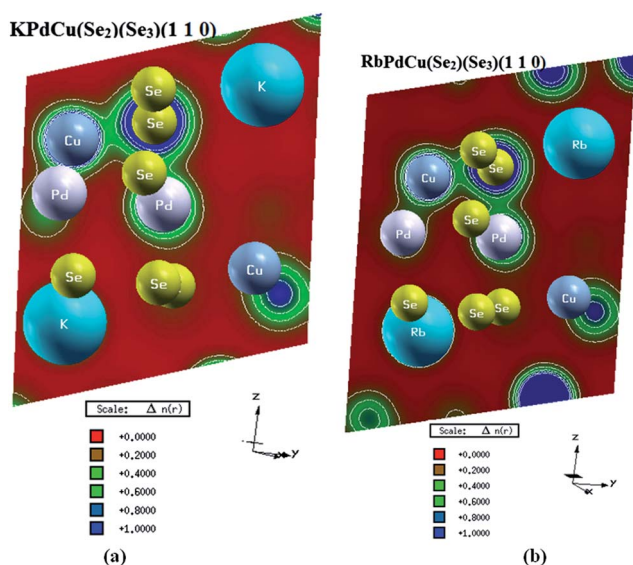


Fig. 4 Electronic charge density contours.

$$\varepsilon_1(\omega) = 1 + \frac{2e}{\varepsilon_0 m^2} \times \varepsilon_{V,C} \int_{BZ} \frac{2dk}{(2\pi)^2} \frac{|\mathbf{a} \times M_{V,C}(k)|^2}{E_C(k) - E_V(k)/\hbar} \times \frac{1}{[E_C(k) - E_V(k)]^2/\hbar^2 - \omega^2} \quad (9)$$

$$\alpha(\omega) = \frac{2k\omega}{c} = \frac{2\pi k}{\lambda_0} \quad (10)$$

$$R(\omega) = \frac{(n-1)^2 + k^2}{(n+1)^2 + k^2} \quad (11)$$

where n is the refractive index, k is the extinction coefficient, ε_0 is the vacuum dielectric constant, λ_0 is the wavelength of light in a vacuum, C and V are the conduction band and valence band, respectively, BZ is the first Brillouin zone, K is the electron wave vector, \mathbf{a} is the unit direction vector of the vector potential A , M_{VC} is the transition matrix element, ω is the angular frequency and $E_C(\omega)$ and $E_V(\omega)$ are the intrinsic energy levels of the conduction band and valence band, respectively.

An understanding of the electronic structures can be reached by investigating the optical spectra, which not only give information about the occupied and unoccupied states, but also about the features of the bands. Thus we investigated the optical properties of the KPdCu(Se₂)(Se₃) and RbPdCu(Se₂)(Se₃) compounds. The dielectric function connects the microscopic physical transitions between bands with the electronic structures of a solid, reflecting the band structure of the solid and providing information about its spectrum. In using KPdCu(Se₂)(Se₃) and RbPdCu(Se₂)(Se₃) as semiconductor materials, their spectra are generated by electronic transitions between energy levels and all the dielectric peaks can be explained using the calculated energy band structure and DOS. Fig. 5a and b show the spectra of the real and imaginary parts of the complex dielectric function *versus* the photon energy. As is clear from the above-mentioned calculation, there is no remarkable difference in the electronic structure of the spin-up and spin-down states, so the optical properties are discussed here using only the spin-up state. Our analysis of the $\varepsilon_2(\omega)$ spectrum (Fig. 5a) shows that the first critical point of the dielectric function occurs at 0.30 eV. This point is $Y_v - Y_c$, which gives the threshold for the optical transitions between the VBM and the CBM. This is known as the fundamental absorption edge. Beyond this threshold energy (the first critical point), the curve increases rapidly. This is because the number of points contributing towards $\varepsilon_2(\omega)$ increases abruptly. As the investigated compounds have a monoclinic symmetry, only three tensor components are needed to describe all the optical properties. These are: $\varepsilon_2^{xx}(\omega)$, $\varepsilon_2^{yy}(\omega)$ and $\varepsilon_2^{zz}(\omega)$. The main peak of the $\varepsilon_2^{xx}(\omega)$, $\varepsilon_2^{yy}(\omega)$ and $\varepsilon_2^{zz}(\omega)$ spectrum is at about 2.0 eV; there are also a second pronounced peak and three humps (Fig. 5a and b).

The real part of $\varepsilon_1(\omega)$ can be obtained using the Kramers–Kronig transformation. The results for the dispersive part of the dielectric function, $\varepsilon_1(\omega)$ for these compounds are shown in Fig. 5c and d. The main features in this spectrum are the peak around 1.8 eV, the rather steep decrease below 9.0 eV, after

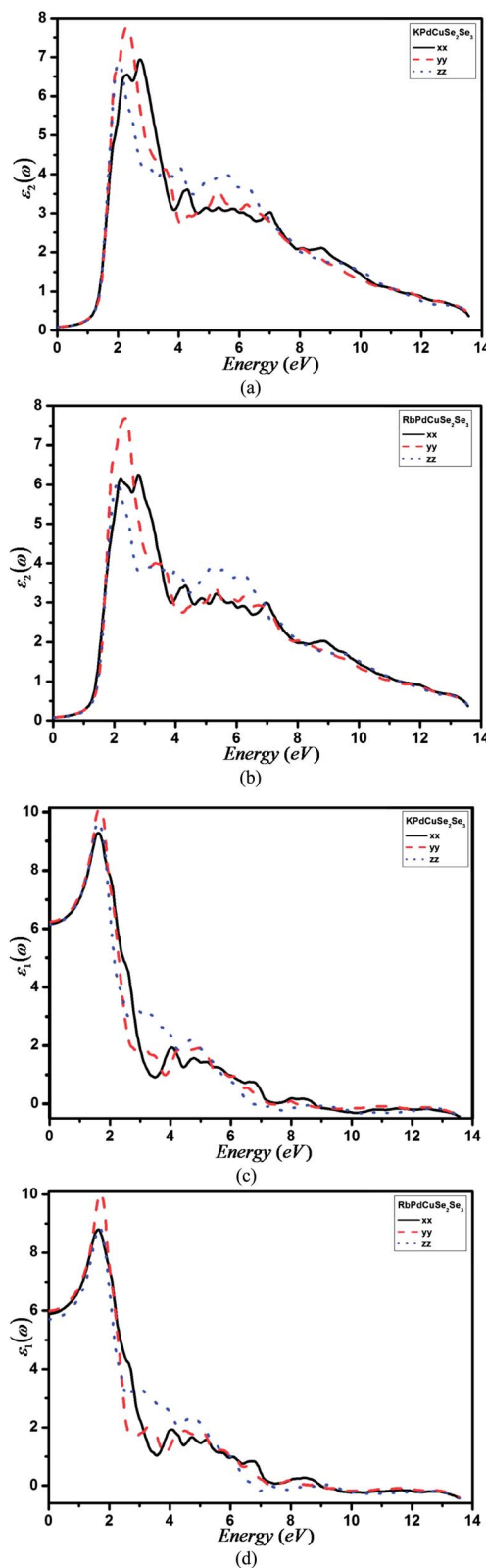


Fig. 5 Calculated imaginary $\varepsilon_2(\omega)$ and real $\varepsilon_1(\omega)$ parts of the dielectric tensor.

which $\varepsilon_1(\omega)$ becomes negative, and the minimum followed by a slow increase towards zero at high energies. In the energy range in which $\varepsilon_1(\omega)$ is negative, the electromagnetic wave is not

Paper

propagated. For the real dielectric function, the most important quantity is the zero frequency limit $\varepsilon_1(0)$, as this gives the static dielectric constant in the zero frequency limits, which has values of 6.168 (5.908), 6.240 (5.994) and 6.149 (5.718) for $\varepsilon_1^{xx}(0)$, $\varepsilon_1^{yy}(0)$ and $\varepsilon_1^{zz}(0)$ for $\text{KPdCu}(\text{Se}_2)(\text{Se}_3)$ and $(\text{RbPdCu}(\text{Se}_2)(\text{Se}_3))$, respectively.

Fig. 6a–h show the energy loss function $L(\omega)$, reflectivity $R(\omega)$, refractivity $n(\omega)$ and absorption coefficient $I(\omega)$. The complex refractive index [$\tilde{n}(\omega) = n(\omega) + ik(\omega)$] portrays the refraction and also the absorption of the compounds. It contains two parts: the real part, $n(\omega)$, is the refractive index second-order tensor, whereas the other part, $k(\omega)$, is the extinction tensor, which represents the loss of photon energy during propagation through the optical medium. The premeditated refractive indices for $\text{KPdCu}(\text{Se}_2)(\text{Se}_3)$ and $\text{RbPdCu}(\text{Se}_2)(\text{Se}_3)$ are illustrated in Fig. 6a and b. The calculated non-zero tensor components of the static refractive index $n^{xx}(0)$, $n^{yy}(0)$ and $n^{zz}(0)$ are 2.483, 2.498 and 2.479 for $\text{KPdCu}(\text{Se}_2)(\text{Se}_3)$ and 2.430, 2.448 and 2.391 for $\text{RbPdCu}(\text{Se}_2)(\text{Se}_3)$, respectively. According to Penn's model,³⁶ $\varepsilon_1(0)$ relates to the band gap of the material and $\varepsilon_1(0)$ is directly related to $n(0)$ by the relation $n(\omega) = \sqrt{\varepsilon_1(\omega)}$. They are improved beyond the zero frequency limits, reaching their maximum values. After the maximum values they start to decrease and, with few oscillations, are greater than unity. In this region ($n < 1$) the phase velocity of the photons enhances, approaching the universal constant (C). In contrast, the group velocity is always less than C and, as a consequence, the relativity relations are not affected.³⁷ The spectrum moves towards lower energy when the cations are changed from K to Rb. This is in agreement with the decrease in the band gap. The absorption spectra of $\text{KPdCu}(\text{Se}_2)(\text{Se}_3)$ and $\text{RbPdCu}(\text{Se}_2)(\text{Se}_3)$ (Fig. 6c and d) shows that both these materials absorb radiation at 2.0 eV. The absorption spectra show an uppermost value of 13.6 eV, analogous to the minimum values of $\varepsilon_1(\omega)$ and $\varepsilon_2(\omega)$ shown in Fig. 5a–d.

The frequency dependent reflectivities $R^{xx}(\omega)$, $R^{yy}(\omega)$ and $R^{zz}(\omega)$ were calculated and are shown in Fig. 6e and f. The reflectivity spectra of the compounds originates from the zero energy which characterizes the static part of the reflectivity components $R^{zz}(0)$, $R^{yy}(0)$ and $R^{xx}(0)$. These values are equal to 0.173, 0.176 and 0.168 for $\text{KPdCu}(\text{Se}_2)(\text{Se}_3)$ and 0.181, 0.183 and 0.180 for $\text{RbPdCu}(\text{Se}_2)(\text{Se}_3)$. The energy loss function $L^{xx}(\omega)$, $L^{yy}(\omega)$ and $L^{zz}(\omega)$, as illustrated in Fig. 6g and h, is a key component in the evaluation of the usefulness of energy of the material due to very fast electrons. The sharp spectral peaks produced in $L^{xx}(\omega)$, $L^{yy}(\omega)$ and $L^{zz}(\omega)$ around 11.8 eV for $\text{KPdCu}(\text{Se}_2)(\text{Se}_3)$ and at 12.0 eV for $\text{RbPdCu}(\text{Se}_2)(\text{Se}_3)$ are due to the occurrence of plasmon excitations.³⁸ It is observed that the relative maximum in the energy loss function occurs with a good approximation at energies where the dielectric function $\varepsilon_1(\omega)$ crosses the zero.

3.5. Thermal properties

The main aim of this work was to determine the thermoelectric properties of $\text{APdCu}(\text{Se}_2)(\text{Se}_3)$ ($A = \text{K}$ and Rb) and their variation with temperature. It is essential to guesstimate the effective

masses of the carriers in different electron and hole pockets to achieve this. We calculated the effective mass (electron, heavy hole and light hole) ratio of the carriers at the conduction and valence band edges by fitting the energy of the respective bands to a quadratic polynomial in the reciprocal lattice vector \vec{k} as discussed earlier. It is apparent that the bands are less dispersive in the $\text{KPdCu}(\text{Se}_2)(\text{Se}_3)$ structure in almost all the high symmetry directions. This is why we aimed for a large effective mass to obtain a high thermo-power. The existence of high mobility carriers is essential in attaining a higher electrical conductivity. Thus there is an opportunity to gain a large figure of merit (ZT) factor in these compounds by having multiple pockets of carriers with both large and small effective masses, with the former leading to a large Seebeck coefficient (S) and the latter improving $\sigma(\tau)$.^{39,40} It is encouraging to note that the electronic structure of the investigated compounds shows the existence of multiple carrier pockets with significantly dissimilar effective masses, thereby signifying that they may have good thermoelectric properties.

For the conductivity coefficient calculation, the relaxation time term τ should be treated as a constant. Fig. 7a and b show the calculated temperature-dependent electrical conductivities for the studied compounds as a function of the relaxation time, $\sigma(\tau)$, within the temperature range 300–800 K, which is given as the σ^{xx} , σ^{yy} and σ^{zz} components. It was found that the conductivity as a function of relaxation time is anisotropic. Assuming that the relaxation time τ is direction-independent, the values of the σ^{xx} and σ^{zz} components at 800 K are smaller than the value of the σ^{yy} component.

The σ^{xx} , σ^{yy} and σ^{zz} values increase rapidly with increasing temperature, confirming the semiconductor-like transportation and temperature-sensitive conduction; this is in good agreement with the calculated electronic band structure. The anisotropic nature should be enhanced at higher temperatures, as shown in Fig. 7a and b. Although there is anisotropy in σ^{xx} , σ^{yy} and σ^{zz} at 300 K, this anisotropy is much greater at higher temperatures. The maximum conductivity values as a function of relaxation time reach $6 \times 10^{18} \Omega^{-1} \text{m}^{-1} \text{s}^{-1}$, $1.72 \times 10^{18} \Omega^{-1} \text{m}^{-1} \text{s}^{-1}$ and $4.8 \times 10^{18} \Omega^{-1} \text{m}^{-1} \text{s}^{-1}$ within the σ^{xx} , σ^{yy} and σ^{zz} components, respectively, for $\text{KPdCu}(\text{Se}_2)(\text{Se}_3)$. In the $\text{KPdCu}(\text{Se}_2)(\text{Se}_3)$ compound the σ^{xx} and σ^{zz} components show weak anisotropy with increasing temperature up to 550 K; the anisotropy then increases with increasing temperature. The anisotropy between the σ^{xx} and σ^{zz} components is comparatively much smaller than that of σ^{xx} and σ^{zz} with the σ^{yy} component. As K is replaced by Rb, the conductivity in both compounds increases with increasing temperature. In $\text{RbPdCu}(\text{Se}_2)(\text{Se}_3)$ there is isotropy between the σ^{xx} and σ^{zz} components over the whole temperature range, although the σ^{xx} and σ^{zz} components show considerable anisotropy with the σ^{yy} component. The maximum conductivity values for $\text{RbPdCu}(\text{Se}_2)(\text{Se}_3)$ as a function of relaxation time reach $0.5 \times 10^{18} \Omega^{-1} \text{m}^{-1} \text{s}^{-1}$ for the σ^{xx} and σ^{zz} components and about $6.85 \times 10^{18} \Omega^{-1} \text{m}^{-1} \text{s}^{-1}$ for the σ^{yy} component. From the conductivity spectra of both compounds we concluded that $\text{KPdCu}(\text{Se}_2)(\text{Se}_3)$ shows a greater increase in conductivity than $\text{RbPdCu}(\text{Se}_2)(\text{Se}_3)$.

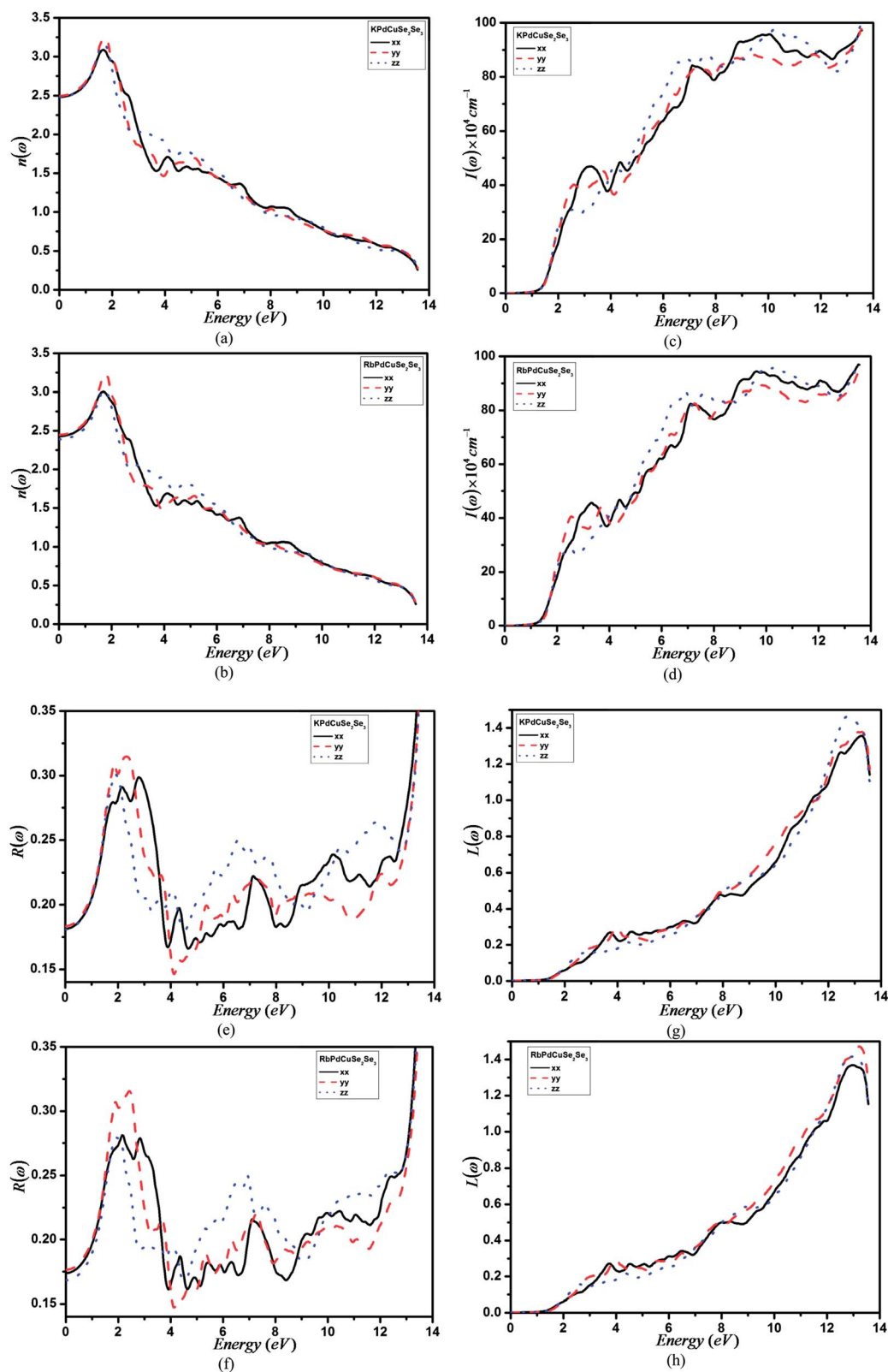


Fig. 6 Calculated refractivity $n(\omega)$, absorption coefficient $I(\omega)$, reflectivity $R(\omega)$ and energy-loss function spectrum $L(\omega)$.

Fig. 7c and d present the calculated temperature-dependent Seebeck coefficients, denoted as the S^{xx} , S^{yy} and S^{zz} components, for the APdCu(Se_2)(Se_3) (A = K and Rb) compounds in the

temperature range 300–800 K. It was found that the Seebeck coefficient as a function of temperature is also anisotropic; the S^{xx} , S^{yy} and S^{zz} components show reverse behaviors with respect

Paper

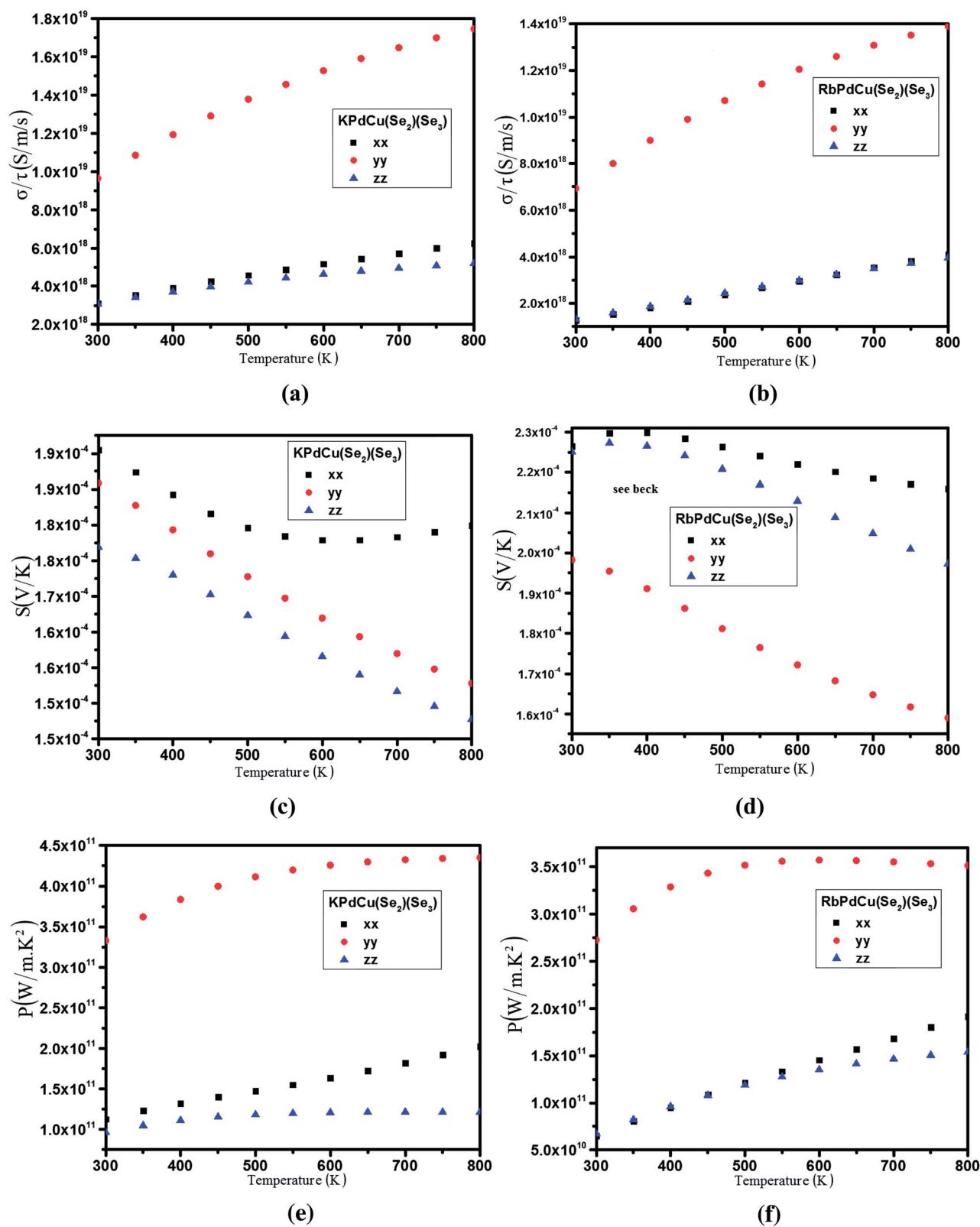


Fig. 7 Calculated thermoelectric properties: electrical conductivity, Seebeck coefficients and power factor.

to the conductivity as a function of temperature. For example, the S value within ' S^y ' component is larger than that within the S^{xx} and S^{zz} components and the anisotropic nature remains the

same in the higher temperature region. The values of the S^{xx} , S^y and S^{zz} components show positive temperature dependence. It was also observed that the values of S^{xx} , S^y and S^{zz} tends to be

completely saturated in the high temperature region, reaching $1.83 (2.16) \times 10^{-4}$, $1.57 (1.97) \times 10^{-4}$ and $1.55 (1.59) \times 10^{-4}$ for the S^{xx} , S^{yy} and S^{zz} components, respectively, for $\text{KPdCu}(\text{Se}_2)(\text{Se}_3)$ and $\text{RbPdCu}(\text{Se}_2)(\text{Se}_3)$ at 800 K. From a consideration of the conductivity dependence as a function of temperature, the electrical performance should be enhanced with increasing temperature.

As we replace K by Rb, the decrease in the Seebeck coefficient for both compounds is the same with increasing temperature. The three components show considerable anisotropy with increasing temperature in both compounds. If we look at the spectra, with increasing temperature the S^{xx} , S^{yy} and S^{zz} components decrease, but the S^{xx} component shows a different behavior to the S^{yy} and S^{zz} components. The S^{xx} component decreases to 600 K, is at equilibrium at 650 K, and then starts to increase with increasing temperature. At low temperatures, $\text{RbPdCu}(\text{Se}_2)(\text{Se}_3)$ has a larger Seebeck coefficient than $\text{KPdCu}(\text{Se}_2)(\text{Se}_3)$.

Fig. 7e and f show the calculated temperature-dependent power factor (PF) as a function of relaxation time in the temperature interval 300–800 K, denoted as P^{xx} , P^{yy} and P^{zz} . The PF value within the P^{xx} and P^{zz} components at 800 K is smaller than the value of the P^{yy} component, assuming that the relaxation time τ is independent of direction. The PF values increase rapidly with increasing temperature, confirming that the electrical performance is sensitive to temperature. The anisotropic nature is enhanced at higher temperatures (Fig. 7e and f). In $\text{KPdCu}(\text{Se}_2)(\text{Se}_3)$ the P^{xx} and P^{zz} components show weak anisotropy at low temperatures, but the anisotropy increases with increasing temperature; the anisotropy between these two components is comparatively very much smaller than that along the P^{yy} component. In contrast, in $\text{RbPdCu}(\text{Se}_2)(\text{Se}_3)$ the P^{xx} and P^{zz} components show isotropy up to 550 K, which increases with increasing temperature; both the P^{xx} and P^{zz} components show considerable anisotropy with the P^{yy} component. We emphasize that $\text{KPdCu}(\text{Se}_2)(\text{Se}_3)$ shows a greater PF value than $\text{KPdCu}(\text{Se}_2)(\text{Se}_3)$. The maximum PF values as a function of relaxation time are $4.3 (3.5) \times 10^{11}$, $2.0 (1.57) \times 10^{11}$ and $1.2 (1.5) \times 10^{11} \text{ W m}^{-1} \text{ K}^{-2} \text{ s}^{-1}$ for the P^{xx} , P^{yy} and P^{zz} components, respectively, for $\text{KPdCu}(\text{Se}_2)(\text{Se}_3)$ and $\text{RbPdCu}(\text{Se}_2)(\text{Se}_3)$. From the analysis of both compounds, we concluded that they both possess good thermoelectric properties at high temperatures, but that $\text{KPdCu}(\text{Se}_2)(\text{Se}_3)$ shows much better thermoelectric behavior than $\text{RbPdCu}(\text{Se}_2)(\text{Se}_3)$; this is attributed to the fact that at higher temperatures $\text{KPdCu}(\text{Se}_2)(\text{Se}_3)$ shows a better PF value than $\text{RbPdCu}(\text{Se}_2)(\text{Se}_3)$.

4. Conclusions

In summary, the electronic band structure, optical properties and electrical transport coefficients of $\text{APdCu}(\text{Se}_2)(\text{Se}_3)$ ($A = \text{K}$ and Rb), a new quaternary copper palladium polyselenide, were studied. From this study of the electronic band structure, we concluded that the valence band maximum and conduction band minimum are positioned at the Y point, resulting in a direct energy band gap of about 1.258/1.275 eV. From the PDOS we also concluded that at an energy of -5.0 eV, the Pd-s state

strongly hybridizes with the Se-p state. Near the Fermi level, the Se-p state hybridizes with the Cu-p state, and at the low conduction band the Pd-s state forms a strong hybridization with the Cu-s state. We have also calculated the electronic charge density in the (010) plane. It can be seen that the Pd–Se and Cu–Se atoms form weak covalent bonds and strong ionicity, whereas the K/Pd atoms show pure ionic bonding. We have also calculated the effective mass ratio of the electrons, heavy holes and light holes. The calculated effective mass ratio for the electron, heavy holes and light holes for $\text{KPdCu}(\text{Se}_2)(\text{Se}_3)/\text{RbPdCu}(\text{Se}_2)(\text{Se}_3)$ are 0.0332/(0.0225), 0.1350/(0.0202) and 0.1858/(0.0198), respectively. The real and imaginary parts of the dielectric function and hence the optical constants, such as the refractive index and extinction coefficient, were calculated and discussed in detail. From the absorption spectrum we concluded that both $\text{KPdCu}(\text{Se}_2)(\text{Se}_3)$ and $\text{RbPdCu}(\text{Se}_2)(\text{Se}_3)$ begin to absorb radiation at around 1.8–2.0 eV. The absorption spectra show an uppermost value at 13.6 eV, analogous to the minimum value of $\varepsilon_1(\omega)$ and $\varepsilon_2(\omega)$. The Seebeck coefficient, together with the conductivity and the PF as a function of relaxation time were calculated systematically. The calculated conductivity and Seebeck coefficient confirm the anisotropic nature and the semiconductor transport behavior of the compounds. The calculated PF as a function of relaxation time increases rapidly with increasing temperature. The maximum PF values as a function of relaxation time reach $4.3 (3.5) \times 10^{11}$, $2.0 (1.57) \times 10^{11}$ and $1.2 (1.5) \times 10^{11} \text{ W m}^{-1} \text{ K}^{-2} \text{ s}^{-1}$ for the P^{xx} , P^{yy} and P^{zz} components, respectively, for $\text{KPdCu}(\text{Se}_2)(\text{Se}_3)$ and $\text{RbPdCu}(\text{Se}_2)(\text{Se}_3)$ at 800 K. The present calculation of the thermoelectrical behavior of $\text{APdCu}(\text{Se}_2)(\text{Se}_3)$ ($A = \text{K}$ and Rb) for the PF suggests that both compounds show good thermoelectric properties at high temperatures.

Acknowledgements

The work was developed within the CENTEM Project, Reg. no. CZ.1.05/2.1.00/03.0088, co-funded by the ERDF as part of the Ministry of Education, Youth and Sports OP RDI Programme.

References

- (a) H. Eckert, *Angew. Chem., Int. Ed. Engl.*, 1989, **28**, 1723; (b) Y. Wang, N. Herron, W. Mahler and A. Suna, *J. Opt. Soc. Am. B*, 1989, **6**, 808; (c) R. Chung, T. Hogan, P. Brazis, M. Rocci-Lane, C. Kannewurf, M. Bastea, C. Uher and M. G. Kanatzidis, *Science*, 2000, **287**, 1024.
- W. S. Sheldrick and M. Wachhold, *Coord. Chem. Rev.*, 1998, **176**, 211.
- M. G. Kanatzidis and A. C. Sutorik, *Prog. Inorg. Chem.*, 1995, **43**, 15.
- M. G. Kanatzidis, *Curr. Opin. Solid State Mater. Sci.*, 1997, **2**, 139.
- M. G. Kanatzidis and B. K. Das, *Comments Inorg. Chem.*, 1999, **21**, 29.
- W. S. Sheldrick and M. Wachhold, *Angew. Chem., Int. Ed. Engl.*, 1997, **36**, 206.
- G. Kräuter and K. Dehnicke, *Chem.-Ztg.*, 1990, **114**, 7–9.

Paper

- 8 K.-W. Kim and M. G. Kanatzidis, *J. Am. Chem. Soc.*, 1998, **120**, 8124–8135.
- 9 M. Wachhold and M. G. Kanatzidis, *J. Am. Chem. Soc.*, 1999, **121**, 4189–4195.
- 10 K.-W. Kim and M. G. Kanatzidis, *J. Am. Chem. Soc.*, 1992, **114**, 4878.
- 11 J. Li, Z. Chen, R.-J. Wang and J. Y. J. Lu, *Solid State Chem.*, 1998, **140**, 149.
- 12 J. Llanos, C. Contreras-Ortega, C. Mujica, H. G. von Schnering and K. Peters, *Mater. Res. Bull.*, 1993, **28**, 39–44.
- 13 C. Mujica, J. Paez and J. Llanos, *Mater. Res. Bull.*, 1994, **29**, 263–268.
- 14 J. Li, H.-Y. Guo, R. A. Yglesias and T. Emge, *Chem. Mater.*, 1995, **7**, 599–601.
- 15 J. Llanos, C. Contreras-Ortega, J. Paez, M. Guzman and C. Mujica, *J. Alloys Compd.*, 1993, **201**, 103–104.
- 16 J. Llanos, P. Valenzuela, C. Mujica, A. Buljan and R. Ramirez, *J. Solid State Chem.*, 1996, **122**, 31–35.
- 17 X. Chen, K. J. Dilks, X. Huang and J. Li, *Inorg. Chem.*, 2003, **42**, 3723–3727.
- 18 P. Guss, M. E. Foster, B. M. Wong, F. Patrick Doty, K. Shah, M. R. Squillante, U. Shirwadkar, R. Hawrami, J. Tower and D. Yuan, *J. Appl. Phys.*, 2014, **115**, 034908.
- 19 V. I. Anisimov, F. Aryasetiawan and A. I. Lichtenstein, *J. Phys.: Condens. Matter*, 1997, **9**, 767.
- 20 J. P. Perdew, B. Kieron and E. Matthias, *Phys. Rev. Lett.*, 1996, **77**, 3865–3868.
- 21 P. Hohenberg and W. Kohn, *Phys. Rev. B: Condens. Matter Mater. Phys.*, 1996, **136**, B864.
- 22 W. Kohn and L. J. Shom, *Phys. Rev.*, 1965, **140**, A1133.
- 23 P. Blaha, K. Schwarz and J. Luitz, *WIEN97: A full potential linearized augmented plane wave package for calculating crystal properties*, ISBN: 3-9501031-0-4, Karlheinz Schwarz. Techn. Universit at Wien, Austria, 1991.
- 24 C. Loschen, J. Carrasco, K. M. Neyman and F. Illas, *Phys. Rev. B: Condens. Matter Mater. Phys.*, 2007, **75**, 035115.
- 25 J. C. Li, C. L. Wang, M. X. Wang, H. Peng, R. Z. Zhang, M. L. Zhao, J. Liu, J. L. Zhang and L. M. Mei, *J. Appl. Phys.*, 2009, **105**, 043503.
- 26 A. Popescu, L. M. Woods, J. Martin and G. S. Nolas, *Phys. Rev. B: Condens. Matter Mater. Phys.*, 2009, **79**, 205302.
- 27 M. Zebarjadi, K. Esfarjani, M. S. Dresselhaus, Z. F. Ren and G. Chen, *Energy Environ. Sci.*, 2012, **5**, 5147.
- 28 L. Bertini and C. Gatti, *J. Chem. Phys.*, 2004, **121**, 8983.
- 29 Y. Wang, X. Chen, T. Cui, Y. Niu, Y. Wang, M. Wang, Y. Ma and G. Zou, *Phys. Rev. B: Condens. Matter Mater. Phys.*, 2007, **76**, 155127.
- 30 L. Lykke, B. B. Iversen and G. K. H. Madsen, *Phys. Rev. B: Condens. Matter Mater. Phys.*, 2007, **73**, 195121.
- 31 D. B. Sirdeshmukh, L. Sirdeshmukh and K. G. Subhadra, *Alkali Halides: A Handbook of Physical Properties*, ed. R. Hull, R. M. Osgood Jr, H. Sakaki and A. Zunger, Springer-Verlag, Berlin, 2001, pp. 249, 251.
- 32 G. K. H. Madsen and D. J. Singh, *Comput. Phys. Commun.*, 2006, **175**, 67.
- 33 R. C. Fang, *Spectroscopy of Solid*, University of Science and Technology Press, Hefei, China, 2001, pp. 71–75.
- 34 X. C. Sheng, *Spectrum and Optical Property of Semiconductor*, Science Press, Beijing, 2002, pp. 76–94.
- 35 Q. Chen, Q. Xie and W. J. Yan, *Sci. China, Ser. G: Phys., Mech. Astron.*, 2008, **38**(7), 825–833.
- 36 D. R. Penn, *Phys. Rev. B: Solid State*, 1962, **128**, 2093–2097.
- 37 M. Fox, *Optical Properties of Solids*, Oxford University Press, 2001.
- 38 L. Marton, *Rev. Mod. Phys.*, 1956, **28**, 172–184.
- 39 D. Parker and D. J. Singh, *Phys. Rev. B: Condens. Matter Mater. Phys.*, 2012, **85**, 125209.
- 40 D. J. Singh and I. I. Mazin, *Phys. Rev. B: Condens. Matter Mater. Phys.*, 1997, **56**, R1650–R1653.



Contents lists available at ScienceDirect

Journal of Alloys and Compounds

journal homepage: www.elsevier.com/locate/jalcom

Optoelectronic behavior of Quaternary Uranium Chalcogenides $\text{Rb}_2\text{Pd}_3\text{UM}_6$ ($\text{M} = \text{S}, \text{Se}$): A first principle study

Haleem Ud Din ^a, Sikander Azam ^b, Saleem Ayaz Khan ^b, R. Khenata ^{c,*}^a Department of Physics, Hazara University, Mansehra, Pakistan^b New Technologies – Research Center, University of West Bohemia, Univerzitni 8, 306 14 Pilsen, Czech Republic^c Laboratoire de Physique Quantique et de Modélisation Mathématique (LPQ3M), Département de Technologie, Université de Mascara, Mascara 29000, Algeria

ARTICLE INFO

Article history:

Received 11 April 2014

Received in revised form 27 June 2014

Accepted 27 June 2014

Available online 5 July 2014

Keywords:

Metallic

Electronic structure

Ab-initio calculation

ABSTRACT

First principle calculations of electronic, Fermi surface, electronic charge density and optical properties of Quaternary Uranium Chalcogenides $\text{Rb}_2\text{Pd}_3\text{UM}_6$ ($\text{M} = \text{S}, \text{Se}$) are performed using full potential linear augmented plane wave (FP-LAPW) method within the frame work of density functional theory. Using mBJ method, the electronic band curves overlap at Fermi level and show metallic band structure for both compounds. The calculated densities of states (DOS) spectra show that the valence band is mainly attributed to Rb-p, Pd-d and S-s/p or Se-s/p states; conduction band is mainly attributed to Pd-d, U-f and S-p or Se-p/d states. From the electronic charge density spectrum, it is revealed that a strong covalent bond exists between Pd and S, and Pd or Se while charge transfer between U and S, U and Se, Rb and S, and Rb and Se atoms results in ionic bond nature. It is noted from Fermi surface calculations that both compounds comprise same number of fast velocity electrons but differs in slow or intermediate velocity of electrons. The calculated frequency dependent dielectric function, energy loss function and reflectivity show a considerable anisotropy for both compounds.

© 2014 Elsevier B.V. All rights reserved.

1. Introduction

Recently Quaternary Uranium Chalcogenides compounds like $\text{Rb}_2\text{Pd}_3\text{UM}_6$ ($\text{M} = \text{S}, \text{Se}$) containing both a transition and an actinide metal have been studied due to their important magnetic properties, U–U interatomic distances dependence and Uranium coordination environment [1]. The U–U interatomic distances affect whether long-range magnetic ordering occurs, whereas the crystalline electric field effect is produced by the coordination number [2]. Moreover, the interaction between f-orbital electrons of Uranium (U) and the valence orbitals of the Palladium (Pd) complicates the magnetic behavior and results in orbital overlapping as in proximity in intermetallic compounds. An anion such as Sulfur (S) or Selenium (Se) can be incorporated to make these magnetic atoms far apart and reduces the orbital overlapping. Additionally, the oxidation states are assigned to the atoms and the atoms adopt characteristic coordination environments that are not present in intermetallic compounds. $\text{Rb}_2\text{Pd}_3\text{US}_6$ shows unusual low magnetic moment to crystalline electric field effect and noticeable magnetic

anisotropy. These quaternary compounds crystallize in orthorhombic structure with space group of $Fmmm$ and have eight formula units in the $\text{NaBa}_2\text{Cu}_3\text{O}_6$ structure type. Pd atoms occupy the square-planar coordination environment. A hexagonal prism structure can be formed by six edge-sharing square-planar PdM_6 ($\text{M} = \text{S}, \text{Se}$) units and also the edges shared with trigonal-prismatic UM_6 units, forming layers along (010). Rb atoms separate these layers. The Rb1 atom occurs in a square antiprism while Rb2 atom is ten coordinate with one hexagonal face and the opposite face square [1].

To the best of our knowledge, neither experimental nor theoretical data related electronic structure, Fermi surface, electronic charge density and optical properties of $\text{Rb}_2\text{Pd}_3\text{UM}_6$ ($\text{M} = \text{S}, \text{Se}$) compounds are available. Thus, we think worthwhile to perform these calculations, using the full potential linear augmented plane wave (FP-LAPW) method.

The rest of the paper is as follows, Section 2 deals with the brief description of the computational detail of this study. The most relevant results obtained for the electronic band structure, density of states (DOS), electronic charge density, Fermi surface and optical properties of $\text{Rb}_2\text{Pd}_3\text{UM}_6$ ($\text{M} = \text{S}, \text{Se}$) compounds have been presented and discussed in detail in Section 3. Finally, in Section 4 we summarize the main conclusions of our work.

* Corresponding author. Address: LPQ3M-Laboratory, Faculty of Science and Technology, Mascara University, Mascara 29000, Algeria. Fax: +213 45802923.

E-mail address: khenata_rabah@yahoo.fr (R. Khenata).

2. Method of calculation

As $\text{Rb}_2\text{Pd}_3\text{UM}_6$ ($M = \text{S}, \text{Se}$) compounds have been reported in the $Fmmm$ space group of the orthorhombic system with crystal structure as shown in Fig. 1a and b. The experimental lattice constants recently reported by Oh George et al. [1]; $a = 9.7462(2) \text{ \AA}$, $b = 14.3306(2) \text{ \AA}$, $c = 16.8572(3) \text{ \AA}$ for $\text{Rb}_2\text{Pd}_3\text{US}_6$ and $a = 10.0525(3) \text{ \AA}$, $b = 14.8432(5) \text{ \AA}$, $c = 17.4127(5) \text{ \AA}$ for $\text{Rb}_2\text{Pd}_3\text{USE}_6$, are used in our calculation. The present optimized atomic positions and optimized interatomic distances (\AA) for $\text{Rb}_2\text{Pd}_3\text{UM}_6$ ($M = \text{S}, \text{Se}$) compounds are in good agreement with available experimental data [1] as given in Tables 1 and 2, respectively. We have performed these calculations using full potential linear augmented plane wave (FP-LAPW) method within the support of density functional theory (DFT) [3,4] as implemented in WIEN2 K code [5]. Achievement of DFT is to use different approximations like local density approximation (LDA), generalized gradient approximation (GGA), Engel-Vosko generalized gradient approximation (EV-GGA) and modified Becke-Johnson (mBJ), to treat the exchange correlation [6–9]. As the DFT within both LDA and GGA is known to usually underestimates the band gap value, hence the modified Becke Johnson (mBJ) is used to remove this discrepancy and to obtain a reliable electronic and optical properties for $\text{Rb}_2\text{Pd}_3\text{UM}_6$ ($M = \text{S}, \text{Se}$) compounds. It has been observed that mBJ produces band gap values closer to the experimental data compared to those obtained with LDA, GGA or EV-GGA [9–16].

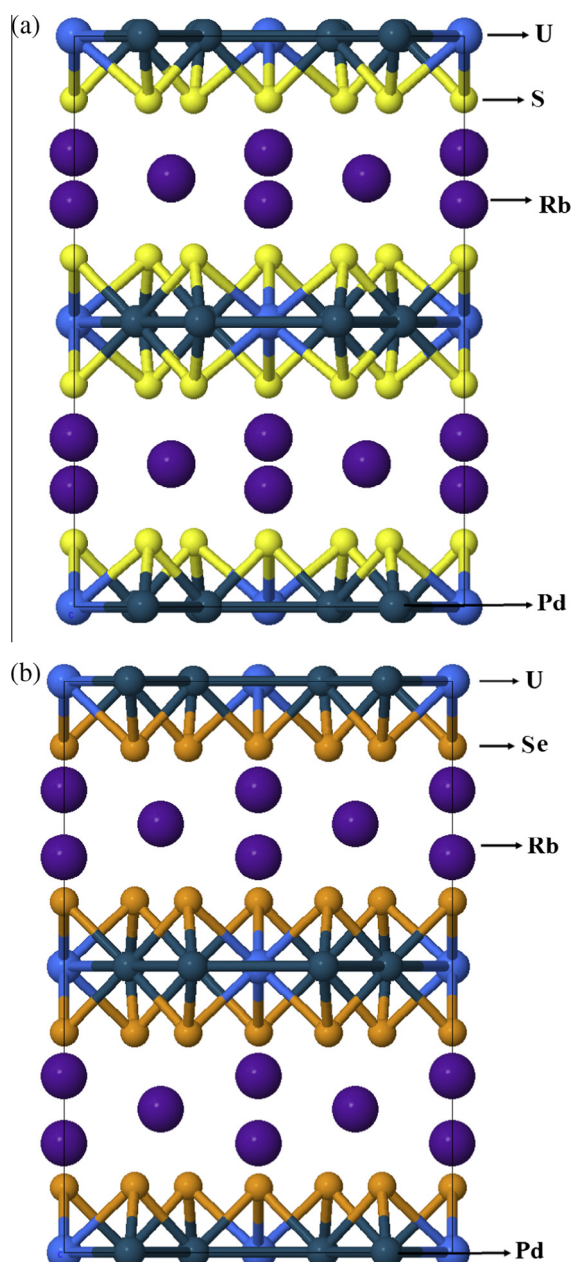


Fig. 1. Crystal structure of $\text{Rb}_2\text{Pd}_3\text{US}_6$ (a) and $\text{Rb}_2\text{Pd}_3\text{USE}_6$ (b).

In the interstitial region, the wave function was expanded in plane wave with cut-off, $R_{\text{MT}}K_{\text{max}} = 7.0$ whereas, it was expanded up to $l_{\text{max}} = 10$ in the sphere. The R_{MT} values were chosen as 2.0 atomic units (a.u.) for all (Rb, Pd, U, S and Se) atoms. A mesh of $10 \times 10 \times 10$ k -points was used in the irreducible Brillouin zone integration. Also, the Fourier expansion of charge density was taken to be $G_{\text{max}} = 12$ (a.u.) $^{-1}$. The self consistency was used to check the electronic structure, Fermi surface, electronic charge density and optical properties convergence in the self consistency field.

3. Results and discussions

3.1. Band structure, density of states (DOS) and electronic charge density

The electronic properties such as band structure and density of states (DOS) of $\text{Rb}_2\text{Pd}_3\text{UM}_6$ ($M = \text{S}, \text{Se}$) compounds are calculated using mBJ. The calculated band structure for $\text{Rb}_2\text{Pd}_3\text{US}_6$ and $\text{Rb}_2\text{Pd}_3\text{USE}_6$ are shown in Fig. 2a and b, respectively. It is noted there is no energy gap among the bands around the Fermi level. At the Fermi level valence and conduction bands overlap significantly, as a result, both $\text{Rb}_2\text{Pd}_3\text{US}_6$ and $\text{Rb}_2\text{Pd}_3\text{USE}_6$ exhibit a metallic character.

The total and partial density of states (TDOS and PDOS) for $\text{Rb}_2\text{Pd}_3\text{UM}_6$ ($M = \text{S}, \text{Se}$) compounds are also calculated and displayed in Fig. 3a–c. It is clear from the densities of states spectra that the valence band (VB) below the Fermi level consists of three regions. For both compounds, the lower part of valence band situated between -14.0 eV and -12.0 eV is mainly contributed by S-s or Se-s orbitals with small contribution of Pd-s/p and U-s/p and Rb-s orbitals, while the second lower region from -11.8 eV to -10.5 eV is dominated by Rb-p orbital. The third region of valence band from -6.0 eV to -1.0 eV is attributed to Pd-d state with small contribution of S-p state. The conduction band (CB) in these compounds originates from Pd-d, U-f and S-p or Se-p states with a small contribution of Rb-s, Pd-p and U-d orbital electrons. Therefore, VB is mainly attributed to Rb-p, Pd-d and S-s/p or Se-s/p states; CB is mainly attributed to Pd-d, U-f and S-p or Se-p/d states and there exist a strong hybridization between Pd-d, U-f and S-p or Se-p/d orbitals.

Electronic charge density is used to provide information about the bond nature among different atoms. The electron charge density plots for $\text{Rb}_2\text{Pd}_3\text{UM}_6$ ($M = \text{S}, \text{Se}$) compounds in 2D (101) plane have been calculated using mBJ and displayed in Fig. 4. As large difference in electronegativity (EN) is responsible for charge transfer among different atoms resulting ionic bond nature. Small electronegativity difference (EN) results in charge sharing and responsible for covalent bond nature. Electronegativity values for Rb, Pd, U, S and Se are 0.82, 2.20, 1.38, 2.58 and 2.55, respectively. Small ΔEN values show strong covalent bond nature of Pd with S or Se while large electronegativity difference between U and S, U and Se, Rb and S, and Rb and Se result in ionic bond nature. Different colors in color charge density scale correspond to different charge concentration areas. The blue color represents maximum charge transfer. From the electron charge density contours it can be noted that maximum charge sharing between Pd and $M = \text{S}, \text{Se}$ is seen and hence, confirms the covalent bond nature.

3.2. Fermi surface

The electronic structure of metallic materials can be well described by the electronic states which cross the Fermi level and form the Fermi surface (FS) structure. Energy distribution curves (EDC) for k -points of the Brillouin zone is used conventionally to determine the Fermi surface and the k -locations (i.e. the bands crossing the Fermi energy). Electrons closest to the Fermi level play a vital role for conductivity of a material. Hence, it is easy to understand the electronic structure of any metallic material

Table 1
Comparison between experimental and optimized atomic positions for $Rb_2Pd_3UM_6$ ($M = S, Se$) compounds.

Atom	Exp. X	Opt. X	Exp. Y	Opt. Y	Exp. Z	Opt. Z
<i>Rb₂Pd₃US₆</i>						
U1	0.0000	0.0000	0.0000	0.0000	0.167539(9)	0.16786
Pd1	0.33937(2)	0.33741	0.0000	0.0000	0.157018(15)	0.15805
Pd2	0.17687(3)	0.17446	0.0000	0.0000	0.0000 0	0.0000
Rb1	0.2500	0.2500	0.2500	0.2500	0.2500	0.2500
Rb2	0.0000	0.0000	0.29578(4)	0.29962	0.0000	0.0000
S1	0.19234(6)	0.18171	0.11234(4)	0.11247	0.10041(3)	0.10299
S2	0.0000	0.0000	0.11126(5)	0.11049	0.30034(5)	0.29375
<i>Rb₂Pd₃USe₆</i>						
U1	0.0000	0.0000	0.0000	0.0000	0.167775(18)	0.16837
Pd1	0.33737(4)	0.33448	0.0000	0.0000	0.15796(3)	0.15904
Pd2	0.17316(6)	0.16960	0.0000	0.0000	0.0000	0.0000
Rb1	0.2500	0.2500	0.2500	0.2500	0.2500	0.2500
Rb2	0.0000	0.0000	0.30444(6)	0.30898	0.0000	0.0000
Se1	0.19155(4)	0.18091	0.11523(3)	0.11638	0.09999(3)	0.10236
Se2	0.0000	0.0000	0.11362(4)	0.11392	0.30084(4)	0.29520

Table 2
Comparison between experimental and optimized interatomic distances (Å) for $Rb_2Pd_3UM_6$ ($M = S, Se$) compounds.

<i>Rb₂Pd₃US₆</i>						
Atoms	U1–S1	U1–S2	Pd1–S1.2	Pd1–S2.2	Pd2–S1.4	
Exp.	2.7178(6)	2.7483(8)	2.3473(6)	2.3571(6)	2.3408(6)	
Opt.	2.633	2.648	2.400	2.383	2.370	
Atoms	Rb1–S1.4	Rb1–S2.4	Rb2–S2.2	Rb2–S1.4	Rb2–S1.4	
Exp.	3.2506(6)	3.2573(5)	3.6198(8)	3.6455(7)	3.6864(6)	
Opt.	3.235	3.237	3.708	3.653	3.771	
<i>Rb₂Pd₃USe₆</i>						
Atoms	U1–Se1	U1–Se2	Pd1–Se1.2	Pd1–Se2.2	Pd2–Se1.4	
Exp.	2.8331(5)	2.8659(7)	2.4684(5)	2.4560(5)	2.4477(4)	
Opt.	2.595	2.782	2.518	2.503	2.485	
Atoms	Rb1–Se1.4	Rb1–Se2.4	Rb2–Se2.2	Rb2–Se1.4	Rb2–Se1.4	
Exp.	3.3421(4)	3.3462(4)	3.6750(7)	3.7506(5)	3.8244(8)	
Opt.	3.320	3.319	3.745	3.828	3.833	

from the Fermi surface. We have performed the FS calculations of $Rb_2Pd_3UM_6$ ($M = S, Se$) compounds using FP-LAPW method as displayed in Fig. 5a and b. It can be observed from this figure that the FS for $Rb_2Pd_3UM_6$ ($M = S, Se$) compounds is made up of one band and consists of a number of empty and shaded areas. The empty

and shaded areas contain holes and electrons respectively, show a considerable difference between the FS of these compounds. One can see that $Rb_2Pd_3US_6$ have large number of holes and less number electrons while $Rb_2Pd_3USe_6$ contains less holes and large number of electrons. Additionally, different color seen in the FS, result from the change in velocity of electrons. Violet and red colors represent slow and fast velocity of electrons whereas, the rest of colors show intermediate velocity of electrons. From FS, it is noted that both compounds comprising same number of fast velocity electrons but differs in slow or intermediate velocity of electrons.

3.3. Optical properties

The optoelectronic properties of solid materials are very useful for various applications in sciences and engineering [17]. We have calculated the optical properties of $Rb_2Pd_3UM_6$ ($M = S, Se$) compounds using mBJ as shown in Fig. 6a–d. Neither theoretical nor experimental literature has been found regarding the optical properties of these compounds. The frequency dependent dielectric function and the band structure calculations can be established from energy eigenvalues and electron wave functions. As the

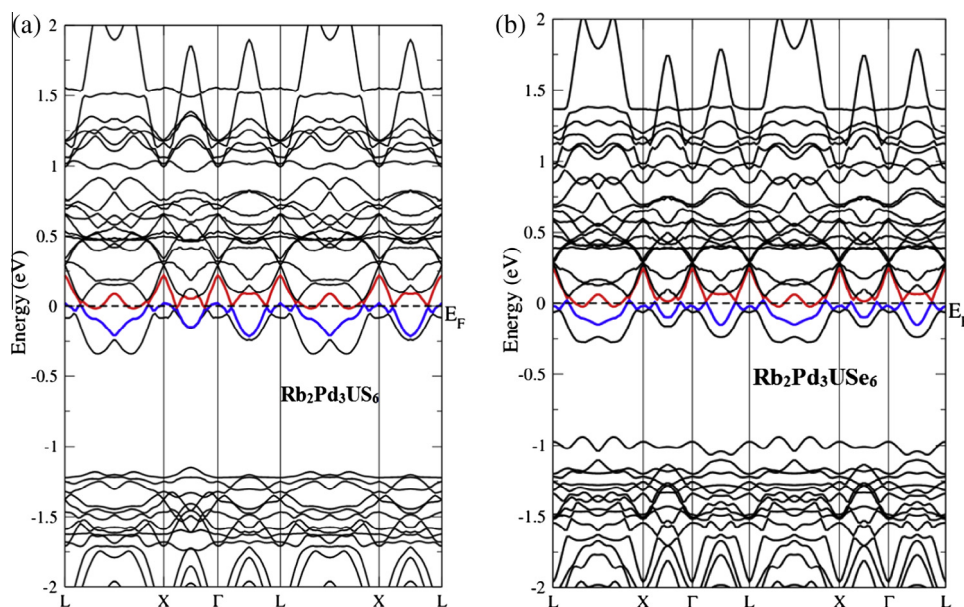


Fig. 2. Calculated band structures of $Rb_2Pd_3US_6$ (a) and $Rb_2Pd_3USe_6$ (b) using mBJ.

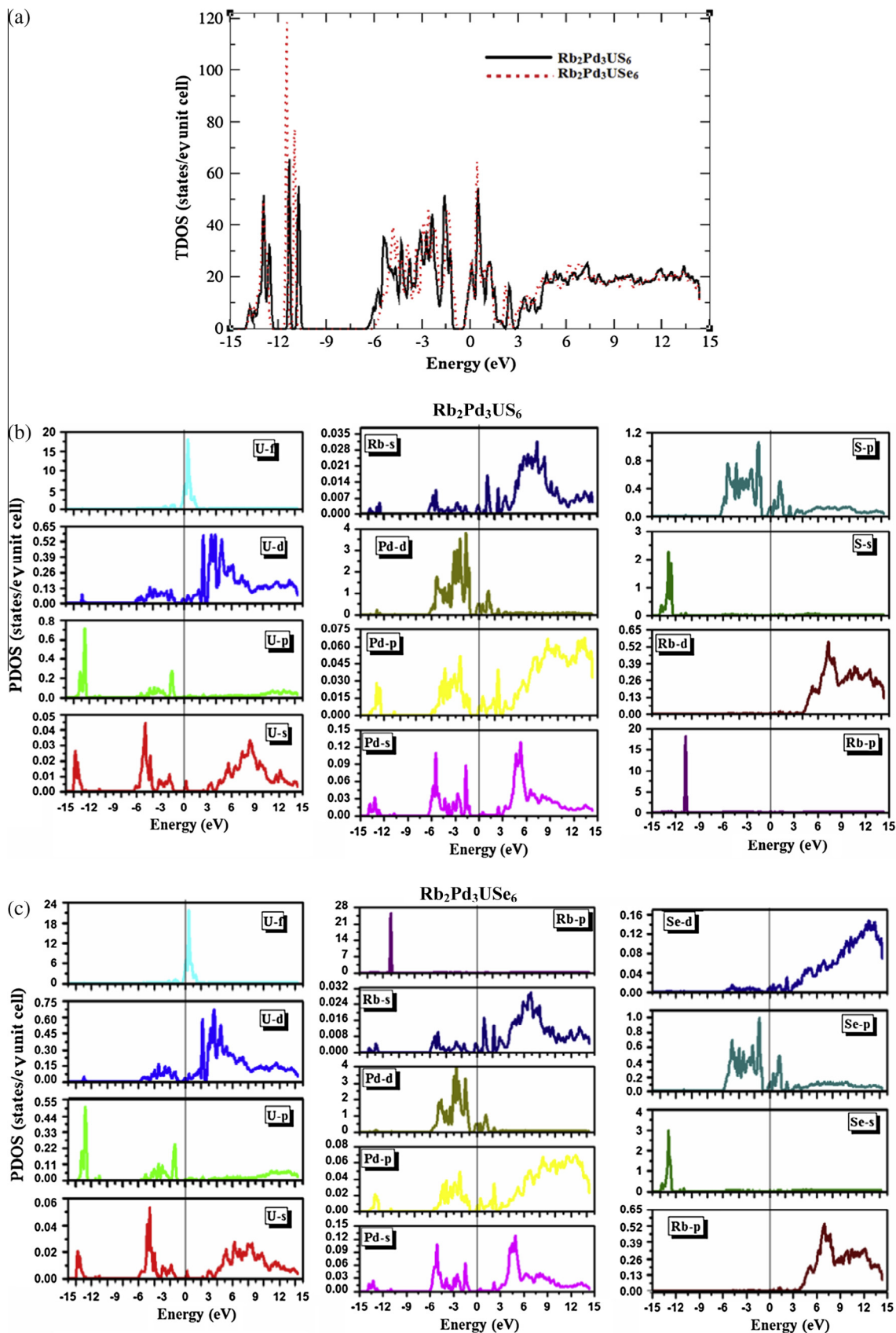


Fig. 3. Calculated total density of states (TDOS) of $\text{Rb}_2\text{Pd}_3\text{US}_6$ and $\text{Rb}_2\text{Pd}_3\text{USE}_6$ (a), partial density of states (PDOS) of $\text{Rb}_2\text{Pd}_3\text{US}_6$ (b) and $\text{Rb}_2\text{Pd}_3\text{USE}_6$ (c) using mBJ.

inter-band transitions are mainly divided into two parts; direct and indirect inter-band transitions. The indirect inter-band transitions are ignored because it leads to phonon scattering and

expected less contribution to $\epsilon_2(\omega)$ [18]. Direct inter-band transition may contribute to $\epsilon_2(\omega)$ if all likely transitions from occupied to unoccupied states are achieved. As $\text{Rb}_2\text{Pd}_3\text{UM}_6$ ($M = \text{S}, \text{Se}$)

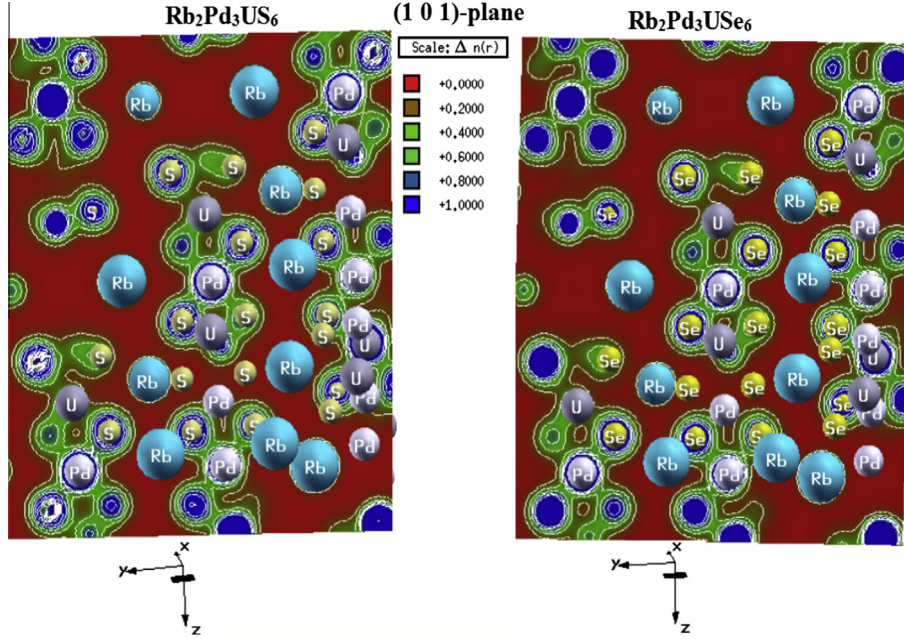


Fig. 4. Calculated electronic charge density of $Rb_2Pd_3UM_6$ ($M = S, Se$) in (101)-plane.

compounds have $Fm\bar{3}m$ space group of the orthorhombic system and therefore, comprising three non-zero components (i.e. $\epsilon^{xx}(\omega)$, $\epsilon^{yy}(\omega)$ and $\epsilon^{zz}(\omega)$) of second order dielectric tensor. The imaginary part of dielectric function $\epsilon_2(\omega)$ [19] can be calculated as:

$$\epsilon_2^{ij}(\omega) = \left(\frac{8\pi^2 \hbar^2 e^2}{m^2 V} \right) \sum_k \sum_{cv} (f_c - f_v) \frac{P_{cv}^i(k) P_{vc}^j(k)}{E_{vc}^2} \delta[E_c(k) - E_v(k) - \hbar\omega] \quad (1)$$

where $P_{cv}^i(k)$, V , e , m , \hbar , f_c and f_v represent the momentum matrix element, unit cell volume, electronic charge, electron mass, Planck's constant and Fermi distributions of the valence and conduction bands, respectively.

Imaginary part of the dielectric function $\epsilon_2(\omega)$ for both compounds in the energy range 0–8 eV is shown in Fig. 6a. It is clear from Fig. 6a that the components $\epsilon_2^{xx}(\omega)$ and $\epsilon_2^{zz}(\omega)$ display maximum anisotropy with $\epsilon_2^{yy}(\omega)$ in the energy range 0–6 eV. This anisotropy corresponds to different polarizations. Peak values of the components $\epsilon_2^{xx}(\omega)$, $\epsilon_2^{yy}(\omega)$ and $\epsilon_2^{zz}(\omega)$ are given in Table 3. For both compounds, the peak value of $\epsilon_2^{yy}(\omega)$ dominates $\epsilon_2^{xx}(\omega)$ and $\epsilon_2^{zz}(\omega)$ and results in transition from the bottom of valence band (VB) to the top of conduction band (CB). Additionally, the maximum absorption seen between 0 and 0.4 eV reveals that these compounds are suitable for optoelectronic devices in the infrared (IR) energy region. A few small bumps are observed at higher energies. Moreover, higher reflection and very small absorption can be noticed between 4.0 eV and 5.3 eV.

A preview of three components $\epsilon_1^{xx}(\omega)$, $\epsilon_1^{yy}(\omega)$ and $\epsilon_1^{zz}(\omega)$ for the real part of the dielectric function obtained from the three components of $\epsilon_2(\omega)$, is displayed in Fig. 6b. Two components $\epsilon_1^{xx}(\omega)$ and $\epsilon_1^{zz}(\omega)$ show major anisotropy with $\epsilon_1^{yy}(\omega)$ and display an anisotropic behavior from 3.5 to 4.6 eV energy range. Above 6.1 eV, all the three components $\epsilon_1^{xx}(\omega)$, $\epsilon_1^{yy}(\omega)$ and $\epsilon_1^{zz}(\omega)$ behave isotropically. Penn model [20–22] relates the real part of the dielectric function and the band gap as, $\epsilon_1(0) = 1 + (\hbar\omega_p/E_g)$. From the spectrum, an inverse relationship between band gap and $\epsilon_1(0)$ has been noted and values of $\epsilon_1^{xx}(0)$, $\epsilon_1^{yy}(0)$ and $\epsilon_1^{zz}(0)$ are given in Table 3.

Added to the dielectric function, the energy-loss function and reflectivity calculations are performed using mBJ. Energy-loss function $L(\omega)$ is large at plasma energy and determines the energy

lost in traversing of a fast moving electron [23,24]. The collective oscillation of valence electron causes plasmon loss. In the inter-band transitions, the scattering probability for volume is directly related to $L(\omega)$. We have calculated the spectrum of frequency related to plasma resonance (as shown in Fig. 6c). For these compounds, the maximum peaks are located above 11.0 eV and can be identified as plasmon peaks. Also, these peaks correspond to the peaks seen in $\epsilon_2(\omega)$ spectra. The plasmon peak values are given in Table 3.

The frequency dependent reflectivity spectrum for both compounds is displayed in Fig. 6d. Plasmon resonance can also be confirmed by variations occurred in the reflectivity $R(\omega)$. Using the imaginary part of the dielectric function, $\epsilon_2(\omega)$, the plasmon smallest depth is determined at plasma resonance and is a function of the degree of overlap between the inter-band absorption regions [18]. The values of the three components at zero-frequency reflectivity (i.e. $R^{xx}(0)$, $R^{yy}(0)$ and $R^{zz}(0)$) for both compounds are given in Table 3. After this, the reflectivity $R(\omega)$ reaches to maximum and then decreases with further increase in energy. It is interesting to note that the maximum peak values of reflectivity occurs at 0.25 eV for $Rb_2Pd_3US_6$ and 0.38 eV for $Rb_2Pd_3USE_6$ where the $\epsilon_1(\omega)$ becomes zero, as seen from Fig. 6d and b.

4. Conclusion

We have performed the first principle calculations on electronic band structure, density of states (DOS), electronic charge density, Fermi surface and optical properties of $Rb_2Pd_3UM_6$ ($M = S, Se$) compounds using the FP-LAPW method within the mBJ approximation. The band structure calculations show that both compounds have zero band gap and show metallic band structure. From calculated DOS, it is concluded that the valence band is mainly attributed to Rb-p, Pd-d and S-s/p or Se-s/p states while conduction band is mainly attributed to Pd-d, U-f and S-p or Se-p/d states. The electronic charge density spectrum reveals that maximum charge sharing between Pd and S, and Pd or Se show covalent bond nature whereas no charge transfer between U and S, U and Se, Rb and S, and Rb and Se atoms responsible for ionic bond nature. Also, the Fermi surface spectrum confirms

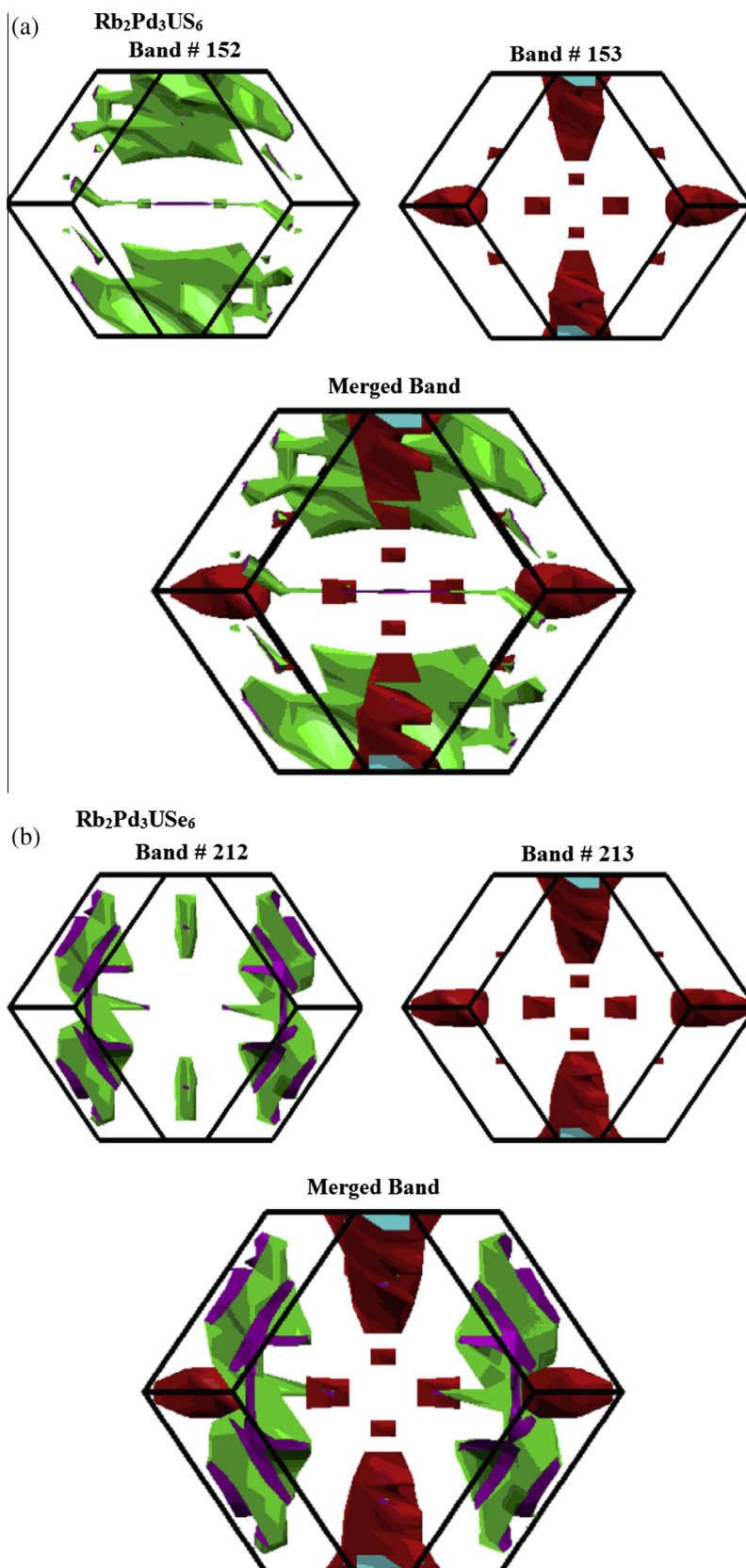


Fig. 5. Calculated Fermi surfaces of Rb₂Pd₃US₆ (a) and Rb₂Pd₃US₆ (b).

that both compounds have same number of fast velocity electrons but different number of slow or intermediate velocity of electrons. Additionally, the maximum peak values of the imaginary

part of dielectric function and the energy-loss function, the zero limit frequency of real part of dielectric function and reflectivity are calculated and discussed in details.

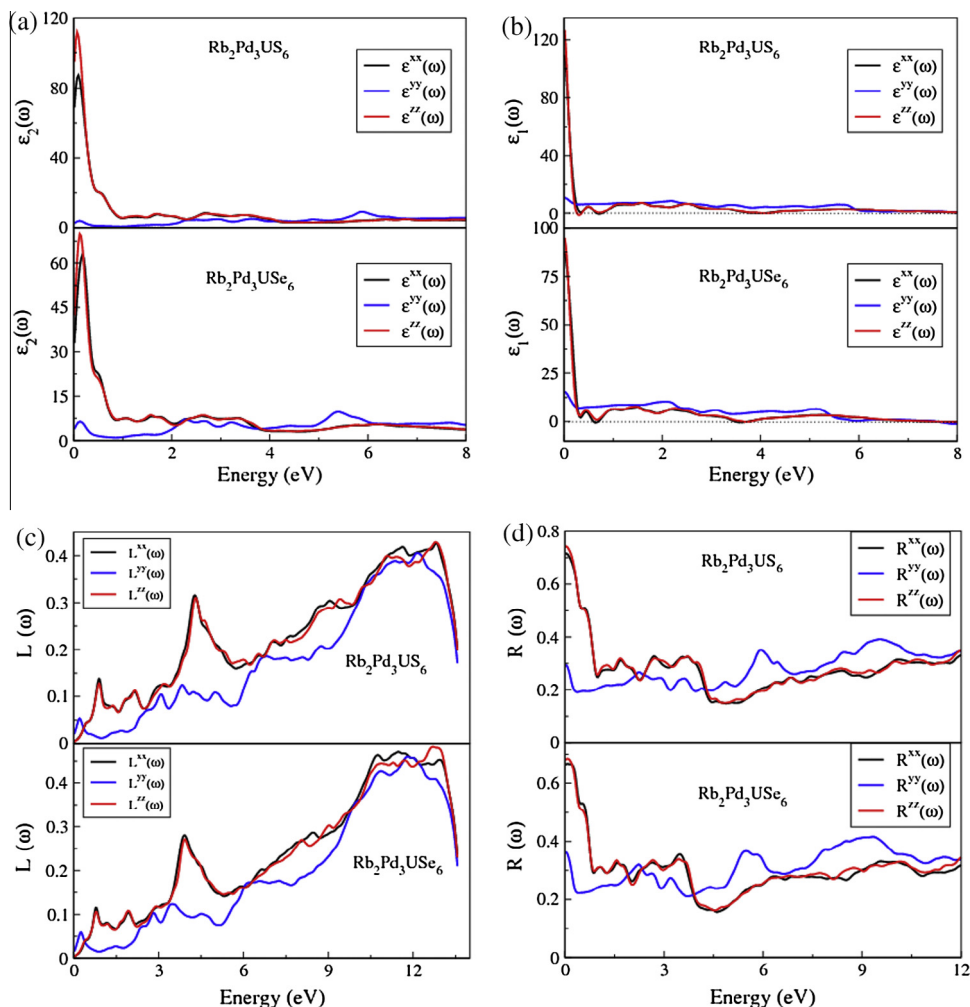


Fig. 6. Calculated imaginary $\varepsilon_1(\omega)$ (a), real $\varepsilon_2(\omega)$ (b) parts of dielectric function, energy loss $L(\omega)$ (c) and reflectivity $R(\omega)$ (d) of Rb₂Pd₃UM₆ (M = S, Se).

Table 3

Calculated highest peak values of $\varepsilon_2^{xx}(\omega)$, $\varepsilon_2^{yy}(\omega)$ and $\varepsilon_2^{zz}(\omega)$, zero-frequency limit ($\varepsilon_1^{xx}(0)$, $\varepsilon_1^{yy}(0)$ and $\varepsilon_1^{zz}(0)$), maximum peak values of $L^{xx}(\omega)$, $L^{yy}(\omega)$ and $L^{zz}(\omega)$ and zero-frequency limit reflectivity ($R^{xx}(0)$, $R^{yy}(0)$ and $R^{zz}(0)$) for Rb₂Pd₃US₆ and Rb₂Pd₃US₆Se₆ compounds.

	Rb ₂ Pd ₃ US ₆	Rb ₂ Pd ₃ US ₆ Se ₆		Rb ₂ Pd ₃ US ₆	Rb ₂ Pd ₃ US ₆ Se ₆
$\varepsilon_2^{xx}(\omega)$	87.27	62.70	$L^{xx}(\omega)$	0.426	0.471
$\varepsilon_2^{yy}(\omega)$	8.97	9.68	$L^{yy}(\omega)$	0.459	0.460
$\varepsilon_2^{zz}(\omega)$	111.95	69.85	$L^{zz}(\omega)$	0.429	0.483
$\varepsilon_1^{xx}(0)$	109.28	86.98	$R^{xx}(0)$	0.713	0.664
$\varepsilon_1^{yy}(0)$	10.93	15.43	$R^{yy}(0)$	0.294	0.362
$\varepsilon_1^{zz}(0)$	126.73	94.93	$R^{zz}(0)$	0.739	0.681

Acknowledgements

The author (R.K) acknowledges the support by the National Plan for Science, Technology and Innovation under the research Project No. 11-NAN1465-02. The result was developed within the CENTEM Project, Reg. No. CZ.1.05/2.1.00/03.0088, co-funded by the ERDF as part of the Ministry of Education, Youth and Sports OP RDI program. And also Access to computing and storage facilities owned by parties and projects contributing to the National Grid Infrastructure MetaCentrum, provided under the programme "Projects of Large Infrastructure for Research, Development, and Innovations" (LM2010005), is greatly appreciated.

References

- [1] N. Oh George, E.S. Choi, J.A. Ibers, *Inorg. Chem.* 51 (2012) 4224.
- [2] N. Oh George, E.S. Choi, J. Lu, Lukasz A. Koscielski, M.D. Ward, D.E. Ellis, J.A. Ibers, *Inorg. Chem.* 51 (2012) 8873.
- [3] P. Hohenberg, W. Kohn, *Phys. Rev.* 136 (1964) 864.
- [4] W. Kohn, L.J. Sham, *Phys. Rev.* 140 (1965) A1133.
- [5] P. Blaha, K. Schwarz, G.K.H. Madsen, D. Kvasnicka, J. Luitz, *WEIN2K, an Augmented Plane Wave + Local Orbitals Programme for Calculating Crystal Properties*; Technische Universitat, Vienna, Austria, Wein, 2001, ISBN 3-9501031-1-2.
- [6] P. Dufek, P. Blaha, K. Schwarz, *Phy Rev. B* 50 (1994) 7279.
- [7] J.P. Perdew, K. Burke, M. Ernzerhof, *Phys. Rev. Lett.* 77 (1996) 3865.
- [8] E. Engel, S.H. Vosko, *Phys. Rev.* B50 (1994) 10498.
- [9] F. Tran, P. Blaha, *Phys. Rev. Lett.* 102 (2009) 226401.
- [10] Sikander Azam, A.H. Reshak, *Int. J. Electrochem. Sci.* 8 (2013) 10359.
- [11] A.H. Reshak, Sikander Azam, *Int. J. Electrochem. Sci.* 8 (2013) 10396.
- [12] Hayatullah, S. Naeem, G. Murtaza, R. Khenata, M.N. Khalid, *Physica B* 414 (2013) 91.
- [13] Hayatullah, G. Murtaza, R. Khenata, S. Mohammad, S. Naeem, M.N. Khalid, A. Manzar, *Physica B* 420 (2013) 15.
- [14] Haleem Ud Din, A.H. Reshak, *Comp.Mat.Sci.* 83 (2014) 474.
- [15] Roshan Ali, G. Murtaza, Y. Takagiwa, R. Khenata, Haleem Ud Din, H. Ullah, S.A. Khan, *Chin. Phys. Lett.* 31 (4) (2014) 047102.
- [16] Roshan Ali, S. Mohammad, Hamid Ullah, S.A. Khan, H. Uddin, M. Khan, N.U. Khan, *Phys. B* 410 (2013) 93.
- [17] A.H. Reshak, H. Kamarudin, S. Auluk, *J. Phys. Chem. B.* 116 (2012) 4677.
- [18] Saleem Ayaz Khan, A.H. Reshak, *Int. J. Electrochem. Sci.* 8 (2013) 9459.
- [19] A. Delin, P. Ravindran, O. Eriksson, J.M. Wills, *Int. J. Quant. Chem.* 69 (1998) 349.
- [20] D.R. Penn, *Phys. Rev.* 128 (1962) 2093.
- [21] G. Murtaza, Hayatullah, R. Khenata, M.N. Khalid, S. Naeem, *Physica B* 410 (2013) 131–136.
- [22] R. Hoffman, *Rev. Mod. Phys.* 60 (1988) 601.
- [23] C.D. Gellatt, A.R. Williams Jr., V.L. Moruzzi, *Phys. Rev. B.* 27 (1983) 2005.
- [24] A.H. Reshak, Jan Chyský, Sikander Azam, *Int. J. Electrochem. Sci.* 9 (2014) 460.



Contents lists available at ScienceDirect

Journal of Solid State Chemistry

journal homepage: www.elsevier.com/locate/jssc

Exploring the electronic structure and optical properties of the quaternary selenide compound, $\text{Ba}_4\text{Ga}_4\text{SnSe}_{12}$: For photovoltaic applications

Sikander Azam^a, Saleem Ayaz Khan^a, Souraya Goumri-Said^{b,*}^a *New Technologies – Research Center, University of West Bohemia, Univerzitni 8, 306 14 Pilsen, Czech Republic*^b *School of Chemistry and Biochemistry and Center for Organic Photonics and Electronics, Georgia Institute of Technology, Atlanta, GA 30332-0400, USA*

ARTICLE INFO

Article history:

Received 23 April 2015

Received in revised form

5 June 2015

Accepted 8 June 2015

Available online 12 June 2015

Keywords:

Selenides

Semiconductors

ab-initio calculations

Electronic structure

Optical properties

ABSTRACT

Due to huge demand on discovering new materials for energy, we used first-principle calculations to explore the electronic structure and optical properties of a recent quaternary selenide, namely $\text{Ba}_4\text{Ga}_4\text{SnSe}_{12}$. The electronic structure and the optical properties of $\text{Ba}_4\text{Ga}_4\text{SnSe}_{12}$ were calculated through a reliable approach of Engle Vosko-GGA (EV-GGA). We found that $\text{Ba}_4\text{Ga}_4\text{SnSe}_{12}$ has a direct band gap of 2.14 eV positioned at Γ . Acquiring the fundamental characteristics of $\text{Ba}_4\text{Ga}_4\text{SnSe}_{12}$, we studied the linear optical properties like dielectric function in the energy range of 0–14 eV. From the dielectric function we noticed a weak directional anisotropy for the two components. The absorption spectrum indicates the possibility of greater multiple direct and indirect inter-band transitions in the visible regions and shows similar behavior with experimental spectrum. $\text{Ba}_4\text{Ga}_4\text{SnSe}_{12}$ can be used as shielding material from UV radiations. Present study predicts that the $\text{Ba}_4\text{Ga}_4\text{SnSe}_{12}$ is promising for photovoltaic applications due to their high absorption of solar radiations and photoconductivity in the visible range.

© 2015 Elsevier Inc. All rights reserved.

1. Introduction

There has been an abundant research in the field of physics and chemistry for binary and ternary chalcogenides during the past decade which has paved path for a comprehensive understanding of these solutions causing significant advances in quaternary material preparation techniques. Due to rich structural chemistry and unusual physical properties the chalcogenides are much interesting [1–6]. Quaternary chalcogenide compounds have a very diverse and interesting structural chemistry and show useful physical and chemical properties that may be applicable to modern technologies. They have attracted much attention because of the relative ease of their preparation from the melt and their interesting physical, thermal and optical properties. Furthermore, chalcogenide glasses exhibit a continuous change of their properties by changing their chemical structure. Important studies on characterization, crystallization kinetics and optical constants have recently been reported [5–7]. Furthermore, these materials have been subject of intensive research with application of new synthetic methods, such as the surfactant-thermal method [4–12]

with aim to control the sizes and shapes of nano-crystals.

The non-centrosymmetric polar characteristics and simultaneous transmission of long wavelength radiation required of such crystals point to complex chalcogenides as a potential source of NLO materials. As a source of new NLO materials, quaternary chalcogenides are attractive due to a variety of acentric arrangements resulting from the combination of two kinds of metal centers with different size, coordination preference, and packing characteristics [13]. Rare-earth chalcogenides have exhibited not only rich structures resulting from the diverse geometry of the Ln centered coordination polyhedra and the flexible connectivity among them, but also attractive magnetic, transport, and optical properties related to the 4f electrons [14]. Yin et al. [15] in early studies developed the quaternary $A/M/M'/Q$ (A =alkaline-earth metal; M =Al, Ga, In; M' =Si, Ge; Q =S, Se, Te) system and originate four iso-structural compounds, BaGa_2MQ_6 (M =Si, Ge; Q =S, Se), which were described to be a new-fangled series of IR nonlinear optical materials showing promise for practical applications. Recently, Yin et al. [15] have presented the synthesis, structural characterizations, and band gap measurements of an interesting quaternary selenide, $\text{Ba}_4\text{Ga}_4\text{SnSe}_{12}$. They also reported its electronic band structure calculated using the plane-wave pseudo-potential method. The later employed method is non-full potential method and might suffer from some shortcoming. In the present

* Corresponding author.

E-mail address: Souraya.Goumri-Said@chemistry.gatech.edu (S. Goumri-Said).

study, we thought it would be worthwhile to perform calculations by considering a full potential approach and we used all electrons full potential linear augmented plane wave method. Our calculation has led to band gap very close to the experimental value [15]. Hence, we completed our investigation by bonding characterization and optical properties to explore its potential application as material for photovoltaic devices. The present work has been divided in three parts. In Section 2, we briefly describe the computational technique and crystal structure of $\text{Ba}_4\text{Ga}_4\text{SnSe}_{12}$ compound. The most relevant results obtained for the electronic and optical properties are presented and discussed in Section 3. Finally, in Section 4, we summarize the main conclusions of the present work.

2. Computational method and crystal structure

The present calculations were performed using the full potential linearized augmented plane wave (FP-LAPW) as implemented in WIEN2k program [16] in the frame work of density functional theory (DFT) [17,18]. This method suggests that the unit cell space is split into interstitial region (IR) and non-overlapping Muffin-tin (MT) sphere centered at the atomic sites. Generalized gradient approximation (GGA) with Engel and Vosko parameterization (EV-GGA) [19] has been used to treat the exchange–correlation potential. Optimization of the ground state properties was achieved with the help of DFT based EV-GGA scheme. Relaxed geometry is obtained when the forces acting on each atom is minimized. Minimization of forces means that the structure is completely relaxed for the force values less than 1 mRy/au. Self-consistence convergence was set to 10^{-4} Ry. The core and valence states were treated fully relativistically and scalar relativistically respectively. The cutoff parameter $R_{\text{MT}}K_{\text{max}}$ which controls the convergence of basis set is taken to be 7.0, where R_{MT} is the smallest atomic sphere radius in the unit cell and K_{max} represents magnitude of the largest K vector. The calculations were carried out with 2000K points mesh integration over the irreducible Brillouin zone (IBZ).

We are applying the described method to the recently synthesized quaternary selenides, $\text{Ba}_4\text{Ga}_4\text{SnSe}_{12}$ compound. This selenide, possess newly typed structures in the cubic crystal system with space group P-421c (No. 114) (see Fig. 1). Lattice constants and atomic coordinates were obtained from the experimental measurements [15]. The structure of $\text{Ba}_4\text{Ga}_4\text{SnSe}_{12}$ was fully relaxed before proceeding with further calculations.

3. Results and discussion

3.1. Electronic band structure and density of states

The obtained results related to the electronic properties of the

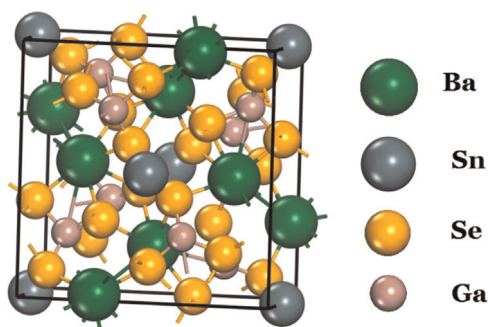


Fig. 1. Representation and labeling of unit cell structure of $\text{Ba}_4\text{Ga}_4\text{SnSe}_{12}$.

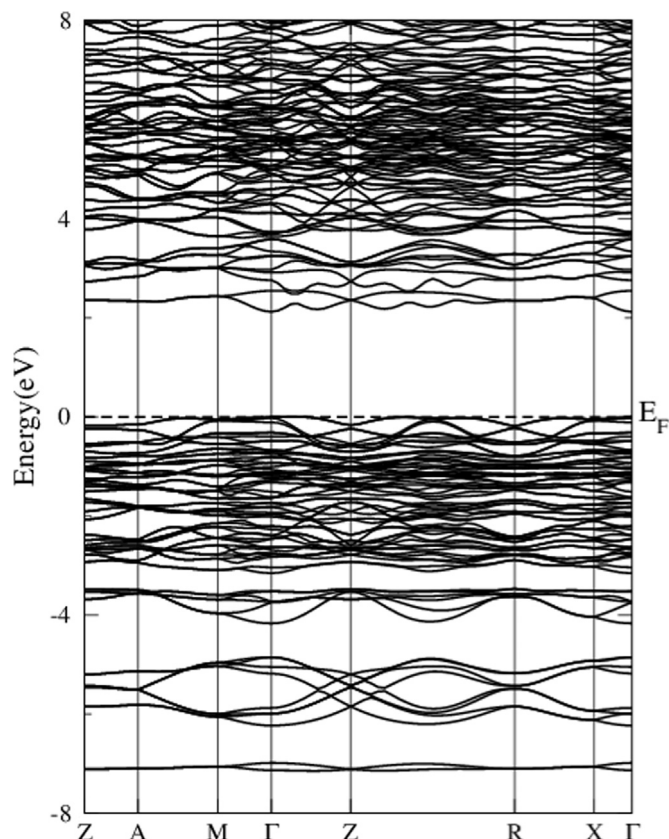


Fig. 2. Electronic band structure along high symmetry points.

$\text{Ba}_4\text{Ga}_4\text{SnSe}_{12}$ compound are discussed via energy band structures. Band structure for $\text{Ba}_4\text{Ga}_4\text{SnSe}_{12}$ compounds is calculated along high symmetry points $Z \rightarrow A \rightarrow M \rightarrow \Gamma \rightarrow Z \rightarrow R \rightarrow X \rightarrow \Gamma$ in the Brillouin zone as shown in Fig. 2. The zero energy is arbitrarily taken at the Fermi level. The energy scale is in eV, and the valence band maximum is set to be at the Fermi energy (E_F), indicating that the bands below E_F are all occupied. It is well known that both LDA and GGA underestimate the band gap of semiconductors, so in this regards we used EV-GGA approximation which yields better band splitting with respect to LDA and GGA. Therefore we preferred to show here results related to EV-GGA approach. The important parameter (that is of great interest in semiconductors), can be determined from the energy band structure is the band gap E_g that is the impact of energies between the lower conduction band (CB) and topmost valence band (VB). From our calculations, we estimated the value of the band gap to $E_g = 2.14$ eV. This is very close to the experimental measurement (2.16 eV) and shows that the full potential calculations describe correctly the present selenide compared to the pseudo-potential method (which led to a band gap value of 1.42 eV) [15]). Principally, the energy structure of the materials depends on the interactions between orbitals in the lattice. It is quite evident that the investigated selenide has a direct band gap as the valence band maximum (VBM) and the conduction band minimum (CBM) arises at $\Gamma-\Gamma$ point of BZ. In order to understand the major contribution of orbitals/atoms in the band structure, the total and atom-resolved density of states (DOS) were calculated and reported in Fig. 3. The plots for the total/partial density of states (TDOS and PDOS) are depicted in Fig. 3. Narrowly four bands are examined in the energy ranges from -15.0 to 15.0 eV. The PDOS reveals that, in the valence band, the major contribution comes from Ba- p and Ga- d . The bands are separated by narrow gaps around -14.0 to -13.5 , -10.5 to -7.5 , -7.0 to -6.5 , and 5.0 to -4.0 eV. The structure from -15.0 to

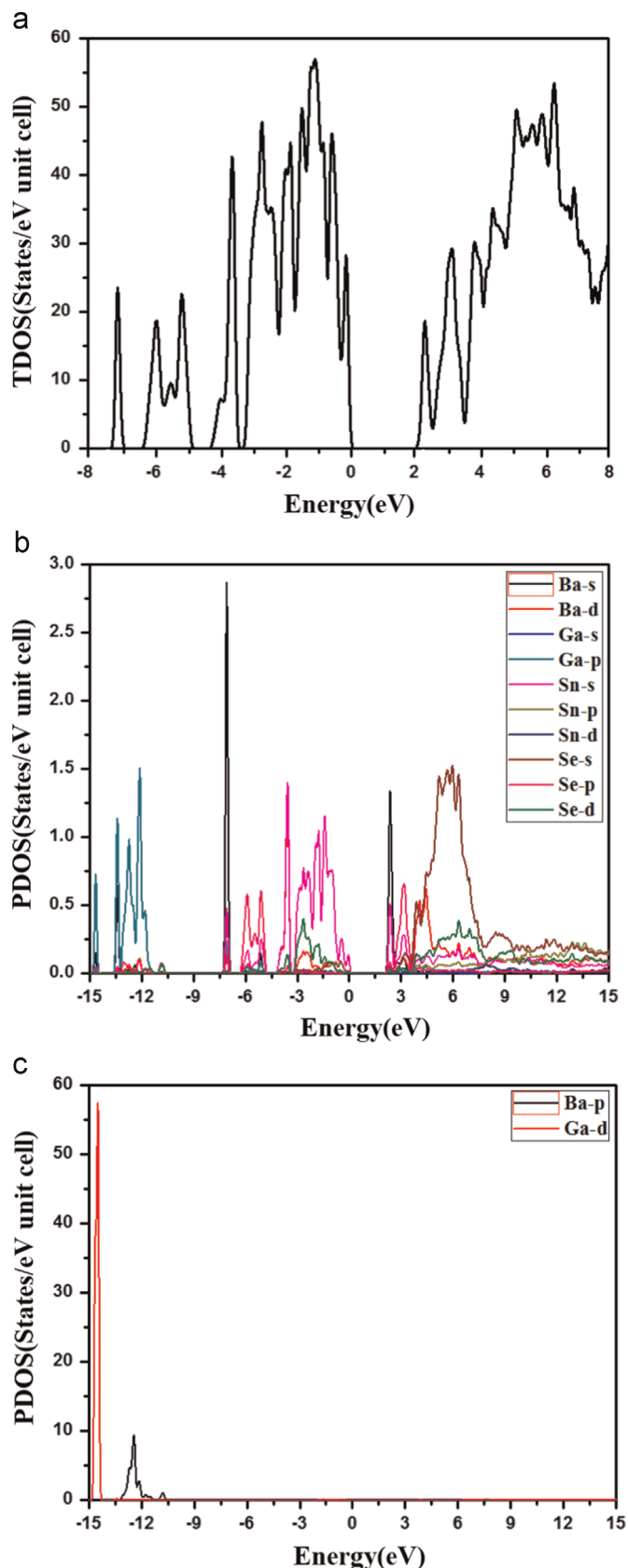


Fig. 3. Calculated TDOS and PDOS (states/eV unit cell) for $\text{Ba}_4\text{Ga}_4\text{SnSe}_{12}$.

–14.0 eV is due to the major contribution of Ga-*p/d* with small contribution from Ba-*s* and Se-*p* states. The region between –13.5 and –11.0 consists of Ba-*p*, Ga-*p* and Ba-*s* states with a small

contribution from Ba-*d* state. The bands between –8.5 and 7.0 are due to the Ba-*s* with a small admixture of Sn-*s* state. The structure at the maximum valence band comes from Sn-*s* and Se-*p* with small contribution from Se-*d* and Ba-*d* states. In the lower conduction band Ba-*s*, Se-*p*, Sn-*s*, Ba-*d* and Se-*s* states have the main contribution. A strong hybridization exists between Ga-*p* and Ba-*s*, Ba-*s* and Sn-*s*, Sn-*s* and Se-*p* states in both valence and conduction bands. From the density of state (PDOS) we conclude that the investigated compound has some covalent features in spite of its main ionic character.

We also calculated the effective mass of charge carriers (electrons or holes) by fitting the dispersion curve using the following expression:

$$\frac{1}{m_{ij}^*} = \frac{2}{\hbar^2} \frac{d^2 E_{ij}}{dk_{ij}^2}$$

Using the effective mass (m^*), one can describe the motion of electrons inside the bands which were influenced by the applied force. Furthermore, charge carriers in the bands have different effective masses which depend on energy [9] and the inverse proportion between the effective masses and the energy band curvature lead to higher values of the effective mass. We calculated the effective mass of electrons in the $\text{Ba}_4\text{Ga}_4\text{SnSe}_{12}$ compound and found it equal to $0.345 \times m_e$ (m_e presents the rest mass of electrons). The effective masses value of the present selenide is smaller compared to a similar chalcogenide recently synthesized and characterized, PbGa_2Se_4 [20]. The effective masses values in Y–X direction were found equal to $1.396434 \times m_e$ and in direction Y– Γ is equal to $5.149053 \times m_e$. When the effective masses of electrons/holes are sufficiently huge, the conductivity and carrier mobilities are relatively low. On the other hand, the high effective mass is sign good thermoelectric performance. Consequently, the considered selenide is more appropriate to photovoltaic application than thermoelectric properties [21,22].

3.2. Electronic charge density and bonding characteristics

Charge density distributions enrich us with further insight into the electronic structure and information about chemical bonding nature of the compound. Charge density distributions also serve as good indicator about the maximum and the minimum charge sites. The calculated valence charge density (Fig. 4a and b) is a useful probe to predict the chemical bonding and charge transfer in $\text{Ba}_4\text{Ga}_4\text{SnSe}_{12}$ material. Highly converged wave function is used to plot valence charge density (3D iso-surface shown in Fig. 4a) [23]. The 3D iso-surface shows that the charges are localized on Sn, Se and Ga atoms compared to Ba atom. The 2D charge density plot in (1 0 1) crystallographic plane shows high degree of asymmetry. Electro-negativity plays significant role in understanding charge transfer mechanism. The electro negativity values are Ba (0.9), Sn (1.8), Se (2.5) and Ga (1.81) among which Se atom being most electronegative thus acquire maximum charge concentration site. From the color scale it can be also confirmed that the maximum charge accumulated around the Se atom, as yellow color indicates greater charge concentration while orange, red and black colors represent zero and negative charge regions (which are mostly interstitials between different atoms). As we observed from PDOS, there exists a strong hybridization between the states of Ba, Se, Sn and Ga atoms, reflecting a covalent bonding between these atoms. In 2D plot of $\text{Ba}_4\text{Ga}_4\text{SnSe}_{12}$ (Fig. 4b), covalent bonding exist between Se-Ga.

3.3. Optical properties

The optical properties of solids give a significant means for

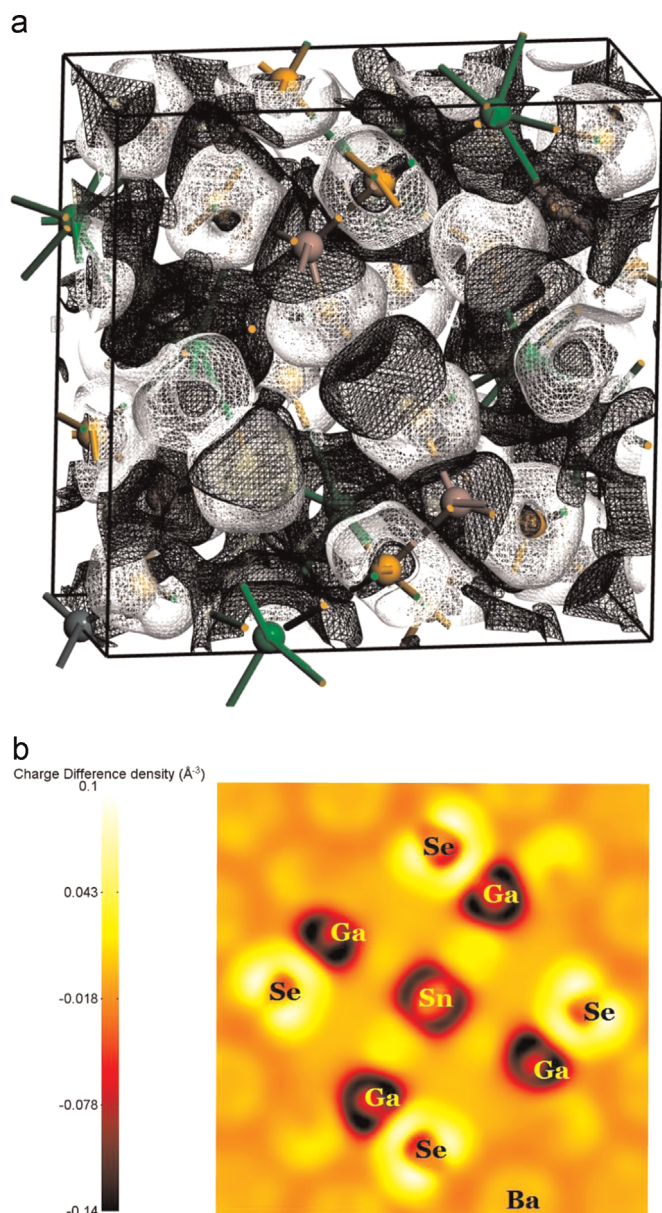


Fig. 4. Calculated electronic charge density (a) 3D isosurface. (b) 2D maps. (For interpretation of the references to color in this figure, the reader is referred to the web version of this article.)

studying localized defects, excitons, lattice vibrations, energy band structure, impurity levels, and certain magnetic excitations. The light interacts with matter in many ways whose effects are of great interest for materials. Transition of electrons takes place between the occupied valence bands and the unoccupied conduction bands when light of particular energy falls on the materials surface. These transitions act as source of information about the energy bands. This is the reason that energy dependent optical properties are related to the band structure. Complex dielectric function $\epsilon(\omega) = \epsilon_1(\omega) + i\epsilon_2(\omega)$ is one of the most important optical characteristic of materials. Intra-band and inter-band are the two main transition effects that occur in the dispersion of dielectric function. Intra-band transitions are more important in metals and contribute mostly to the dielectric function. Inter band transition (direct and indirect) is most common in semiconductors. Dielectric function explores much useful information about the optical nature of the materials. The crystal structure of trigonal bears two major non-zero dielectric components of $\text{Ba}_4\text{Ga}_4\text{SnSe}_{12}$ material.

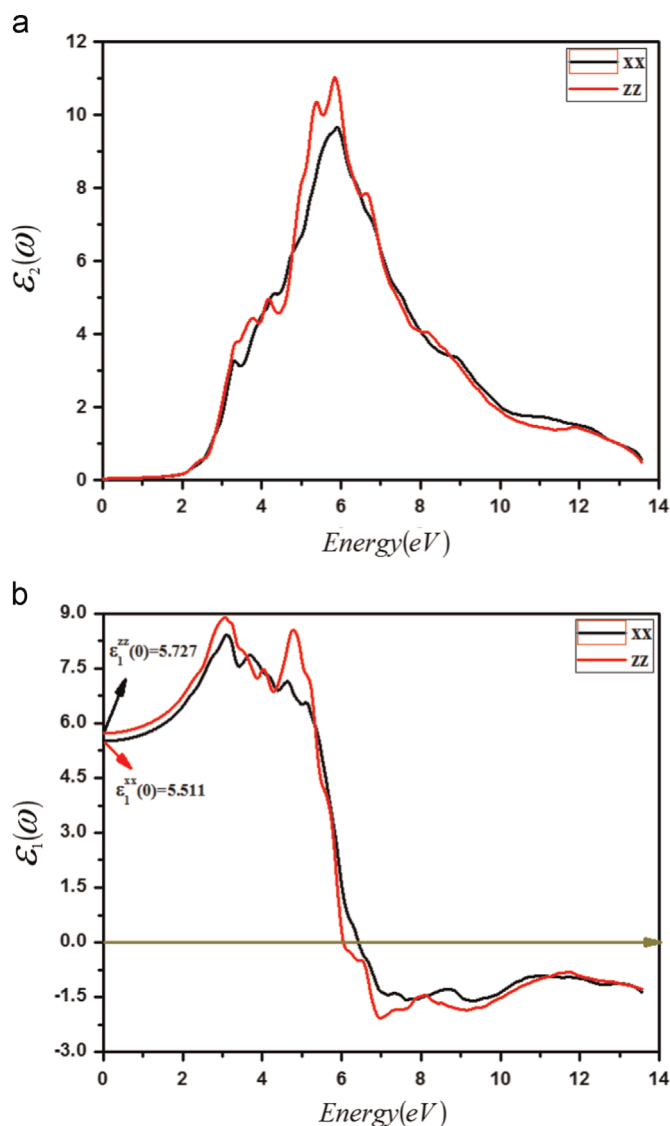


Fig. 5. (a and b) Calculated imaginary part $\epsilon_2^{\text{XX}}(\omega)$ (dark solid curve – black color online) and $\epsilon_2^{\text{ZZ}}(\omega)$ (long solid curve – red color online) spectra; calculated real part $\epsilon_1^{\text{XX}}(\omega)$ (dark solid curve – black color online) and $\epsilon_1^{\text{ZZ}}(\omega)$ (long solid curve – red color online) spectra. (For interpretation of the references to color in this figure legend, the reader is referred to the web version of this article.)

The optical transitions can be illuminated from our investigated band structure and density of states. The optical properties are calculated at equilibrium lattice parameters as a function of incident photon energy up to 14 eV as shown in Fig. 5. The imaginary $\epsilon_2(\omega)$ and real $\epsilon_1(\omega)$ parts of the dielectric tensor components are presented in Fig. 5(a and b) for $\text{Ba}_4\text{Ga}_4\text{SnSe}_{12}$ compound. The $\epsilon_2(\omega)$ spectrum shows that the critical point of the dielectric function comes about 2.0 eV. So this material shows transmission till 2.0 eV and above 2.0 eV the absorption starts. Therefore, this material possesses potential application in visible regions. The fundamental absorption edges give the threshold for direct optical transitions between the top of valence band and bottom of conduction band. This critical point is the absorption edge for the optical transitions between the highest valence band and the lowest conduction bands (i.e., Sn-s \rightarrow Ba-s). The imaginary part shows a steep peak at around 6.0 eV. The two components show maximum anisotropy between 6.0 and 8.0 eV. We should highlight that the anisotropy in the optical (linear) susceptibilities favors an improved phase matching conditions required for study of the second harmonic generation (SHG) and optical parametric

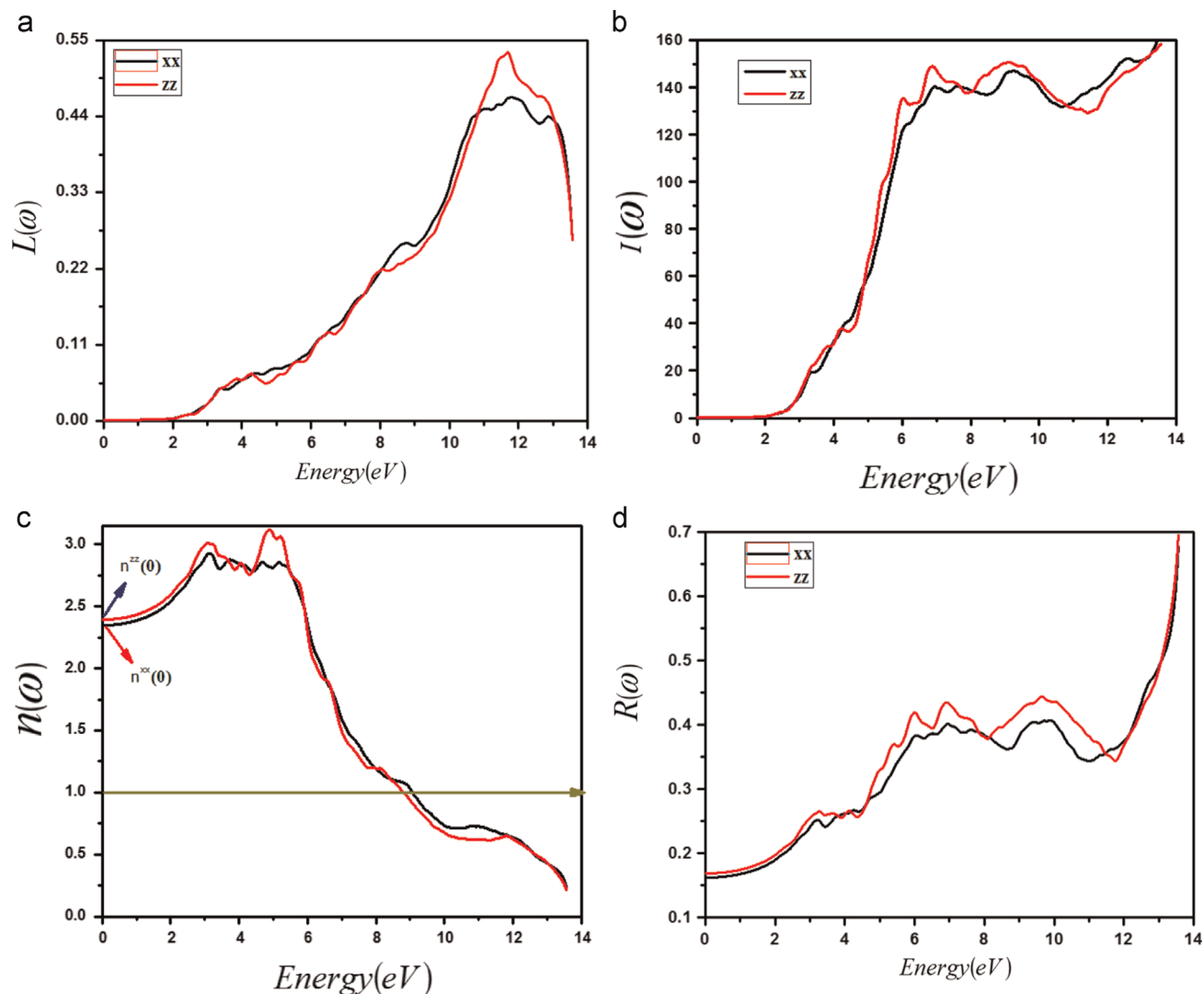


Fig. 6. (a–d) Calculated energy-loss spectrum $L^{xx}(\omega)$ (long solid curve – black color online) and $L^{zz}(\omega)$ (long solid curve – red color online) spectra; calculated energy-loss spectrum $I^{xx}(\omega)$ (long solid curve – black color online) and $I^{zz}(\omega)$ (long solid curve – red color online) spectra; calculated refractive index $n^{xx}(\omega)$ (long solid curve – black color online) and $n^{zz}(\omega)$ (long solid curve – red color online) spectra; calculated reflectivity $R^{xx}(\omega)$ (long solid curve – black color online) and $R^{zz}(\omega)$ (long solid curve – red color online) spectra. (For interpretation of the references to color in this figure legend, the reader is referred to the web version of this article.)

oscillation (OPO).

The peaks that arise in the optical dispersion are due to possible electric dipole transitions from occupied state to unoccupied state. The real part $\epsilon_1(\omega)$ is evaluated from the imaginary part using the well-known Krammer–Kronig relation [24]. Considerable anisotropy found among the two components for the investigated selenide and two main peaks are situated in between 3.0 eV and 5.0 eV. Our calculated, $\epsilon_1^{xx}(\omega)$ and $\epsilon_1^{zz}(\omega)$ are displayed in Fig. 5b. The static limit for the real part of dielectric function, $\epsilon_1(0)$, along the two crystallographic directions is found to be 5.511 and 5.727 for $\epsilon_1^{xx}(0)$ and $\epsilon_1^{zz}(0)$. The uniaxial anisotropy $\delta\epsilon = [(\epsilon_0^{xx} - \epsilon_0^{zz})/\epsilon_0^{tot}]$ is 0.03844 indicating the existence of the anisotropy. Energy loss function $L(\omega)$ describes the energy loss by a fast moving electron in materials. The energy loss functions for the investigated selenide are drawn in Fig. 6a. As the energy increases the loss function spectra peaks also increases, the main peaks of the energy loss function for the two components (xx and yy) are in between 10.5 and 13.0 eV. These peaks are defined as the bulk plasma frequency ω_p^\perp and mostly occur when $\epsilon_1(\omega)$ reaches zero point. Hence, incident light with frequency greater than 6.0 eV the materials becomes transparent. In the energy loss spectra the peaks are related

to inter-band transitions and plasmon energies. The energy loss spectra and the real part of dielectric function concurrently indicate that the comparative maximums in energy loss functions are connected to the energy of plasmon oscillations. It is practical that the comparative extreme in the energy loss function take places with an excellent estimate at energies somewhere the dielectric function $\epsilon_1(\omega)$ crosses the zero line. At this energy value the reflectivity spectrum suddenly dropped. The components show maximum isotropy between 11.0 and 13.0 eV and the rest of the curves are highly anisotropic in the lower energy range.

Another important optical parameter is the reflectivity $R(\omega)$ that is illustrated in Fig. 6b. Spectrum of the reflectivity $R(\omega)$ shows small values in the visible range as the energy increases the peaks shows inclination. Reflectivity for the investigated compound is about 70% at high energy and in between 6.0 and 10.0 eV, the reflectivity is above 45%. So it is concluded that the investigated compound can be partially used as a shielding material in ultra violet regions. The maximum reflectivity takes place where the real part of dielectric function $\epsilon_1(\omega)$ becomes negative. The absorption spectrum $I(\omega)$ is plotted in Fig. 6c, in the energy range of 0.0–14.0 eV, the spectrum reflects that the deep absorption

occurs at high energies. This absorption first peak originates from Sn-s state, which is situated at the top of the valence bands to the empty Ba-s state, i.e. at the bottom of the conduction bands. In the absorption spectra the first highest peak takes places almost at about 2.0 eV for $I^{xx}(\omega)$ and $I^{zz}(\omega)$ components, which shows similar behavior with experimental results [15].

Finally, we also calculated the refractive index $n(\omega)$ for the investigated compound as displayed in Fig. 6d. The refractive index is intimately related to the electronic polarizability of ions and the local field inside the crystal. The plot of the refractive index is displayed in Fig. 5e. The relation between the refractive index and complex dielectric function is $\epsilon_1(\omega) = n^2 + k^2$, $\epsilon_2(\omega) = 2nk$ [25]. At low energies the peaks emerge and with increasing energies the curves vanish. The reason for these discarding of curves at higher energy is due to the fact that beyond certain energy the material is no longer considered as transparent material, and it absorbs high energy photons. It is also clear from Fig. 6d that the refractive index falls below unity at number of frequencies. So it means that material crossing zero, the material becomes superluminal for high energy photon. From the spectra of the refractive index, one can observe that the refractive index $n(\omega)$ approximately follows $\epsilon_1(\omega)$ while the extinction coefficients changes in a similar fashion as $\epsilon_2(\omega)$.

4. Conclusion

Employing FP-LAPW method based on the DFT within Engel Vosko GGA we have presented detailed study on electronic and optical properties of the quaternary selenide named $\text{Ba}_4\text{Ga}_4\text{SnSe}_{12}$. It has been established on the basis of electronic band structure that $\text{Ba}_4\text{Ga}_4\text{SnSe}_{12}$ has a semi conducting nature with a direct band gap at Γ point. Real and imaginary parts of the dielectric function, reflectivity and refractive index were reported. Our theoretical investigations were found more accurate compared to the previous theoretical work were they found a band gap value of 1.42 eV whereas our finding is close to the measured value (i.e. 2.16 eV). The lower energy region of the CB (conduction band) is mainly formed by a mixture of Ba-s, Se-p, Sn-s, Ba-d and Se-s states, while its (conduction band) higher energy region are composed of Ba-d, Ga-p, Sn-p and Se-s/p/d orbitals. The lower energy region VB (valence band) is mainly induced by Ga-p/d states, and its (valence band) upper energy region comprised from the Sn-s and Se-p states. The present selenide, $\text{Ba}_4\text{Ga}_4\text{SnSe}_{12}$, has a maximum reflectivity in the visible and UV regions of electromagnetic spectrum leading to consider it for potential application as photovoltaic material.

Acknowledgments

The first two authors (S.A and S.K) are supported within the within the CENTEM project, reg. no. CZ.1.05/2.1.00/03.0088, co-funded by the ERDF as part of the Ministry of Education, Youth and Sports OP RDI program and, in the follow-up sustainability stage, supported through CENTEM PLUS (LO1402) by financial means from the Ministry of Education, Youth and Sports under the National Sustainability Programme I.MetaCentrum (LM2010005) and CERIT-SC (CZ.1.05/3.2.00/08.0144) infrastructures.

References

- [1] P. Klchambare, M. Sharon, Y. Seki, T. Hagino, S. Nagata, *Solid State Ion.* 125 (1997) 101.
- [2] A. Chatterjee, K. Biswas, *Angew. Chem. Int. Ed.* 54 (2015) 5623.
- [3] S.N. Guin, J. Pan, A. Bhowmik, D. Sanyal, U.V. Waghmare, K. Biswas, *J. Am. Chem. Soc.* 136 (2014) 12712.
- [4] W. Liu, J.-S. Lee, D.V. Talapin, *J. Am. Chem. Soc.* 135 (2013) 1349.
- [5] W.-W. Xiong, J. Miao, K. Ye, Y. Wang, B. Liu, Q. Zhang, *Angew. Chem. Int. Ed.* 54 (2015) 546.
- [6] W.-W. Xiong, G. Zhang, Q. Zhang, *Inorg. Chem. Front.* 1 (2014) 292–301.
- [7] W.-W. Xiong, E.U. Athresh, Y.T. Ng, J. Ding, T. Wu, Q. Zhang, *J. Am. Chem. Soc.* 135 (2013) 1256–1259.
- [8] W.-W. Xiong, P.-Z. Li, T.-H. Zhou, A.I.Y. Tok, R. Xu, Y. Zhao, Q. Zhang, *Inorg. Chem.* 52 (2013) 4148–4150.
- [9] J. Gao, Q. Tay, P.-Z. Li, W.-W. Xiong, Y. Zhao, Z. Chen, Q. Zhang, *Chem. Asian J.* 9 (2014) 131–134.
- [10] W.-W. Xiong, J. Miao, P.-Z. Li, Y. Zhao, B. Liu, Q. Zhang, *CrystEngComm* 16 (2014) 5989–5992.
- [11] K. Biswas, Q. Zhang, I. Chung, J.-H. Song, J. Androulakis, A.J. Freeman, M. G. Kanatzidis, *J. Am. Chem. Soc.* 132 (2010) 14760.
- [12] A. Dahshan, K.A. Aly, *J. Non-Cryst. Solids* 408 (2015) 62.
- [13] J.H. Liao, G.M. Marking, K.F. Hsu, Y. Matsushita, M.D. Ewbank, R. Borwick, P. Cunningham, M.J. Rosker, M.G. Kanatzidis, *J. Am. Chem. Soc.* 125 (2003) 9484.
- [14] J. Flahaut, in: Karl A. Gschneidner Jr., E. LeRoy (Eds.), *Handbook on the Physics and Chemistry of Rare Earths*, 4, Elsevier, 1979, p. 1.
- [15] W. Yin, K. Feng, R. He, D. Mei, Z. Lin, J. Yao, Y. Wu, *Dalton Trans.* 44 (2015) 2259–2266.
- [16] P. Blaha, K. Schwartz, G.K.H. Madsen, D. Kvasnicka, J. Luitz, *WIEN2K, An Augmented Plane Wave+Local Orbitals Program for Calculating Crystals Properties*, Karlheinz Schwartz, Techn. Universitat, Wien, Austria, 2001. ISBN: 3-9501031-1-2.
- [17] P. Hohenberg, W. Kohn, *Phys. Rev.* 136 (1964) 864.
- [18] W. Kohn, L.J. Sham, *Phys. Rev.* 140 (1965) A1133.
- [19] E. Engel, S.H. Vosko, *Phys. Rev.B: Condens. Matter* 50 (1994) 10498.
- [20] Yu. I. Ravich, *J. Phys. Colloques* 29 (1968) C4–114.
- [21] T. Babuka, I.V. Kityk, O.V. Parasyuk, G. Myronchuk, O.Y. Khyzhun, A. O. Fedorchuk, M. Makowska-Janusik, *J. Alloy. Compd.* 633 (2015) 415.
- [22] W. Khan, S. Goumri-Said, *RSC Adv.* 5 (2015) 9455.
- [23] S. Goumri-Said, M.B. Kanoun, *J. Solid State Chem.* 197 (2013) 304.
- [24] R. de L. Kronig, *J. Opt. Soc. Am.* 12 (1926) 547.
- [25] E. Marquez, A.M. Bernal-Olira, J.M. Goualez-Leat, Prieto-Alcon, A. Ledesma, R. Jimenez-Garay, Martil, *Mater. Chem. Phys.* 60 (1999) 231.



Contents lists available at ScienceDirect

Journal of Alloys and Compounds

journal homepage: www.elsevier.com/locate/jalcomDetailed DFT studies of the electronic structure and optical properties of KBaMSe_3 ($M = \text{As}, \text{Sb}$)Sikander Azam^a, Saleem Ayaz Khan^a, Wilayat Khan^a, Saleh Muhammad^b, Haleem Udin^b, G. Murtaza^{c,*}, R. Khenata^d, Fahad Ali Shah^b, Jan Minar^a, W.K. Ahmed^e^a New Technologies – Research Center, University of West Bohemia, Univerzitni 8, 306 14 Pilsen, Czech Republic^b Materials Modeling Lab, Department of Physics, Hazara University, Mansehra, Pakistan^c Materials Modeling Laboratory, Department of Physics, Islamia College University, Peshawar, Pakistan^d Laboratoire de Physique Quantique et de Modélisation Mathématique (LPQ3M), Département de Technologie, Université de Mascara, Mascara 29000, Algeria^e ERU, College of Engineering, United Arab Emirates University, Al Ain, United Arab Emirates

ARTICLE INFO

Article history:

Received 23 December 2014

Received in revised form 3 March 2015

Accepted 16 April 2015

Available online 29 April 2015

Keywords:

FP-LAPW

Electronic structure

Optical properties

ABSTRACT

Bonding nature as well as the electronic band structure, electronic charge density and optical properties of KBaMSe_3 ($M = \text{As}, \text{Sb}$) compounds have been calculated using a full-potential augmented plane wave (FP-LAPW) method within the density functional theory. The exchange–correlation potential was handled with LDA and PBE–GGA approximations. Moreover, the Engel–Vosko generalized gradient approximation (EV–GGA) and the modified Beck–Johnson potential (mBJ) were also applied to improve the electronic band structure calculations. The study of band structure shows that $\text{KBaAsSe}_3/\text{KBaSbSe}_3$ compounds have an indirect band gap of 2.08/2.10 eV which are in close agreement with the experimental data. The bonding nature has been studied as well using the electronic charge density (ECD) contour in the (101) crystallographic plane. It has been revealed that As/Sb–O atoms forms a strong covalent, while Ba–Se atoms form weak covalent bonding and the ionic bonding is mainly found between K and Ba atoms. Moreover, the complex dielectric function, absorption coefficient, refractive index, energy-loss spectrum and reflectivity have been estimated. From the reflectivity spectra, we found that KBaAsSe_3 compound shows greater reflectivity than KBaSbSe_3 , which means that KBaAsSe_3 compound can be used as shielding material in visible and also in ultra violet region.

© 2015 Elsevier B.V. All rights reserved.

1. Introduction

For the last few decades, the newly investigated multinary chalcogenides comprising two or more metal cations have been gaining immense importance for their structural and compositional complexity which is suitable for various physical properties (like thermoelectric, superconducting, magnetic and nonlinear optical properties), battery electrodes and photovoltaic applications [1]. The stereochemical activity of ns^2 lone pair of electrons of M ($M = \text{As}, \text{Sb}$) strongly affects the structure and electronic nature and the properties of the resultant compound as well. Over the past few years, the synthesis of new group 15 element-containing multinary chalcogenides has been performed and many chalcogenides with fascinating physical properties were discovered [1,2]. The quaternary KBaMSe_3 ($M = \text{As}, \text{Sb}$) selenides have been

determined isostructural and crystallized in the centrosymmetric space group $P21/c$ of the monoclinic crystal system. The trivalent M atom coordinated to three Se atoms forms a trigonal pyramid with the Se atoms serving as the triangle base and indicates the stereochemical activity of the ns^2 lone pair electron [3]. The microscopic packing of anions is greatly influenced by the size and charge of cations and generally determines the various properties in a crystal [3,4]. The mixture of different size and charge of the alkali and the alkaline-earth cations influences the packing of anions and demonstrates a considerable effect on the stoichiometries, structures and properties of KBaMSe_3 . An indirect band gap semiconductor nature have been investigated using the diffuse reflectance spectra [3] with band gap values 2.26 and 2.04 eV for KBaAsSe_3 and KBaSbSe_3 respectively.

Inspiring these significant properties discussed above, we have performed the electronic structure, electronic charge density and optical calculations of quaternary KBaMSe_3 ($M = \text{As}, \text{Sb}$) using the full potential linear augmented plane wave (FP-LAPW) method within the framework of Wien2k code.

* Corresponding author. Tel.: +92 321 6582416.

E-mail addresses: murtaza@icp.edu.pk (G. Murtaza), khenata_rabah@yahoo.fr (R. Khenata).

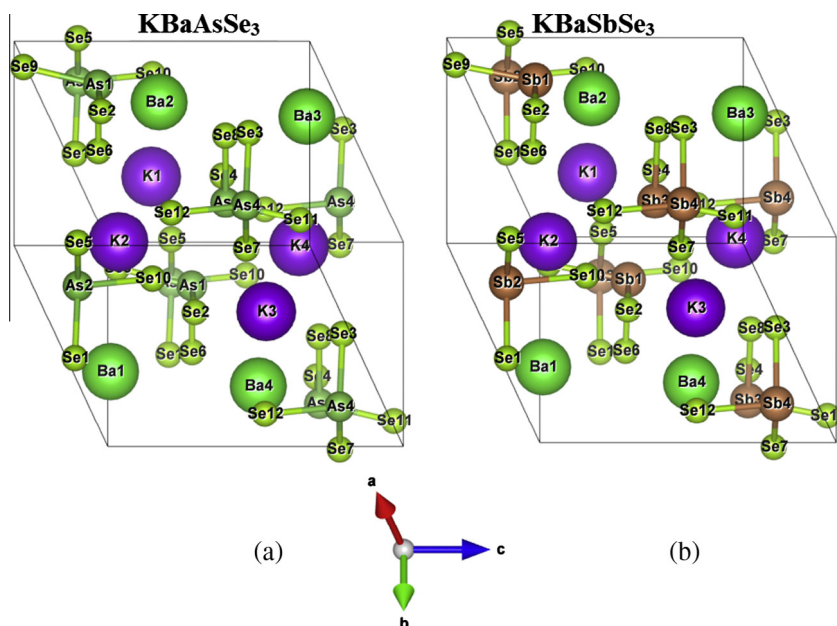


Fig. 1. The optimized crystal structure of KBaMSe_3 ($M = \text{As, Sb}$) compounds.

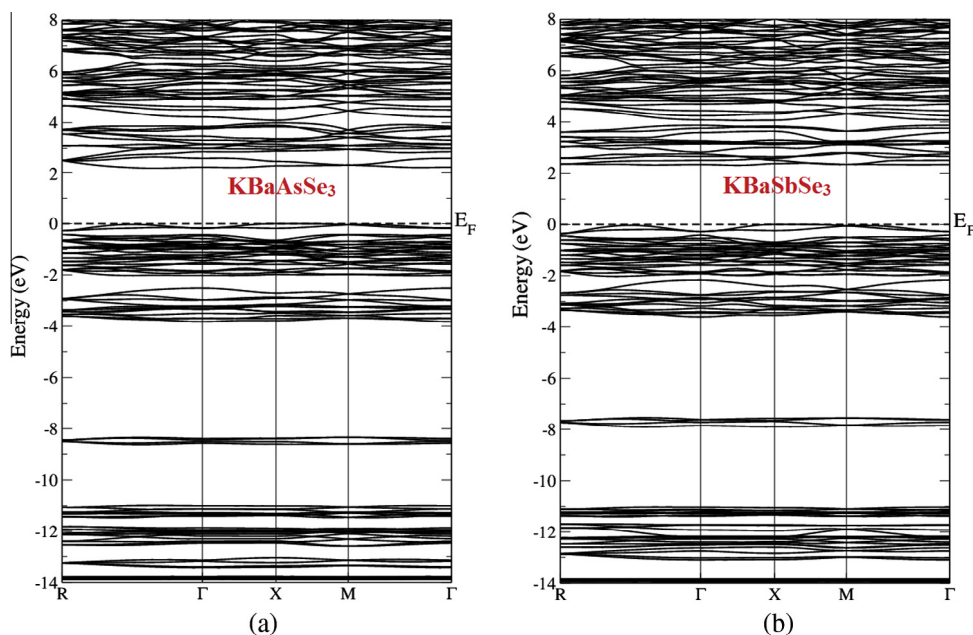


Fig. 2. Energy band structures of KBaMSe_3 ($M = \text{As, Sb}$) compounds, obtained by using the modified Becke–Johnson (mBJ). the conduction band minimum (CBM) is located at the Γ point of BZ for both compounds, while the valence band maximum (VBM) is located at the Y symmetry points for KBaAsSe_3 and at the middle of M point for KBaSbSe_3 , resulting in an indirect band gap for KBaAsSe_3 and KBaSbSe_3 .

In view of KBaMSe_3 ($M = \text{As, Sb}$), it has been known to our knowledge that there is a shortage of theoretical information. As a matter of fact, in the past the CASTEP code was used in investigating the electronic structure of these compounds [3]. The CASTEP code is considered as non-full potential method, where we thought that it would be worthwhile to do the calculations taking into account the importance of using full potential calculations; therefore we've used all electrons FPLAPW method. It has been observed that our computed energy band gaps are in fairly good agreement with the experimental data [3]. To the best of our

knowledge, no optical properties of KBaMSe_3 ($M = \text{As, Sb}$) have been yet reported in literature. Therefore, it stimulates us to deal with the electronic structure and the optical properties of KBaMSe_3 ($M = \text{As, Sb}$) through the present paper.

The paper structure is organized as follows: In Section 1, a comprehensive introduction of quaternary KBaMSe_3 ($M = \text{As, Sb}$) selenides is demonstrated. Section 2 is devoted to the method of calculations. The obtained results are discussed in details in Section 3 whereas the summary of the present work is presented in Section 4.

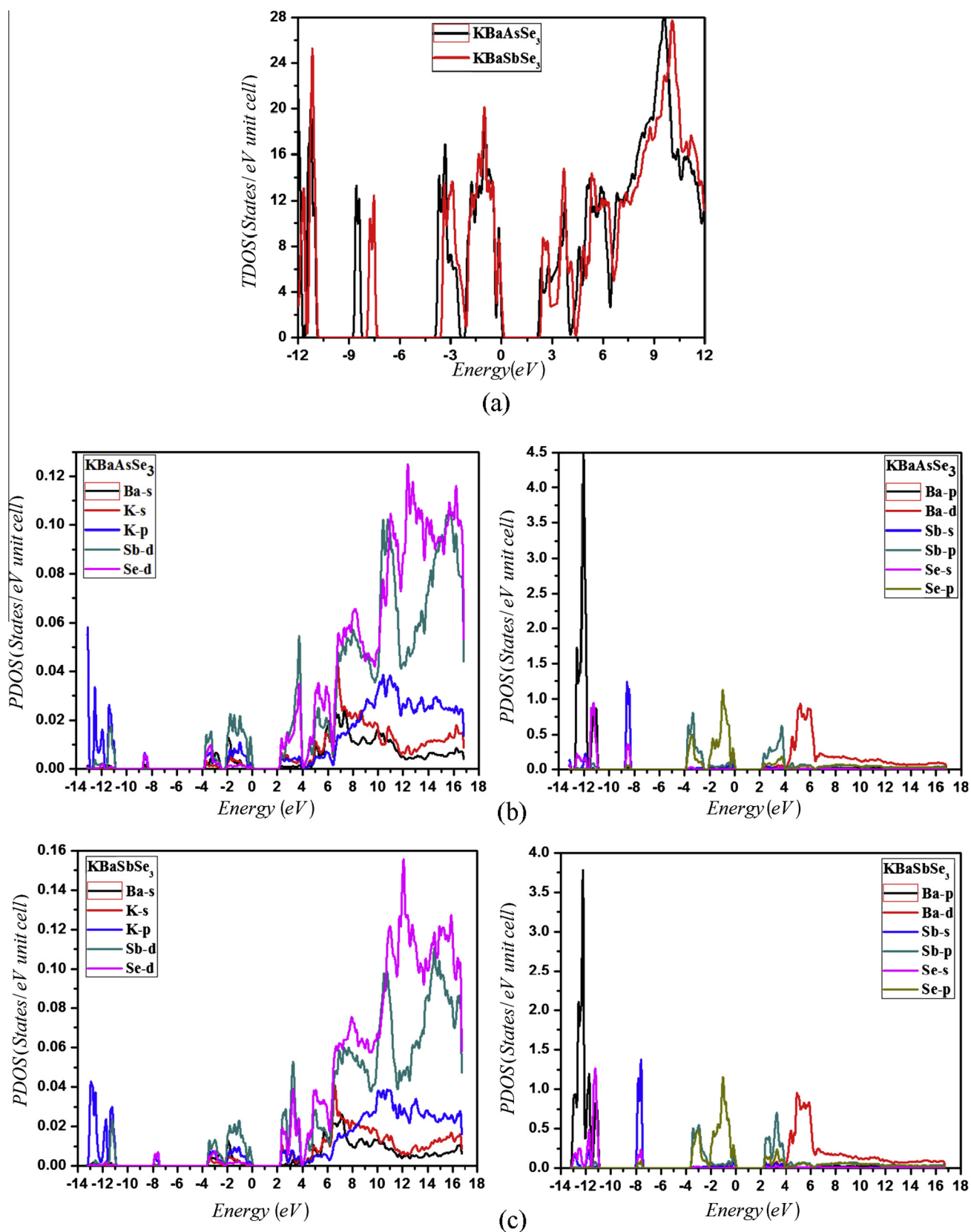


Fig. 3. (a) The calculated total density of states TDOS dispersions (States/eV) of KBaMSe_3 ($M = \text{As, Sb}$) compounds using mBJ; (b, c) The calculated partial density of states PDOS (States/eV) of KBaMSe_3 ($M = \text{As, Sb}$) compounds using mBJ.

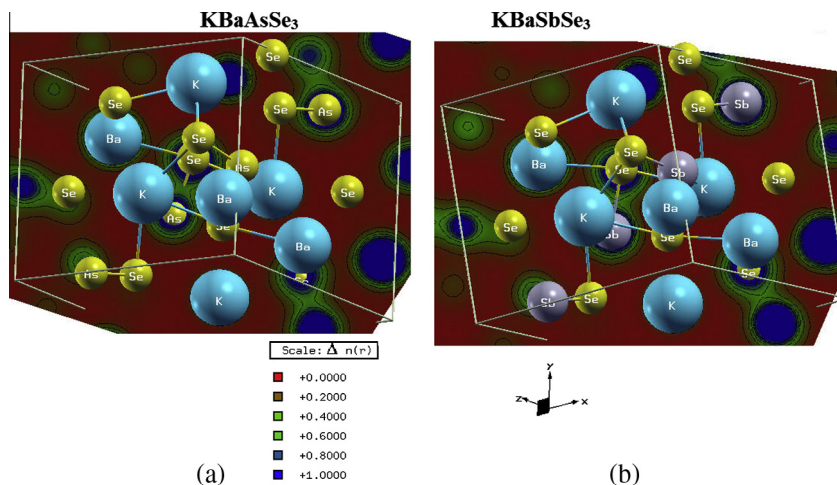


Fig. 4. The electronic charge density contour with mBJ in the (101) plane for KBaMSe_3 ($M = \text{As, Sb}$) compounds using mBJ.

2. Computational methodology

The crystallographic data of KBaAsSe_3 and KBaSbSe_3 obtained from Yin et al. [3] have been used in this study. Basically, the $\text{KBaAsSe}_3/\text{KBaSbSe}_3$ compound crystallizes in monoclinic structure comprising the space group $P21/c$ (# 14), with lattice parameters, $a = 9.369(2)$ Å, $b = 9.049(2)$ Å, $c = 9.247(2)$ Å, $\alpha = 90.00$, $\beta = 108.23(3)$, and $\gamma = 90.00$ ($a = 9.386(2)$ Å, $b = 9.199(2)$ Å, $c = 9.369(2)$ Å, $\alpha = 90.00$, $\beta = 108.25(3)$, and $\gamma = 90.00$). The unit cell crystal structures of both compounds are shown in Fig. 1. To study the electronic properties, we have used the all-electron-full-potential linear augmented plane wave (FP-LAPW) method based on first-principles density functional calculations as implemented in the WIEN2k [5,6]. It is well-known that the calculated band gap within DFT using local density approximations (LDA) [7], generalized gradient approximations (GGA) [8] is underestimated by around 30–40% compared to the experimental one. In order to overcome this drawback, Engle–Vosko GGA (EVBGA) [9] approximation and the modified Beck–Johnson potential (mBJ) [10] are adopted. The EVBGA was found to be quite successful in reproducing better band splitting, and hence better band gap value compared to LDA and GGA is observed. The plane-wave expansion $R_{\text{MT}} \times K_{\text{Max}}$ (R_{MT} represent minimum radius of the muffin-tin sphere and K_{Max} is the magnitude of the largest k vector in the plane wave expansion) was taken equal to 8. k sampling with 2000 k -points in the irreducible Brillouin zone (BZ) has been used, where this parameter controlled the size of the basis. The atomic sphere radii of atoms were considered as large as possible so that they would not overlap each other. Full-lattice optimization was used to perform the calculations. Self-consistent calculations are considered to be converged when the total energy of the system is stable within 0.1 mRy and the difference in the total electronic charge does not exceed 0.001e, as calculated in the consecutive steps. Within the muffin-tin (MT) spheres, the potential and charge density distributions are extended in spherical harmonics with orbital number $l_{\text{max}} = 10$. The chosen MT sphere radii of KBaAsSe_3 (KBaSbSe_3) are 2.5 a.u. for Ba/K atoms and 2.26 a.u. for As/Se atoms (2.5 a.u. for Ba/K atoms, 2.48 a.u. for Sb atom and 2.36 a.u. for Se atom).

3. Result and discussions

3.1. Band structure and density of states

The band structures and densities of states were predicted using the LDA, GGA, EVGGA and mBJ functionals. The calculated band structure profiles using the LDA, GGA, EV-GGA and mBJ for the herein studied compounds were similar except for the value of their band gaps which were higher within mBJ. Fig. 2 depicts the calculated band structures along the high symmetry directions points of the Brillouin zone (BZ) for the monoclinic KBaAsSe_3 and KBaSbSe_3 compounds within mBJ only. Following Fig. 2, it is illustrated that the conduction band minimum (CBM) is located at the Γ point of BZ for both compounds, while the valence band maximum (VBM) is located at the Y symmetry points for KBaAsSe_3 and at the middle of M point for KBaSbSe_3 , resulting in an indirect band gap semiconductors for KBaAsSe_3 and KBaSbSe_3 . The computed band gap of KBaAsSe_3 , are 1.43, 1.544 and 1.69, 2.08 eV for

LDA, GGA, EVGGA and mBJ, and for KBaSbSe_3 , are 1.59, 1.70, 2.153 and 2.10 eV for LDA, GGA, EVGGA and mBJ approximations, which are in good agreement with the experimental values (2.26 eV and 2.04 eV) and demonstrates an improved band gap values compared to those obtained by Yin et al. (1.52 eV and 1.67 eV) [3] using CASTEP code. The calculated density (i.e., total and partial) of states (TDOS and PDOS) for KBaAsSe_3 and KBaSbSe_3 compounds are shown in Fig. 3. It is clearly seen that there is an abrupt increase in DOS at the valence band (VB), which is apparent from the low dispersion in the band structure (Fig. 2).

To explicate the character of the electronic band structures, we were intended to the calculations of total and partial densities of states (TDOS and PDOS) of KBaAsSe_3 and KBaSbSe_3 compounds (see Fig. 3). The lowest bands (valence band) around -14.0 to -11.0 eV consist of Ba-p and Se-s states with small contribution of As/Sb-s/p/d states. The As/Sb-s and Se-s states along with small contribution of Ba-s and K-p states are located between -9.5 and -8.0 eV. The highest occupied valence band from -4.0 and 0.0 eV are derived from the As/Sb-p, Ba-s and Se-p states with a small contribution of K-s/p and As/Sb-d states that define the top of the valence band. The conduction band consists of Ba-s/d states with small contributions of As/Sb-p/d and K-s/p states. Analyzing the density of states (partial density of states), a strong hybridization exists between Ba-p and Se-s orbitals at around -14.0 to -12.0 eV. The hybridization is also seen between As/Sb-s and Se-s states at the energy range from -9.5 to -8.0 eV, and also at -4.0 to Fermi level, where a strong hybridization exist between Se-p and Ba-d orbital. The difference between the density of state structure of the two compound is that when the As atoms is replaced by Sb atoms, the whole structure moves towards lower energies, and the height of the peaks decrease as well.

3.2. Electronic charge density

The calculated total electronic charge density (ECD) in (101) planes for KBaAsSe_3 and KBaSbSe_3 compounds have been displayed in Fig. 4. In this paper we presented the charge density difference distributions to examine the bonding in both compounds. The bonding (ionic and covalent bonding) definition is based on density difference distributions. The ECD spectra for the KBaAsSe_3 and KBaSbSe_3 compounds, show tendency of covalent character for As/Sb-Se bonds which depends on Pauling electro-negativity difference of the atoms, K (0.820), As (2.050), Sb (2.020) and Se (2.550). It is evident that Se atom has higher electro negativity than the other atoms, so it is noticed that the maximum charges accumulated

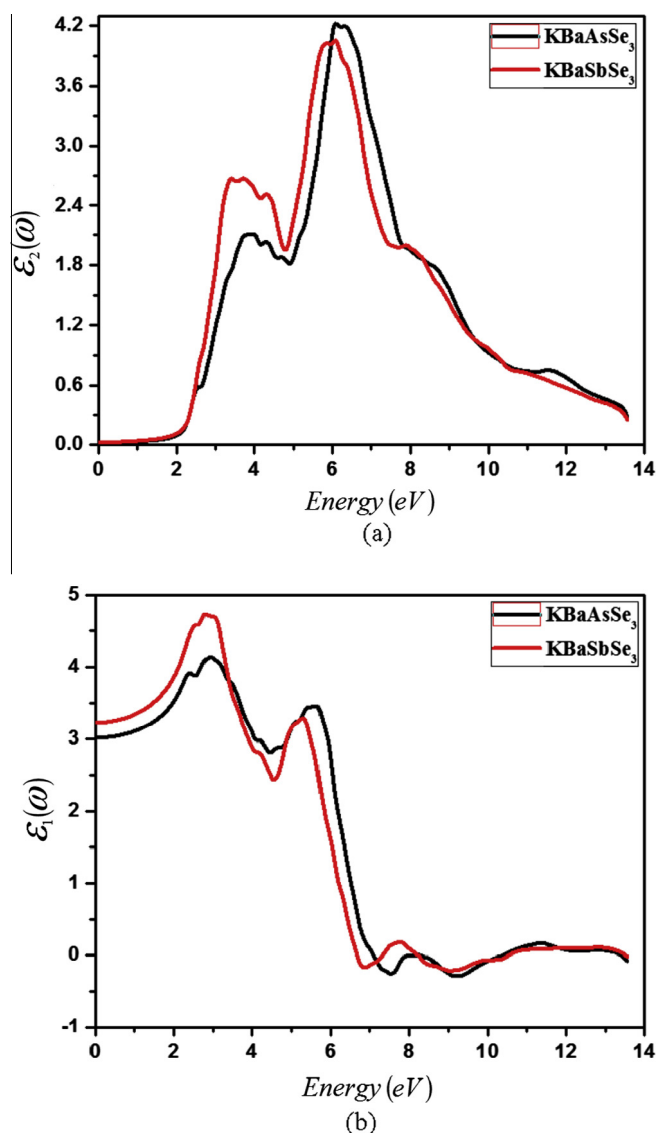


Fig. 5. Calculated imaginary part ($\epsilon_2^{average}(\omega)$) of KBAAsSe₃ compound (dark solid curve-black color online) and KBASbSe₃ compound (dark curve-red color online) spectra (a); and real part ($\epsilon_1^{average}(\omega)$) of KBAAsSe₃ compound (dark solid curve-black color online) and KBASbSe₃ compound (dark curve-red color online) spectra (b). (For interpretation of the references to colour in this figure legend, the reader is referred to the web version of this article.)

around Se-atom. If a glance taken inside the ECD contour, humps appears round the Se atom, which is due to the attraction between the next neighbors As atoms. If we look to the ECD of KBAAsSe₃ compound the humps appear around the Ba and Se atoms, a weak covalent bond between these two atoms can be observed. But when As is replaced by Sb atom, the bond distance between Ba and Se atoms increases though the humps appear between these, but there is no covalent bond exist between these atoms.

3.3. Linear optical properties

In this section, the complex dielectric function ($\epsilon(\omega) = \epsilon_1(\omega) + i\epsilon_2(\omega)$) of KBAAsSe₃ and KBASbSe₃ compounds is discussed. Basically, the imaginary part of the dielectric function, $\epsilon_2(\omega)$ depends on the momentum matrix elements and the joint density of states. The spectra for both (imaginary and real) parts are shown in Fig. 5, for an energy range 0–14 eV. The spectra of both compounds

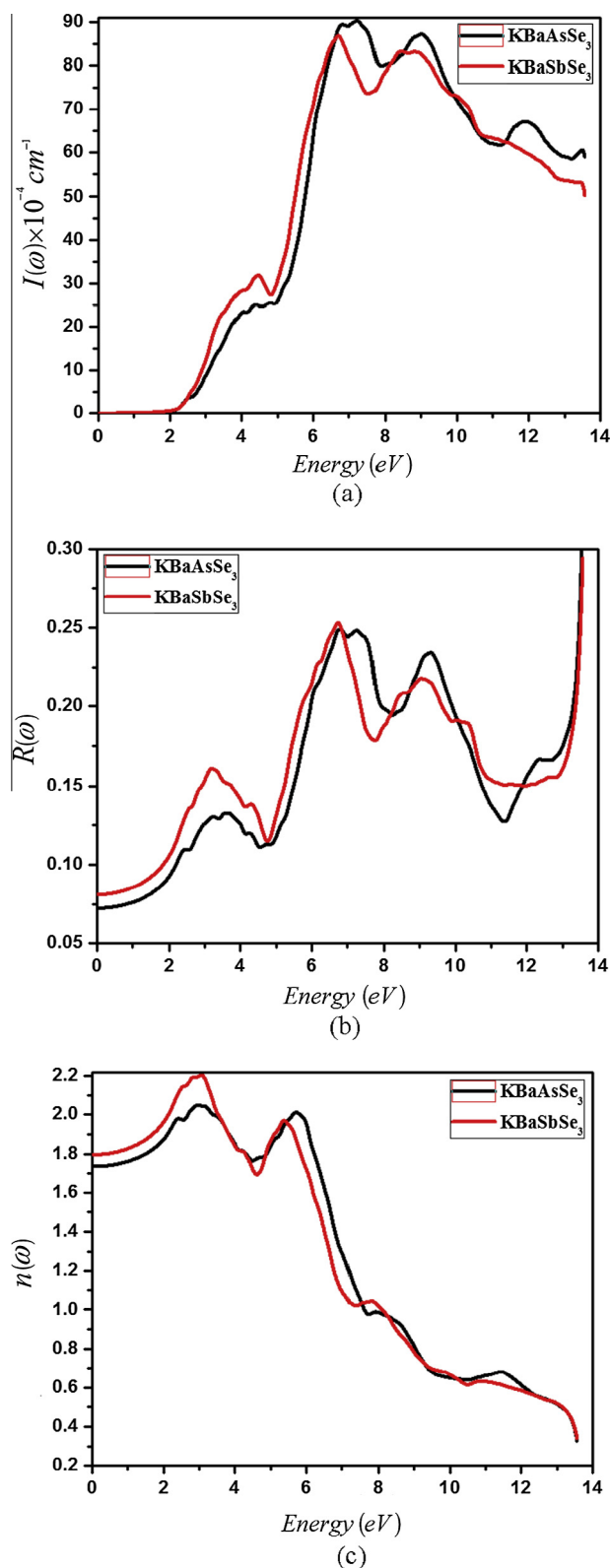


Fig. 6. Calculated energy loss spectrum ($I^{average}(\omega)$) of KBAAsSe₃ compound (dark solid curve-black color online) and KBASbSe₃ compound (dark curve-red color online) spectra (a); Calculated reflectivity ($R^{average}(\omega)$) of KBAAsSe₃ compound (dark solid curve-black color online) and KBASbSe₃ compound (dark curve-red color online) spectra (b); and Calculated refractive index ($n^{average}(\omega)$) of KBAAsSe₃ compound (dark solid curve-black color online) and KBASbSe₃ compound (dark curve-red color online) spectra (c). (For interpretation of the references to colour in this figure legend, the reader is referred to the web version of this article.)

illustrate some numerous peaks which communicate to electronic transitions from the occupied band to the unoccupied band. As our investigated compounds has the monoclinic symmetry, hence the dielectric functions are resolved into three components $\varepsilon^{xx}(\omega)$, $\varepsilon^{yy}(\omega)$ and $\varepsilon^{zz}(\omega)$. The investigated spectra of the imaginary parts $\varepsilon_2^{xx}(\omega)$, $\varepsilon_2^{yy}(\omega)$ and $\varepsilon_2^{zz}(\omega)$ of the frequency dependent dielectric function, but it will be shown only the calculated average dielectric function of both compounds as elucidated in Fig. 5. As it is clear from the spectra of both compounds that, as we move from KBaAsSe₃ compound to KBaSbSe₃ compound, though there is a shift in the structure towards the higher energy and the value of the peaks decreases.

To explain the calculated spectra of the imaginary part of the investigated compounds, the spectra are divided in two parts. The range of the first part is from 2.5 to 5.0 eV, whereas for the second one is above 6.0 eV. Mainly, the first part is dominated by Se-p, Sb-p and K-p transitions, where the interband transition (peak) arises between the valence band maximum (VBM) and conduction band minimum (CBM). These peaks arise for both compounds at 2.0 eV. The next group of the peaks is construed from the transitions from either Se-p or As-p states for both compounds. The main peak for both compounds appears at 7.0 eV.

The average real part of the dielectric function $\varepsilon_1(\omega)$, have been investigated by using the Kramers–Kronig relations [11]. The investigated spectra of $\varepsilon_1(\omega)$ for both compounds are plotted in Fig. 5(b). The zero frequency limits $\varepsilon_1(0)$ is mainly the imperative quantity, known as the electronic part of the static dielectric constant which is greatly influenced by the band gap. The calculated static values are 3.04 for KBaAsSe₃ and 3.57 for KBaSbSe₃. It has been interpreted that the smaller energy gap (E_g) assents a larger $\varepsilon_1(0)$ value [12], which is explained from the Penn model [13]. This (Penn) model is based on this formula $\varepsilon(0) = 1 + (\hbar\omega_p/E_g)^2$. From this expression it is apparent that $\varepsilon(0)$ is inversely proportional to E_g .

Mainly, the absorption coefficients from the $\varepsilon_1(\omega)$ and $\varepsilon_2(\omega)$ were evaluated. The average absorption spectra are shown in Fig. 6(a). About 2.0 eV the first absorption peak is originated for the KBaAsSe₃ and KBaSbSe₃ compounds. The absorption edge begins approximately at 2.1 eV for KBaAsSe₃ and KBaSbSe₃, which indicates close agreement to the experimental values (2.26 and 2.04) [3]. The absorption coefficient in the fundamental region is exalted almost $90 \times 10^4 \text{ cm}^{-1}$ for KBaAsSe₃ and KBaSbSe₃ compounds at ultraviolet region.

The average reflectivity spectra for the investigated compounds are illustrated in Fig. 6(b). In general, both investigated compounds show same behavior but KBaAsSe₃ compound shows greater reflectivity than the KBaSbSe₃. From the reflectivity spectrum, it can be inferred that these compounds display small reflectivity at low energies, then a rapid increase in the reflectivity occurs at the intermediate and the high energies. Basically, the reflectivity maxima take place from inter-band transitions, while they occurred between the energy ranges 6.0–10.0 eV and then above at 13.4 eV for both compounds, which is in the ultraviolet (i.e., both compounds can be therefore served as a possible shield for ultraviolet radiation).

The calculated average refractive indices for the investigated compounds are displayed in Fig. 6(c). In the refractive index, the peaks that appear are related to the peaks emerged in the imaginary part of the dielectric function. The refractive index spectra show greater peaks between 2.0 and 6.0, but a rapid decrease occurs at high energies in the refractive indices of both compounds.

This phenomenon is a significant physical parameter linked to the microscopic atomic interactions. On the theoretical standpoint, there are two approaches in screening this subject: the refractive index that is linked with the density, and the local polarizability of these individuals which are related to the energy gap E_g of the

material [14,15]. Hervé and Vandamme proposed an empirical formula in order to be motivated by simple physics of light refraction and dispersion, as follows [15]:

$$n = \sqrt{1 + \left(\frac{A}{E_g} + B\right)}$$

where $A = 13.6 \text{ eV}$, $B = 3.4 \text{ eV}$ and E_g is the band gap. The computed refractive indices of KBaAsSe₃ and KBaSbSe₃ compounds are 1.8695 and 1.8504, respectively. This is confirmed by the computation of the optical dielectric constant ε_∞ , which depends on the parameter n . From the average refractive index spectra, it can be concluded that the static value of $n(0)$ decreases as the band gap increases. The static values for KBaAsSe₃ and KBaSbSe₃ compounds are 1.72 and 1.8, respectively.

4. Conclusions

As a summary, we've studied the electronic structure and optical properties of the KBaMSe₃ ($M = \text{As, Sb}$) by using the FPLAPW through the density functional theory. It has been found that the calculated band gaps are in good agreement with the available experimental data. To obtain the comparable energy gap, we also used EVGGA which shows better band gap than the LDA and GGA. The calculated band structures reveal that both compounds are indirect band gap semiconductors.

Through analyzing the density of states (partial density of states), a strong hybridization between Ba-p and Se-s, As/Sb-s and Se-s and also between Se-p and Ba-d orbital is observed. As we replace As by Sb atom, the density of structure moves toward lower energies. The dielectric function, refractive index, energy loss function, absorption coefficient and reflectivity of the compounds were also investigated. The absorption edge begins approximately at 2.08 and 2.1 eV for KBaAsSe₃ and KBaSbSe₃, which indicates a close agreement with the experimental values (2.04 and 2.26).

Acknowledgement

The result was developed within the CENTEM project, reg. no. CZ.1.05/2.1.00/03.0088, co-funded by the ERDF as part of the Ministry of Education, Youth and Sports OP RDI programmed. Computational resources were provided by MetaCentrum (LM2010005) and CERIT-SC (CZ.1.05/3.2.00/ 08.0144) infrastructures.

References

- [1] D. Mei, Z. Lin, L. Bai, J. Yao, P. Fu, Y. Wu, J. Solid. Stat. Chem 183 (2010) 1640–1644.
- [2] G. Zhang, B. Zhang, H. Chen, X. Zhang, C. Zheng, J. Lin, F. Huang, J. Alloys Comp. 591 (2014) 6–10.
- [3] W. Yin, K. Feng, L. Kang, B. Kang, J. Deng, Z. Lin, J. Yao, Y. Wu, J. Alloys Comp. 617 (2014) 287–291.
- [4] D. Mei, Z. Lin, L. Bai, J. Yao, P. Fu, Y. Wu, J. Solid. Stat. Chem. 183 (2010) 1640–1644.
- [5] K.M. Wong, S.M. Alay-e-Abbas, A. Shaikat, Y. Fang, Y. Lei, J. Appl. Phys. 113 (2013) 014304.
- [6] K.M. Wong, S.M. Alay-e-Abbas, Y. Fang, A. Shaikat, Y. Lei, J. Appl. Phys. 114 (2013) 034901.
- [7] J.P. Perdew, K. Burke, M. Ernzerhof, Phys. Rev. Lett. 77 (1996) 3865.
- [8] V. Panchal, D. Errandonea, A. Segura, P. Rodriguez-Hernandez, A. Munoz, J. Appl. Phys. 110 (2011) 043723.
- [9] E. Engel, S.H. Vosko, Phys. Rev. B 50 (1994) 10498.
- [10] F. Tran, P. Blaha, Phys. Rev. Lett. 102 (2009) 226401.
- [11] W.T. Ching, P. Rulis, Phys. Rev. B 73 (2006) 045202.
- [12] A. Chahed, O. Benhelal, S. Laksari, B. Abbar, B. Bouhafs, N. Amrane, Phys. B 367 (2005) 142.
- [13] D.R. Penn, Phys. Rev. 128 (1962) 2093.
- [14] N.M. Balzaretti, J.A.H. dajornada, Solid State Commun. 99 (1996) 943.
- [15] P.J.L. Hervé, L.K.J. Vandamme, J. Appl. Phys. 77 (1995) 77.

Chapter 7

Curriculum vitae

Curriculum vitae

SIKANDER AZAM S/O Mr. FAZLI RABBI

Date Of Birth: Jan 30th 1982

Email: sikander.physicst@gmail.com



PRESENT ADDRESS

New Technologies - Research Center,
University of West Bohemia,
Univerzitni 8, 306 14 Pilsen,
Czech Republic
(+420) 775928620

PERMANENT ADDRESS

Vill and P/O Dagai,
Mohallah Hamzakheil,
District Swabi, Tehsil Razar,
KPK, Pakistan,
(+92) 3339459711.

Research area

Condensed Matter Physics (Electronic Structure Calculation): In condensed matter physics, I do study on Electronic Structure, Elastic properties, optical and thermoelectric properties of the solid materials in the light of Density Functional Theory (DFT). It may be mentioned that with the knowledge of band structure of a material, the understanding of various properties of materials has been increased in the past few decades. Starting with atomic number only, the electronic structure calculation can be done and based on the information one can engineer to modify the crystal structure and further can determine the total energies of all the possible crystal structures. Thus the most stable structure can be determined. In the second part, I study on the elastic properties of the materials. It is of particular interest as they determine the mechanical stability of the materials. Elastic properties of a solid are important because of they relate to various fundamental solid state properties. Therefore, it will be desirable if before carrying out expensive and tedious time consuming process of experiments to determine electronic band structure, density of states and elastic properties, one can use computational tools for theoretical calculation to understand these parameters and hence save both the time and resources for technology development with better-designed experiments. DFT is commonly used to calculate the electronic structure of simple and complex systems containing many atoms such as large molecules or solids. It is based on electron density rather than on the wave function and treated both exchange and correlation but approximately. In this method, many body problems of interacting electrons and nuclei are mapped to a series of one-electron equations which is called Kohn-Sham (KS) equations. For the solution of the KS equations, several methods have been developed with the Linearized Augmented Plane Wave (LAPW). Based on this, a computer code WIEN2K is used to solve the KS equations and thus obtain the crystal properties on atomic scale.

EDUCATION

2011	M.Phill.	Hazara University
2008	M.Sc.	University of Malakand
2002	B.Sc.	University of Peshawar
2000	F.Sc.	BISE Peshawar
1998	SSc.	BISE Peshawar

At present: PhD student, working under the supervision of Prof. Dr. Jan Minar from 1st January 2012 till now. New Technologies - Research Center, University of West Bohemia, Univerzitni 8, 306 14 Pilsen, Czech Republic

Master in Philosophy thesis title (M. Phil):

Study of medicinal plants by using PIXE techniques.

My PhD thesis dissertation:

First principle studies of optical, thermoelectric and electronic characteristics of complex materials.

EXPERIENCE

Teaching; Teaching experience in different graduate and undergraduate institutes during 2006-2009.

Proficiencies:

- Wien2k code.
- Elastic Code
- Gibbs Code
- SPRKKR Code
- BoltzTraP Code
- RSPt Code

- Success as a laboratory and tutorial instructor in general Physics, Experienced working in a multidisciplinary team. Appropriate organization, record keeping, verbal and written communication skills.
- Have enough experience of working in different computer programs including MS-word, MS-excel MS-Power Point, and Web Browsing etc.

Courses studied in PhD:

1. Physical Chemistry for Metallurgists (Prof.RNDR. Jaroslav Fiala, CSc.F Eng)
2. Experimental methods of material properties study (RNDR. Dagmar Jandov, Ph.D.; RNDR. Josef Kasl, CSc.)
3. Theory of plasma-based technologies (RNDR. Josef Kasl, CSc.)
4. Physical Biology (Prof.Dr Petr Chvosta+ Daliber Stys)
5. Density functional theory (Prof.Dr Ali.H.Reshak)
6. Application of Laser in Bio Physics (Prof.Dr Ali.H.Reshak).
7. Full Potential Linear Augmented Plane Wave Method 1 (Prof.Dr Ali.H.Reshak).
8. Full Potential Linear Augmented Plane Wave Method 2 (Prof.Dr Ali.H.Reshak).
9. Light Interaction with the Matter - Linear Phenomenon 1 (Prof.Dr Ali.H.Reshak).

Other subjects studied (in M.phil and Master):

Quantum mechanics, mathematical method of physics, Classical mechanics,	statistical mechanics, Plasma physics, Optical properties, Solid state	Quantum optics Modern physics University of Malakand Electro dynamics,	Magnetism, Electronics Nuclear physics Electro magnetic theory
--	---	---	--

Conferences/Workshops Attended:

- "5Mv tandem Accelerator And Its Applications by Dr. Aqeel Ahsan Khurram on 8th October 2009
- Participated in a seminar delivered by Dr. Gul Rasool (research Officer South-Korea) on computational physics, 9th March 2010, at university of Hazara.
- Workshop arranged on Astronomy Physics by Physics Department university of Hazara.
- School on LHC At NCP, Islamabad from 24 April to 04 may 2011
- International conference on Condensed Matter Physics and Engineering Bahauddin Zakariya University, Multan, Pakistan 2012.
- International workshop on Materials Modeling and simulation University of Malakand Pakistan 2013.
- DPG-Frhjahrstagung (DPG Spring Meeting) Dresden
- Autum School on correlated Electrons (FZ, Jlich) (poster presentation)
- Hands-on course Introduction to the application of ab-initio methods in spectroscopy, New Technologies Research Centre, University of West Bohemia address: Univerzitni 8, 30614 Plzen, CZ (poster presentation)
- DPG conference in Berlin, March 15th to 20th 2015 (Oral talk)

Language Skills:

Proficient to speak, read and write	English (international),
Proficient to speak, read and write	Urdu (national),
Proficient to speak, read and write,	Pashto (local)

Academic References:

- **Prof. Dr. Jan Minar**

Department Chemie und Biochemie Ludwig-Maximilians-Universitt Mnchen,
Butenandtstr. 11, Haus E 81377 Mnchen, Germany
Email: Jan.Minar@cup.uni-muenchen.de

- **Prof. Dr. Ondrej Sivr**

Institute of Physics Academy of Sciences of the
Czech Republik Cukrovarnicka 10162 53 Praha 6 Czech Republic
Email: sivr@fzu.cz

Chapter 8

List of publications

Sikander Azam, PhD student
Publications 48
Total Impact Points 92.92
Citations 104

Journal Publications

1. Saleem Ayaz Khan, Sikander Azam, Ondrej Sipr, *Materials Science in Semiconductor Processing*, 41 (2016) 45-53.
2. Sikander Azam, Saleem Ayaz Khan, Souraya Goumri-Said, *Journal of Electronic Materials*, 45 (2015) 1-9.
3. Sikander Azam, Saleem Ayaz Khan, Souraya Goumri-Said, *Materials Science in Semiconductor Processing*, 39 (2015) 606–613
4. Sikander Azam, Saleem Ayaz Khan, Souraya Goumri-Said, *Journal of Solid State Chemistry*, 229 (2015) 260–265
5. Sikander Azam, Saleem Ayaz Khan, Wilayat Khan, Saleh Muhammad, Haleem Udin, G. Murtaza, R. Khenata, Fahad Ali Shah, Jan Minar, W.K. Ahmed, *Journal of Alloys and Compounds*, 644 (2015) 91–96
6. Wilayat Khan, Sikander Azam, Ali Fahad, Shah, Souraya Goumri-Said, *Solid State Sciences* 48 (2015) 244-250
7. Bendjedid, T. Seddik, R. Khenata, H. Baltache, G. Murtaza, A. Bouhemadou, S. Bin Omran, Sikander Azam, Saleem Ayaz Khan, *Journal of Magnetism and Magnetic Materials*, 396 (2015) 190–197
8. Sikander Azam, Saleem Ayaz Khan, Jan Minar, Souraya Goumri-Said, *Current Applied Physics*, 15 (2015) 1160-1167
9. Saleem Ayaz Khan, Sikander Azam, Fahad Ali Shah, Bin Amin, *Optical Materials* 47 (2015) 372–378
10. Sikander Azam, Saleem Ayaz Khan, Souraya Goumri-Said, *Materials Research Bulletin*, 70 (2015) 847–855
11. Sikander Azam, Saleem Ayaz Khan, *Materials Science in Semiconductor Processing*, 34 (2015) 250–259
12. Fahad Ali Shah, Saleem Ayaz Khan, Suneela Arif, Sikander Azam, R. Khenata, S. Bin Omran, *Current Applied Physics* 15 (2015) 608-616

13. M. El Amine Monir, R. Khenata, G. Murtaza, H. Baltache, A. Bouhemadou, Y. Al-Douri, S. Azam, S. Bin Omran, H. Ud Din, *Indian J Phys*, 89 (2015) 1251–1263
14. Sikander Azam, Saleem Ayaz Khan, Jan Minar, Wilayat Khan, Haleem Ud Din, R Khenata, G Murtaza, S Bin-Omran, Souraya Goumri-Said, *Semicond. Sci. Technol.*, 30 (2015) 105018 (9pp)
15. Saleem Ayaz Khan, Sikander Azam, *Materials Research Bulletin* 70 (2015) 436–441
16. Sikander Azam, A.H. Reshak, *Materials Science in Semiconductor Processing*, 31(2015) 372–379
17. Sikander Azam, Saleem Ayaz Khan, R. Khenata, G. Murtaza, S. Bin Omran, Saleh Muhammad, *Zeitschrift für Naturforschung A*, 70 (2015) 187 (8pp).
18. M. El Amine Monir, H. Baltache, R. Khenata, G. Murtaza, Sikander Azam, A. Bouhemadou, Y.Al-Douri, S. Bin Omran, Roshan Ali, *Journal of Magnetism and Magnetic Materials*, 378 (2015) 41–49
19. Sikander Azam, A. H. Reshak, *Journal of Physica B* 464 (2015) 9–16
20. H. Reshak, Sikander Azam, *Materials Science in Semiconductor Processing*, 30 (2015) 197–207
21. Sikander Azam, Saleem Ayaz Khan, Fahad Ali Shah, Saleh Muhammad Haleem Ud Din, R. Khenata, *Intermetallics*, 55 (2014) 184-194
22. H. Reshak, Y.Al-Douri, R. Khenata, Wilayat Khan, Saleem Ayaz Khan, Sikander Azam, *Journal of Magnetism and Magnetic Materials*, 363 (2014)133–139
23. H. Reshak, Sikander Azam, *Journal of Magnetism and Magnetic Materials*, 362 (2014) 204–215
24. O. Miloud Abid, A. Yakoubi, A. Tadjer, R. Khenata, R. Ahmed, G. Murtaza, S. Bin Omran, Sikander Azam, *Journal of Alloys and Compounds* 616 (2014) 475–482
25. Haleem Ud Din, Sikander Azam, Saleem Ayaz Khan, R. Khenata, *Journal of Alloys and Compounds* 615 (2014) 507–513
26. Sikander Azam, A. H. Reshak, *Materials Science in Semiconductor Processing*, 26 (2014) 649–656
27. Sikander Azam, A. H. Reshak, *Solid State Sciences*, 32 (2014) 26-34
28. Sikander Azam, A. H. Reshak, *Journal of Organometallic Chemistry*, 766 (2014) 22-33
29. Sikander Azam, A. H. Reshak, *RSC Adv.*, 4 (2014) 20102

30. H. Reshak, Sikander Azam, *Optical Materials*, 37 (2014) 97–103
31. Fahad Ali Shah, Sikander Azam, *Solid State Sciences* 34 (2014) 56-62
32. A. H. Reshak, Sikander Azam, Z. A. Alahmed, *Int. J. Electrochem. Sci.*, 9 (2014) 975 – 989
33. Sikander Azam, Wilayat khan, Saleem Ayaz Khan, A. H. Reshak, *International Journal of Engineering Research & Technology*, 3 (2014) 564-570
34. A. H. Reshak, Sikander Azam, *Appl. Phys. A* 116 (2014) 333–340
35. Sikander Azam, Jiri Bila, H. Kamarudin, A. H. Reshak, *Int. J. Electrochem. Sci.*, 9 (2014) 445 – 459
36. A. H. Reshak, Sikander Azam, *Journal of Magnetism and Magnetic Materials*, 342 (2013) 80–86
37. Sikander Azam, Wilayat khan, Saleem Ayaz Khan, A. H. Reshak, *International Journal of Innovative Research in Science, Engineering and Technology*, 3 (2014) 9571-9578
38. A. H. Reshak, Sikander Azam, Jan Chyský, *Int. J. Electrochem. Sci.*, 9 (2014) 460 - 477
39. H. Reshak, Sikander Azam, *Journal of Magnetism and Magnetic Materials*, 352 (2014) 72–80
40. Sikander Azam: *Journal of Magnetism and Magnetic Materials* 351 (2014) 98–103
41. Sikander Azam, A. H. Reshak, *Physica B*, 431 (2013) 102–108
42. Sikander Azam, A. H. Reshak, *Int. J. Electrochem. Sci.*, 8 (2013) 10359 – 10375
43. A. H. Reshak, Sikander Azam, *Journal of Magnetism and Magnetic Materials*, 345 (2013) 294–303
44. A. H. Reshak, Sikander Azam, *Int. J. Electrochem. Sci.*, 8 (2013) 10396 – 10423
45. Wilayat khan, Sikander Azam, Saleem Ayaz Khan, A. H. Reshak, *International Journal of Innovative Research in Science, Engineering and Technology*, 3 (2014) 9579-9588
46. A. H. Reshak, Sikander Azam, *J. Material Sci. Eng.*, 3 (2014) 1-5
47. Saleem Ayaz Khan, Wilayat khan, Sikander Azam, A. H. Reshak, *International Journal of Innovative Research in Science, Engineering and Technology*, 3 (2014) 9626-9634
48. A. H. Reshak, Sikander Azam, *Journal of Magnetism and Magnetic Materials*, 358-359 (2014)16–22